UNIVERSIDAD COMPLUTENSE DE MADRID
FACULTAD DE CIENCIAS FÍSICAS

TESIS DOCTORAL

Measuring entanglement and topology in optical lattices:
local answers to non-local questions

MEMORIA PARA OPTAR AL GRADO DE DOCTOR

PRESENTADA POR

Emilio Alba Linero

Director

Juan José García Ripoll

Madrid, 2014

UNIVERSIDAD COMPLUTENSE DE MADRID
FACULTAD DE CIENCIAS FÍSICAS

Measuring entanglement and topology in optical lattices

Local answers to non-local questions

Emilio Alba Linero

Memoria presentada para optar
al título de Doctor en Ciencias Físicas

Dirigida por
Dr. Juan José García Ripoll

CONTENTS

Part I

INTRODUCTION

1. RESUMEN EN CASTELLANO

1.1 Motivación

Los últimos años han sido testigo de avances espectuaculares en el control y manipulación de sistemas cuánticos. El Santo Grial de este esfuerzo es, desde hace algo más de dos décadas, el ordenador cuántico; un dispositivo que reduciría los ordenadores convencionales a abacos y que podría enfrentarse a clases de problemas que son intratables o inimaginables para la computación clásica. Con esa visión en el horizonte, lejana en la situación tecnológica actual, los experimentos se han centrado en la antecima de la simulación cuántica, que es ya una realidad palpable.[1]

La simulación cuántica consiste en recrear las características o dinámica de un sistema físico muy complejo a estudiar (típicamente, sistemas muy correlacionados intratables computacionalmente) en un sistema cuántico que ha sido diseñado a tal efecto. Las plataformas experimentales que se usan y proponen para estas simulaciones son muchas: iones atrapados, circuitos superconductores, cavidades,... a lo largo de esta tesis veremos muchos ejemplos en una sola plataforma: átomos ultrafríos en redes ópticas. Para conocer más sobre este sistema, referimos al capítulo 3 de esta tesis y las referencias allí incluidas.

Esta tesis se centra en un aspecto muy específico de las simulaciones, y que a nuestro juicio consiste en una de las cuestiones que más información ofrece sobre el sistema simulado: la medida de observables característicos. La motivación de esta tesis no consiste sólo en medir con la intención de atribuir valores a propiedades conocidas; sino que la misma *definición* de observables y medidas arroja una luz sobre el sistema que queremos estudiar y al que, en ocasiones, sólo nos podemos aproximar con modelos que preasumen la existencia de este tipo de clasificación por medidas. Por ilustrar esta idea de forma un poco más extrema, creemos que la aproximación al conocimiento de un sistema complejo se basa en dar respuesta a preguntas (los observables) que no caracterizan por completo el sistema, pero extraen lo que más nos interesa, dejando el resto inexplorado para futuras sorpresas (ejemplos sobre observables específicos que interesan en sí pueden ser el número de estados de borde en un aislante, la presencia de superconductividad o la degeneración de un estado fundamental).

El trabajo contenido en esta tesis se centra en la medida de dos propiedades no locales de un sistema: la topología y entrelazamiento. Aunque a lo largo de la tesis aparecen conectadas y relacionadas en más de una ocasión, el foco principal cae sobre la primera. Revisemos brevemente en qué consisten y cuáles son los motivos para creer que medir estas propiedades constituye un avance en el estado actual del conocimiento.

La topología, y especialmente la aplicación de este concepto en física de materia condensada, ha sido una de las principales vías de estudio en sistemas complejos en

---

[1] Existe un fuerte debate entre puristas sobre qué constituye verdadera simulación cuántica; o incluso si una verdadera simulación no sería al menos tan útil como un potencial ordenador cuántico. Esta tesis elude ese debate y se centra en los aspectos prácticos de las simulaciones experimentales.

los últimos años. Existen dos acepciones comúnmente utilizadas sobre que queremos decir con topología, y la relación entre ellas en difusa. La primera, de uso corriente en ciencia de estado sólido, se refiere a la distinción entre materiales que son aislantes (o superconductores) pero que presentan diferentes comportamiento en el borde (por ejemplo, conducción sin dispersión) dependiendo de propiedades que no son distinguibles con medidas locales. Ejemplos paradigmáticos son el efecto Hall cuántico anómalo, el efecto Hall cuántico de espín o la cadena fermiónica de Kitaev. La segunda acepción es más usada en el marco de la computación cuántica topológica, y típicamente trata con modelos cuyas propiedades (por ejemplo, la degeneración del estado fundamental o la estadística de las excitaciones de baja energía) dependen críticamente de la topología de la variedad en que se inscribe el model. Un ejemplo típico es el código tórico.

Aunque existe relación entre estas definiciones, y muchos trabajos utilizan versiones refinadas de éstas, podemos decir que esta tesis trabaja fundamentalmente en el marco de la primera acepción. En este sentido, definiremos una serie de invariantes, que toman valores enteros, cuya medida caracterizaría parcial o totalmente propiedades en los bordes del sistema. Una definición más precisa de qué entenderemos por topología (y, específicamente, por estado topológicamente no trivial) la presentamos en el capítulo 4 de esta tesis.

El entrelazamiento, por otra parte, constituye una de las características distintivas y más antiintutitivas de la mecánica cuántica. En sí, el entrelazamiento es una consecuencia natural que establece la existencia de correlaciones más fuertes que las clásicas entre partes de un sistema (por ejemplo, entre dos partículas). Sin embargo, y desde el asentamiento del formalismo cuántico como teoría para explicar el mundo microscópico, el entrelazamiento ha sido la base sobre la que atacar dicha teoría (como hicieron Einstein, Podolsy y Rosen en su célebre artículo de 1935 [28]) o la propiedad definitoria de las nuevas reglas de la física moderna, en palabras de Schrödinger [83].

En el campo de la computación cuántica el entrelazamiento es, ante todo, un recurso fundamental para implementar los algoritmos que la hacen tan especial. La mejor forma de resaltar su importancia es en el modelo de computación cuántica basa en medidas (MBQC) que, como indica su nombre, aspira a realizar un cálculo arbitrario únicamente a base de hacer medidas en partículas sueltas. Condición necesaria para poder aplicar estos protocolos es la existencia de un tipo de estado entrelazado, llamado estado grafo, que implica la existencia de entrelazamiento entre dos de sus partes cualesquiera. En este contexto, creemos que la medida de un estado grafo es un paso importante en el camino para la aplicación de estos protocolos.

Por último, y de forma más especulativa, existe un esfuerzo por comprender cuál, si la hay, es la relación entre estados topológicos y entrelazamiento; relación que es natural ya que los estados topológicos mantienen correlaciones especiales a largas distancias. Esto no es una prueba, y los esfuerzos por conectar estas áreas para caracterizar mejor los sistemas de muchas partículas son continuos y se han redoblado a partir del análisis de espectros de entrelazamiento [63]. En este apartado, también esta tesis prentende aportar medidas que clarifiquen qué podemos esperar al usar estas clasificaciones de entrelazamiento en problemas de materia condensada.

1.2 Resultados

Como hilo conductor, la tesis trata la posibilidad de caracterizar y detectar propiedades no locales de gases atómicos ultrafríos. Como hemos mencionado, las principal motivación para esta colección de propuestas surge del campo de la simulación cuántica y la información cuántica. A continuación vamos a listar los resultados principales de esta tesis, siguiendo aproximadamente el orden en que han sido estructurados los capítulos:

- **Un Hamiltoniano de Dirac completo y controlable puede ser implementado de forma realista en una red óptica bidimensional.**

  Hemos revisado la forma en la que un modelo de tipo enlace fuerte (o tight-binding, en inglés) con partículas masivas puede dar lugar a teorías de fermiones sin masa de Dirac en el límite de baja energía. En particular, se detalla la relación entre todos los posibles términos que pueden incluirse en el Hamiltoniano (sin interacción) y los parámetros microscópicos controlables. Las especificidades de la implementación son explicadas de forma cuantitativa, con el objetivo de realizar una propuesta experimental completa.Por último, se sugiere el empleo de varios protocolos de medida, según las características particulares del experimento que se quiera realizar, y que allanan el camino para la realización de simulaciones más complejas en experimentos similares. Este resultado es expuesto principalmente en el capítulo 6.

- **El orden topológico de un aislante de Chern puede ser medido mediante imágenes en tiempo de vuelo de átomos confinados en redes ópticas.**

  Hemos demostrado que un aislante de Chern puede ser implementado y caracterizado en un experimento de redes ópticas. Un índice (o winding number, en inglés) que toma valores en los enteros puede ser medido a partir de imágenes en tiempo de vuelo del gas atómico, lo que resulta equivalente a la medida de su número de Chern. Hemos comprobado numericámente que el protocolo de detección es robusto frente a las inhomogeneidades y temperaturas propias de estos experimentos con redes ópticas, como cabe esperar de un invariante topológico entero. Este resultado es expuesto principalmente en el capítulo 7.

- **El número de Chern de un sistema compuesto de dos pseudoespines puede ser medido de forma exacta a partir de índices parciales.**

Hemos demostrado que el número de Chern de un sistema 4x4 con invariancia traslacional puede ser descompuesto como la suma de las fases de berry -o índices- de dos particiones de tipo pseudoespín. La prueba requiere que dichas particiones no se encuentren maximamente entrelazadas en ningún punto en espacio de momentos -lo que supone una gran restricción a la hora de seleccionar las biparticiones. En general, esta restricción implica motivar la elección de particiones en base a alguna simetría del problema.

Además, y basándonos en este resultado y el expuesto en el punto anterior, podemos concluir que el número de Chern de un sistema compuesto también puede ser medido mediante imágenes en tiempo de vuelo; exponemos este resultado con un ejemplo paradigmático: una propuesta para medir modos de Majorana en un experimento con redes ópticas completamente detallado. Estos resultados están expuestos en los capítulos 5 y 8.

- **El índice topológico puede ser usado para detectar transiciones de fase en sistemas con grados de libertad adicionales.**

  Hemos construido un model de enlace fuerte que incluye el efecto de potenciales Abelianos y no Abelianos sobre fermiones masivos. Las medidas realizadas únicamente en el grado de libertad de espín son suficientes para construir un índice topológico que cambia de valor al cruzar una transición de fase provocada por el potencial no Abeliano, como se demuestra numéricamente. Reafirmando la intuición de la que nos dota el resultado expuesto en el punto anterior, la cantidad de información extraída a partir de estas medidas parciales depende críticamente de la ruptura de simetrías relevantes del problema. Este resultado está expuesto en el capítulo 9.

- **El entrelazamiento genuinamente multipartito puede ser medido localmente en estados grafo.**

  Hemos demostrado que la fidelidad local a un estado grafo puede ser medida en un modelo sencillo de qubits -o bits cuánticos- en una red atómica bipartita. Lo que es más importante, esta fidelidad contituye un testigo de entrelazamiento genuinamente multipartito que puede ser computado sobre regiones arbitrarias, haciendo uso únicamente de dos conjuntos de medidas simultáneas. Hemos incluido evidencia numérica de que este protocolo funciona aun en rpesencia de diferentes fuentes de ruido propias de experimentos con redes ópticas. Aunque las medidas son en sí destructivas, el método es útil tanto como forma de certificar entrelazamiento entre muchas partículas como para calibrar un experimento que tenga el propósito de construir estados grafo de gran tamaño. Este resultado está expuesto en el capítulo 10.

1.3 Líneas de ampliación

Esta sección hará un compendio de las posibles direcciones de investigación que abre el cuerpo de resultados de esta tesis, además de comentar brevemente algunas ideas más especulativas que pueden afianzarse como posibles campos de investigación o ser descartadas.

Una de las principales cuestiones que motiva esta tesis, y que forma parte del núcleo duro de la investigación en el campo de la simulación cuántica, es cómo computar y caracterizar con éxito el efecto de interacciones entre muchas partículas. En la mayoría de problemas, y específicamente en problemas de fermiones en redes de dos o más dimensiones, los métodos numvericos clásicos son muy costosos computacionalmente o directamente inútiles. Sin embargo, muchos de estos problemas son importantes: pueden dar origen a fases exóticas de la materia con excitaciones anyónicas, a modos de Majorana topológicamente protegidos e incluso a explicaciones sobre la superconductividad de alta temperatura crítica.

Esta tesis presenta una nueva herramienta para atacar esos problemas: un observable, el índice topológico, que puede ser medido en experimentos de redes ópticas con técnicas de imagen rutinarias. Este invariante no es sólo equivalente al número de Chern en su caso más sencillo, sino que los capítulos 5 y 8 demuestran que esa equivalencia puede mantenerse en casos más complejos, con la ventaja añadida de dar información sobre el contenido de entrelazamiento entre particiones. Si algún experimento es capaz de controlar la elección de biparticiones a voluntad, estas herramientas caracterizan directamente las propiedades de escala del espectro de entrelazamiento del sistema.

Aun más, el índice topológico puede ser usado como un invariante con sentido completo cuando no tenemos acceso al conjunto de grados de libertad del estado. Ésto ha quedado demostrado en el capítulo 9 para un caso sencillo, pero la potencia del método podría quedar mejor ilustrada aplicándolo a un sistema fuertemente correlacionado.

Otra pregunta que surge de forma natural es si existe algún conjunto de observables que capturen el número de Chern en sistemas mayores que los pseudoespines - una especie de índice topológico para dimensiones más altas. En cierto sentido, el problema de un espín es simple porque tres observables equivalen a una tomografía completa del estado, pero la experiencia con sistemas compuestos 4x4 da esperanzas de que los sistemas más complejos no necesiten un conjunto de observables equivalentes a la tomografía; esperamos que aparezcan nuevas (¡y muy interesantes!) restricciones sobre los estados a medir, como sugiere la importancia del entrelazamiento para sistemas compuestos de dos pseudoespines.

Por último, esta tesis apunta sobre algunas direcciones generales que puede ser interesante mencionar. Por ejemplo, ¿hay algún protocolo escalable para medir espectros de entrelazamiento? ¿Son los invariantes parciales relevantes a la hora de caracterizar un estado y, si es así, qué sentido tiene que toda la información topológica este restringida a unos grados de libertad específicos? Ya que es posible modelar aislantes y superconductores topológicos como sistemas bidimensionales de espín, ¿cuál podría ser el sentido de hacer que esta red de espines estuviera entrelazada o incluso -inspirándonos en los resultados del capítulo 10- presentara entrelazamiento localizable? Éstas y otras preguntas pueden ser combinadas en el gran objetivo de la tesis, como ya hemos comentado al principio: ¿es posible extraer más sentido de los constructos que utilizamos para caracterizar estados si tenemos protocolos para medirlos? Creemos firmemente que la respuesta a esa pregunta es afirmativa, y que ésta es la justificación de la presente tesis.

2. INTRODUCTION

2.1 What this thesis is about

This thesis is about measuring. Physics has changed the way we think and interact with the world around us. Our understanding of nature has grown at an unprecented accelerating pace in the last couple of centuries. Nowadays, with more professional researchers than ever, theoretical and experimental breakthroughs motivate each other and deal with our universe at scales completely alien to our everyday experience. In these unintuitive realms, and particularly at the quantum scale of the very small, people have come up with increasingly abstract mental constructs to explain what is happening; on the other hand, experiments on this scale are forever giving rise to technological applications that improve (or at least change) our lives. It will be few those who say that the boldest of ideas will never become a factor in some real world application.

In this context, the interface between theory and experiment is more blurry and important than ever. We will defend that -in Physics- nothing truly exists that cannot be measured; that any given concept is not only as powerful as its abilities to describe physical phenomena and simplify the number of assumptions on our physical reality, but also as its identification with “the truth” can be denied in practice.

An important example of the connection between theory and experiment lies in particle physics. The standard model has a deep formalism behind it, in the form of Lorentz invariance restrictions, Yang-Mills theories and spontaneous symmetry breaking mechanisms. However, (almost) all of this theory has to be put down to the more mundane language of scattering cross-sections in order to allow itself to be measured. This translation has given rise to amazing developments in experiment and theory, but sometimes lead to frustration regarding aspects of the model (even 'free' dynamics) that are difficult, or arguably impossible, to explore[1]. This gap is made even more obvious in extensions of the standard model, where many unmeasureable beings are postulated in order to satisfy some aspect of the theory. It is our view that a 'measurement-dictionary' is essential for these theories to be physical.

Similar challenges arise in the growing field lying in the intersection between condensed matter physics and quantum information. In the following chapters we will develop this 'measurement-dictionary' for specific instances of two very wide concepts that are ubiquitous in the understanding of these systems: topology and entanglement. These two words are used a bit too profusely in research in this topic; we will try specify at each point what we exactly mean and what can be *unambigously* measured. We hope that, in this way, the reader has less of a buzzwordy-feeling to them.

The measurement protocols here contained are accompanied by detailed experimental proposals, all of them based on optical lattice technology. Since we deal with phenomena that typically involve many particles -and one can argue that is

---

[1] One can only elucubrate about the existence of right-handed neutrinos, glueballs,...

usually the case for non-local properties[2]- optical lattice offer the required balance between scalability and parameter control. Together with the proposals is a thorough analysis of experimental parameters and requirements needed to implement the setup in hand; with a realistic study of orders of magnitude and the leading decoherence processes.

All in all, we hope this thesis helps to link abstract ideas to measurements and reality for many theoretical physicists, and stimulates further experimental effort in these fields - specially in the cold atom community. It is often the case that knowledge of the existence of a new toy – of the likes of a topological/mbqc-useful atomic cloud – spurs the imagination on what to do with it. Most of all, making this toy is what this thesis is about.

2.2 Overview

The structure of this thesis is as follows: First we have this very introduction, which should provide some motivation as to the guidelines of the work here contained; it provides the minimal information required to know the purpose of the thesis and its units and to succesfully navigate through all its chapters.

Chapters 3 and 4 will review some background information which will be helpful to those readers who are unfamiliar with some parts of the field of research. Specifically, Chapter 3 will review some basic concepts of optical lattice technology, most of which are routinely implemented in experiment. This chapter only contains tools which are used in a proposal further along the thesis, and should not be viewed as a complete report on the capabilities of optical lattices The chapter also contains a section devoted to the implementation of condensed matter tight-binding models, which are one of the success stories of the use of lattices for quantum simulations This sort of models will indeed play an important role in this thesis, since they will constitute the basis of a few experimental proposals in following chapters.

Chepter 4, on the other hand, reviews our working definition of topological order and of a widely used topological invariant: the Chern number. It briefly reviews how this invariant is related to the dimensionality and symmetries of the physical system, and contains two main results that will be used repeatedly: first, that Chern number and a winding number are equivalent in pseudospin models; second, that the winding number is an observable quantity in those systems. The chapter also shows that they are also equivalent to a Berry phase, therefore emphasizing that we are dealing with properties which can be attributed to both a model and a physical state.

Chepter 5 is the first chapter of the body of the thesis. It features the analytical proof of the following theorem: the Chern number of a model which lives in the

---

[2] We are here calling a very small set of spatially separated local measurements local itself, in contrast with the broader approach needed to detect topology or genuine multipartite entanglement.

product space of two spins can be identified with the sum of the winding numbers of both spin species - as long as they are never maximally entangled. This statement can be considered remarkable in both parts: on the one hand, it provides a motivation (though not a complete mathematical description) for the winding number to be considered a full-rights topological invariant on its own, even when the system itself might be way more compplicated (e.g. an interacting system). On the other gand, it provides an intriguing link between the definition of invariants and entanglement, specifically when the partitions might not be necessarily fixed from the start- it also provides a protocol to experimentally measure the Schmidt coefficient of some pseudospin bipartition. The proof is numerically tested in a couple of relevant examples, but its influence is felt along several chapters of the thesis.

Chapter 6 deals with an implementation proposal of a full-flavoured Dirac Hamiltonian (in 2+1 dimensions) purely by intensity modulations of the lattice (which are best built in by using diffraction mask technology). It includes a review of the appearance of massless Dirac particles in the half-filled honeycomb lattice - and how the microscopic parameters of the tight-binding model give rise to all possible terms (mass, abelian fields, and even valley-dependent or coupling terms). Most importantly, there is a very detailed analytical and numerical study of the setup, ranging from the specificities of the state-dependent lattice to the order of magnitude analysis of all the relevant quantities. Moreover, a lengthy section is also devoted to the possible measurement techniques on this kind of setup. It is important to bear in mind that Dirac-cone engineering is the most typical way of implementing topological insulators of many sorts, so it comes as no surprise that this chapter contains the main experimental techniques that will be used in the proposals of the following chapters which deal with topology.

Chapter 7 leans hevily on the previous chapters (specially Chapters 4 and 6) and can be considered one of the main results of this thesis. It contains an experimental proposal to implement and, crucially, measure a topologically ordered state. In order to do this, we suggest to use a slight modification of Haldane's honeycomb lattice model (there is a section highlighting the differences) at half-filling, and then perform time-of-flight measurements of the densities of both pseudospin components. It is shown that an integer winding can be derived from those simple observables, characterizing the topological nature of the state. Full numerical analysis shows the robustness of the invariant to typical imperfections in cold atom experiments.

Chapter 8 contains a proposal to measure topological order in a particle-hole symmetric system (i.e. a topological superconductor). The result which is similar in spirit to that of chapter 7 but takes on two very important conceptual additions: first, the different symmetry class implies using a totally different set of observables; second, the difficulty of implementing p-wave pairing forced us to work our way around the simplest models to arrive to a much richer s-wave paired two-specied model. The consequences are beautiful: the model presents a Chern number 2 phase which signals the presence of Majorana zero modes (which has been an elusive task so far - more on that on the chapter itself), as it is adiabatically connected to Kitaev's honeycomb spin model. Moreover, the use of two species allows us to use directly the results of Chapter 5, making it also an experimental proposal to measure the entanglement spectrum of the system. As the model is more involved, a thorough study of the experimental setup, orders of magnitude and feasibility is provided.

Chapter 9 is a last step in the consequences of being able to measure directly topological phase transitions, and makes full use of the ideas (if not the proof) which guide Chapter 5: it uses a pseudospin invariant to signal the presence of a topological phase transition in a more complicated system (which has a non-abelian phase transitions). It presents a model which has a spin-independent magnetic field coupled to spin-dependent tunneling elements: different transitions appear depending on the presence or absence of time-reversal symmetry. The main result, as long as this thesis is concerned, is that the rich phase diagram can be partially derived from simple time-of-flight measurements. More than everything, this chapter signals the outlook on one of the most promising lines of immediate development based on the ideas of this thesis.

Finally, chapter 10 provides a protocol for measuring genuine multipartite entanglement in an optical lattice. This protocol provides an entanglement witness which can be constructed with only two measurement runs, simplifying over previous protocols whose number of measurements increased with the number of particles. Moreover, the protocol allows for the identification of regions which are highly entangled regardless the rest of the system; this result is useful both from a purely theoretical perspective and from the point of view of experimental calibration. Finally, a experimental proposal is provided, together with a detailed analysis of the main sources of noise and their effect on the measurements.

2.3 PhD scientific contributions

The results explained in this thesis are partially published the following in peer-reviewed papers:

1. *Detection of Chern numbers and entanglement in topological two-species systems through subsystem winding numbers* J. de Lisle, S. De, E. Alba, A. Bullivant, JJ Garcia-Ripoll, V. Lahtinen, and J.K. Pachos, New Journal of Phys. **16**, 083022 (2014)
2. *Topological phase transitions driven by non-Abelian gauge potentials in optical square lattices* M. Burrello, I.C. Fulga, Emilio Alba, L. Lepori, A. Trombettoni, Phys. Rev. A **88**, 053619 (2013)
3. *Seeing Majorana fermions in time-of-flight images of spinless fermions coupled by s-wave pairing* Jiannis K. Pachos, Emilio Alba, Ville Lahtinen, Juan J. García-Ripoll, Phys. Rev. A **88**, 013622 (2013)
4. *Simulating Dirac fermions with Abelian and non-Abelian gauge fields in optical lattices* Emilio Alba, Xavier Fernandez-Gonzalvo, Jordi Mur-Petit, Juan J. García-Ripoll, Jiannis K. Pachos, Annals of Physics **328**, 64-82 (2013)
5. *Seeing topological order in time-of-flight measurements* E. Alba, X. Fernandez-Gonzalvo, J. Mur-Petit, J. K. Pachos, Juan J. García-Ripoll, Phys. Rev. Lett. **107**, 235301 (2011)
6. *Mapping the spatial distribution of entanglement in optical lattices* Emilio Alba, Geza Toth, Juan J. García-Ripoll, Phys. Rev. A **82**, 062321 (2010)

Other related results published in peer-reviewed journals by the autor of this thesis are:

1. *Generating and verifying graph states for fault-tolerant topological measurement-based quantum computing in 2D optical lattice* Jaewoo Joo, Emilio Alba, Juan J. García-Ripoll, Timothy P. Spiller, Phys. Rev. A **88**, 012328 (2013)
2. *Hall response of interacting bosonic atoms in strong gauge fields: From condensed to fractional-quantum-Hall states* H. Pino, E. Alba, J. Taron, J. J. Garcia-Ripoll, N. Barberan, Phys. Rev. A **87**, 053611 (2013)

Some of the results have also been presented publicly at the following national and international conferences:

1. *Seeing topological order: topological insulators and topological superconductors* E.Alba. Talk, Biannual Meeting of the Spanish Royal Society of Physics, Valencia (ES), Jul. 2013

2. *Seeing Majorana fermions in time-of-flight images of spinless fermions coupled by s-wave pairing* E. Alba. Poster, Workshop on Quantum Simulations, Bilbao (ES), Oct 2012
3. *Seeing topological order in time-of-flight measurements* E.Alba. Talk, Workshop on Topological States of Matter, Freiburg (DE), March 2012
4. *Mapping the spatial distribution of entanglement in optical lattices* E.Alba. Talk, Biannual Meeting of the Spanish Royal Society of Physics, Santander (ES), Sept. 2011
5. *Mapping the spatial distribution of entanglement in optical lattices* E.Alba. Poster, POLATOM Meeting, Hersonissos, Crete (GR), May 2011
6. *Abelian and non-Abelian fields in optical lattices* E.Alba. Talk, Workshop on Quantum Simulations, Benasque (ES), March 2011

3. OPTICAL LATTICES

3.1 Summary

Optical lattices are maleable and controllable devices which have been used for everything from simulations of condensed matter physics models to single-qubit manipulation to measuring low-energy properties of particle physics theories. Its many-body nature, together with the high degree of control achieved in quantum optics, have sparked the imagination of theoreticians and experimentalists alike. Optical lattices are, in short, one of the most promising candidates for the holy grail of the all-purpose quantum computer/simulator. All results contained in this thesis are obtained with the capabilities and limitations of ultracold atoms technology in mind. Therefore, this chapter is meant as a brief review of optical lattices for the uninitiated, and as a common base for the explanation of the results contained hereinafter. Please consider reading more complete references ([15],[62]) for a thorough understanding of the matter.

3.2 Light-matter interaction

This section will explain how neutral atoms can feel a potential which depends on the intensity profile of the radiation field, which typically consists on a set of laser beams. Our starting point will be the Hamiltonian of a two-level neutral atom immersed in an electromagnetic field, which will be described semiclassically. The Hamiltonian for the particle is:

$$\hat{H}_{atom} = \frac{\hat{\boldsymbol{p}}^2}{2m} + \frac{\hbar\omega_0}{2}\left(\left|e\right\rangle\left\langle e\right| - \left|g\right\rangle\left\langle g\right|\right), \tag{3.1}$$

where $(\left|g\right\rangle, \left|e\right\rangle)$ are the ground and excited internal states of the atom, separated by an energy $\hbar\omega_0$. The semiclassical interaction between atom and radiation field is due to the eletric dipolar force, to first order:

$$\hat{H}_{int} = -\hat{\boldsymbol{d}} \cdot \boldsymbol{E}. \tag{3.2}$$

The dipole moment operator only depends on the spatial distribution of the electronic wavefunction in the internal energy levels:

$$\hat{\boldsymbol{d}} = \boldsymbol{d}\left|g\right\rangle\left\langle e\right| + \boldsymbol{d}^\star\left|e\right\rangle\left\langle g\right|, \quad \boldsymbol{d} = \left\langle g\right|\hat{\boldsymbol{d}}\left|e\right\rangle \quad \left(\left\langle g\right|\hat{\boldsymbol{d}}\left|g\right\rangle = \left\langle e\right|\hat{\boldsymbol{d}}\left|e\right\rangle = 0\right). \tag{3.3}$$

The kinetic term commutes with the rest of terms in the Hamiltonian, and can safely be ignored for the rest of the discussion. However, it is important to bear in mind that the atoms loaded into the lattice must be drastically cooled (in the $nK - \mu K$ range) in order to have an energy lower or comparable to that of typical optical lattices.

We simplify our problem further by considering the field to be coherent and monochromatic, $\boldsymbol{E} = E_0(\boldsymbol{r})\vec{\epsilon}e^{i\omega_L t} + E_0^\star(\boldsymbol{r})\vec{\epsilon}^\star e^{-i\omega_L t}$. We rewrite the atom-field

Hamiltonian in the interaction picture defined by the natural internal-state frequency ($U_I = \exp(i\omega_0/2\,(|e\rangle\langle e| - |g\rangle\langle g|))$):

$$\hat{H}_{int} = -\left(e^{-i\omega_0 t}\boldsymbol{d}\,|g\rangle\langle e| - e^{i\omega_0 t}\boldsymbol{d}^\star\,|e\rangle\langle g|\right)\left(E_0(\boldsymbol{r})\vec{\epsilon}e^{i\omega_L t} + E_0^\star(\boldsymbol{r})\vec{\epsilon}^\star e^{-i\omega_L t}\right) \tag{3.4}$$

We further assume that the frequency of the beam is resonant with the atomic transition ($\Delta = w_L - w_0 \ll w_0$) so we can apply the Rotating Wave approximation; thus discard all terms which, in the interaction picture, oscillate with a frequency higher that Δ:

$$\hat{H}_{int}^{RWA} = -\hbar\left(e^{it\Delta}\Omega(\boldsymbol{r})\,|g\rangle\langle e| + e^{-it\Delta}\Omega^\star(\boldsymbol{r})\,|e\rangle\langle g|\right), \tag{3.5}$$

where we have defined the Rabi frequency $\Omega(\boldsymbol{r}) = E_0(\boldsymbol{r})\boldsymbol{d}\cdot\vec{\epsilon}/\hbar$. Transforming back into the Schrödinger picture, the Hamiltonian (less the kinetic term) reads:

$$\hat{H} = \frac{\hbar\omega_0}{2}\left(|e\rangle\langle e| - |g\rangle\langle g|\right) - \hbar\left(e^{it\omega_L}\Omega(\boldsymbol{r})\,|g\rangle\langle e| + e^{-it\omega_L}\Omega^\star(\boldsymbol{r})\,|e\rangle\langle g|\right), \tag{3.6}$$

The effect of the interaction is easier to understand if we treat it perturbatively. First we must get rid of the time dependence by doing a change of basis:

$$\begin{pmatrix} |g\rangle \\ |e\rangle \end{pmatrix} \to U\begin{pmatrix} |g\rangle \\ |e\rangle \end{pmatrix}, \quad U = \begin{pmatrix} e^{it\omega_L/2} & 0 \\ 0 & e^{-it\omega_L/2} \end{pmatrix} \tag{3.7}$$

and transform the Hamiltonian accordingly:

$$\hat{H} \to U\hat{H}U^\dagger + i\frac{dU}{dt}U^\dagger. \tag{3.8}$$

The resulting Hamiltonian (in the basis which co-rotates with the laser frequency) is

$$\hat{H} = -\frac{\hbar\Delta}{2}\left(|e\rangle\langle e| - |g\rangle\langle g|\right) - \hbar\left(\Omega(\boldsymbol{r})\,|g\rangle\langle e| + \Omega^\star(\boldsymbol{r})\,|e\rangle\langle g|\right), \tag{3.9}$$

The perturbative coupling regime requires then $|\Omega| \ll |\Delta|$, where a second-order energy correction is added to the bare internal state energies:[1]

$$\begin{aligned} \Delta E_g(\boldsymbol{r}) &= \sum_{\Psi\neq g}\frac{|\langle g|\,H_{int}\,|\Psi\rangle|^2}{E_g^{(0)} - E_\Psi^{(0)}} = \hbar\frac{|\Omega(\boldsymbol{r})|^2}{\Delta}, \\ \Delta E_e(\boldsymbol{r}) &= \sum_{\Psi\neq e}\frac{|\langle e|\,H_{int}\,|\Psi\rangle|^2}{E_e^{(0)} - E_\Psi^{(0)}} = -\hbar\frac{|\Omega(\boldsymbol{r})|^2}{\Delta}. \end{aligned} \tag{3.10}$$

Summing up, the effect of the off-resonant light on the atom is to exert a conservative force that can be described by an effective potential, $V(\boldsymbol{r}) \propto \hbar|\Omega(\boldsymbol{r})|^2/\Delta$. Since the Rabi frequency is proportional to the intensity of the field, $|\Omega(\boldsymbol{r})|^2 \propto$

---

[1] Strictly speaking, one should aleady demand that $|\Omega| \ll \omega_0$ in order to apply the RWA. This is safely the case for all standard optical lattice experiments.

$|E_0(\boldsymbol{r})|^2 = I(\boldsymbol{r})$, the atom will be attracted to the intensity minima for $\Delta > 0$, or blue detuning. If $\Delta < 0$ (red detuning) the potential will have its minima at the maxima of the field intensity. A cubic optical lattice can thus be created by a standing-wave configuration of the laser beam, $I(\boldsymbol{r}) \propto \cos^2(k_x x)\cos^2(k_y y)\cos^2(k_z z)$, with a depth of the potential wells that is set by the intensity of the laser beam ($V_0 \simeq \hbar|\Omega(\boldsymbol{r})|^2/|\Delta|$).

Finally, it will be useful to estimate the rate of inelastic processes -heating- arising from the incoherent decay of the population in the excited internal state. This sponatenous emission process is characterized by the inverse of the excited state lifetime Γ_e, and the total heating rate will be proportional to the expected occupation of the bare excited state, $\gamma_{heat} \simeq \Gamma_e|\langle\Psi|e\rangle|^2$. In our ultracold atom setting, $|\Psi\rangle$ will be the ground state of our effective two-level Hamiltonian(3.9), where $|\langle\Psi_{GS}|e\rangle|^2| \sim |\Omega(\boldsymbol{r})|^2/\Delta^2$ for $|\Omega| \ll |\Delta|$. Therefore our total heating rate can be roughly estimated at this level of approximation as:

$$\gamma_{heat} \sim \Gamma_e \frac{|\Omega(\boldsymbol{r})|^2}{\Delta^2} = \Gamma_e \frac{V_o}{\hbar|\Delta|}. \tag{3.11}$$

Experimentally, the heating rate and the scale of energy hierarchies implied by this approximations ($\omega_0 \gg |\Delta| \gg |\Omega|$) are key ingredients in selecting the atomic species and laser frequency and power output. It is important to notice that a large detuning is needed to keep a low heating rate together with a deep potential well. However, we will see that in certain setups (e.g. the state-dependent lattices we will see in some proposals of this thesis) the maximum detuning is fixed and thus one must find a compromise between having a low heating rate and non-trivial dynamics in the lattice, and a detailed analysis of the setup is specially indicated in those cases.

3.3 Optical lattices

Neutral atoms can be cooled down to temperatures where the energy scale of the potential created by the laser beams is dominant. The main way to achieve this ultracold temperatures is through the use of a magneto-optical trap (MOT), which combines a magnetic quadrupole field with beams for laser cooling (for details, see [67]). Without any other fields, this cloud is constrained by an overall harmonic potential. This potential can be made different in the three directions of space, allowing for effective uni-dimensional and bi-dimensional setups.

However, we have seen in the previous section that neutral matter can feel a potential when a strong enough laser beam shines on the cloud; the potential is directly proportional to the spatial intensity profile of the beam (see Eq. 3.10). The simplest way to achieve a non-trivial profile is to shine a beam against a mirror in order to obtain a standing wave pattern: $I(\boldsymbol{r}) \propto \sin^2 x$. This periodic potential can be engineered in one, two or three dimensions, trapping the atoms in the minima of the potential well (see Fig. 3.1).

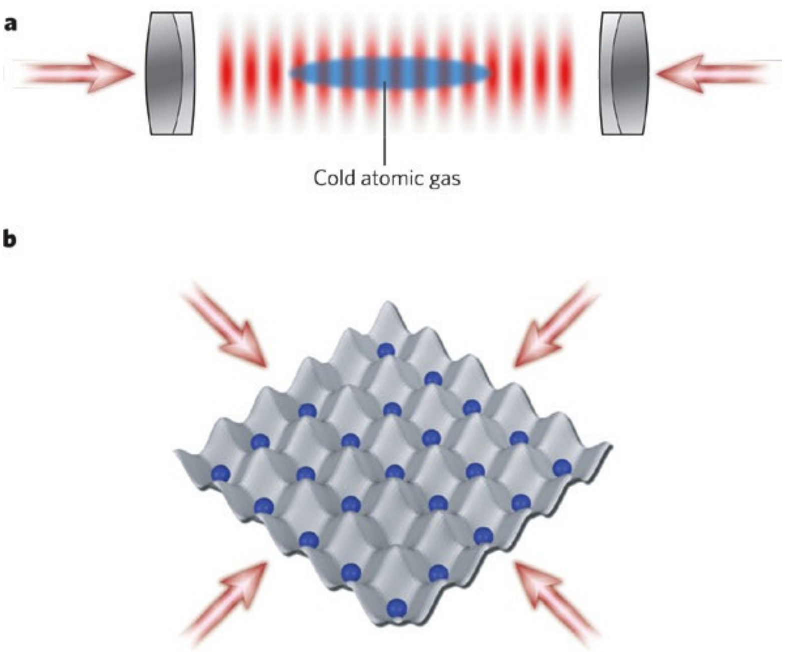

Fig. 3.1: a) Sketch of a standing wave spatial pattern (nodes in red) on top of an ultracold atomic cloud. b) Sketch of a bidimensional optical lattice. Atoms tend to lie at the minima of the potential wells. Figure taken from Ref.[15]

It is also possible to recreate more complicated potentials by adding more beams or using different techniques. We will see in chapter 6 more on how to engineer complicated optical lattices in 2D.

3.4 Tight-binding models

The natural periodic-potential structure of optical lattices is specially fit for addressing solid state problems. This section will review the behaviour of a single particle in a lattice potential, along with some basic charateristics of the interaction between cold atoms; and will present the tight-binding family of models.

A cold atom in an optical lattice of any geometry will have a Hamiltonian governing its dynamics:

$$\hat{H} = \frac{\hat{\boldsymbol{p}}^2}{2m} + V_{lat}(\boldsymbol{r}). \tag{3.12}$$

The defining propoerty of a lattice potential is that it is periodic in some dimension(s), with a lattice spacing set by a vector (or set of vectors) $\boldsymbol{a}_i$:

$$V_{lat}(\boldsymbol{r}) = V_{lat}(\boldsymbol{r} + \boldsymbol{a}_i). \tag{3.13}$$

Bloch's theorem states that the wavefunctions Ψ which are eigenstates of this Hamiltonian are also periodic -with the same periodicity- up to a phase:

$$\Psi(\boldsymbol{r}) = e^{i\boldsymbol{k}\cdot\boldsymbol{r}} u_{\boldsymbol{k},n}(\boldsymbol{r}), \quad u_{\boldsymbol{k},n}(\boldsymbol{r}) = u_{\boldsymbol{k},n}(\boldsymbol{r} + \boldsymbol{a}_i), \tag{3.14}$$

where the periodic function $u(\boldsymbol{r})$ depends on the specifics of the potential and can be solved for by using the Schrödinger equation. The wavevector $\boldsymbol{k}$ can be seen as the quantum number which lists all possible eigenfunctions of the Hamiltonian, and it is called quasimomentum[2]. Quasimomenta are periodic, with a periodicity which is inversely proportional to the lattice spacing; the set of unique quasimomenta which are closer to $\mathbf{0}$ is called the first Brillouin Zone. The other quantum number is the 'band index' number n, which labels the set of eigenstates for any given quasimomentum $\boldsymbol{k}$. In the thermodynamic (infinite lattice) limit, any given n specifies a continuous energy field $E_n(\boldsymbol{k})$ on the Brillouin Zone. For the remainder of this thesis, unless otherwise specified, we will deal with the properties of the lowest energy band and omit the band index number.

The Bloch basis has the property that it is strictly delocalized, that is, any eigenstate fulfills $|\Psi_{\boldsymbol{k}}(\boldsymbol{r})|^2 = |\Psi_{\boldsymbol{k}}(\boldsymbol{r}+\boldsymbol{R})|^2$ for any lattice vector $\boldsymbol{R} = \sum n_i \boldsymbol{a}_i$. If we want to work with localized wavefunctions, we consider their discrete Fourier transform to obtain the *Wannier* basis:

$$w_{\boldsymbol{R}}(\boldsymbol{r}) = \frac{1}{\sqrt{N_{sites}}} \sum_{\boldsymbol{k}} e^{i\boldsymbol{k}\cdot\boldsymbol{R}} \Psi_{\boldsymbol{k}}(\boldsymbol{r}). \tag{3.15}$$

These functions also form a basis $\langle w_{\boldsymbol{R}} | w_{\boldsymbol{R'}} \rangle = \delta_{R,R'}$ and are localized in the intuitive sense (i.e. $|w_{\boldsymbol{R}}(\boldsymbol{r})|^2$ peaks at $|\boldsymbol{r}-\boldsymbol{R}| \sim 0$ and goes to zero for $|\boldsymbol{r}-\boldsymbol{R}| \to \infty$) under reasonable assumptions ([96]).

When the atoms loaded in the lattice are cold enough to stay in the lowest energy band, and the potential is deep enough, it is reasonable to think that the single-particle wavefunctions will be adequately described by localized Wannier functions. We will now formalize this idea by second-quantizing our single-particle Hamiltonian 3.12 making use of the Wannier functions.

We introduce the single particle creation (annihilation) operators for a particle described by a Wannier function in site i, $\hat{c}_i^\dagger$,($\hat{c}_i$); these operators will obey Bose or Fermi statistics depending on the nature of chosen atomic species. In this language, our single-particle Hamiltonian is written as:

$$\hat{H} = \sum_i \epsilon_i \hat{c}_i^\dagger \hat{c}_i + \sum_{i,j} J_{i.j} \hat{c}_i^\dagger \hat{c}_j. \tag{3.16}$$

The set of parameters which describe the Hamiltonian (the on-site potential ϵ_i and the hopping element $J_{i,j}$ are computed by using the first-quantized single particle

---

[2] Its meaning is clearer if we note that the Hamiltonian commutes with the set of dicrete translation operators $\mathcal{T}(n_i \boldsymbol{a}_i)$, and $\vec{k}$ is the eigenvalue of the generator of these translations. In analogy with the momentum being the eigenvalue of the generator of continuous translations, the wavevector $\vec{k}$ is called the quasimomentum. Unlike continuous translations, the fact that the minimum lattice translation is set by the lattice spacing upper-bounds the different possible value of quasimomenta. The set of independent quasimomenta quantum numbers is called a Brillouin Zone.

Hamiltonian written in Eq. 3.12 (herein labelled h_{sp}):

$$\begin{aligned} \epsilon_i &= \int d\boldsymbol{r}\, w^{\star}_{\boldsymbol{R_i}}(\boldsymbol{r}) h_{sp} w_{\boldsymbol{R_i}}(\boldsymbol{r}), \\ J_{i,j} &= \int d\boldsymbol{r}\, w^{\star}_{\boldsymbol{R_i}}(\boldsymbol{r}) h_{sp} w_{\boldsymbol{R_j}}(\boldsymbol{r}). \end{aligned} \tag{3.17}$$

These integrals cannot be computed analytically even with simple separable potentials. However, some information can be readily extracted: if the potential is translationally invariant with the lattice periodicity, all on-site energies ϵ_i will be the same, and they can be regarded as a zero mark for the chemical potential and dismissed. The hopping element is more complicated, but, *if the lattice is deep enough*, the Wannier function falls off at the same exponential rate as the Gaussian wavefunction of an isolated potential well[3]. Thus, the only non-negligible contributions will be that of neighbouring lattice sites, for want of a more dominant energy scale:

$$\hat{H} \approx \sum_{\langle i.j \rangle} J_{i,j} \hat{c}_i^{\dagger} \hat{c}_j. \tag{3.18}$$

The case of a sinusoidal potential ($V_{lat} = V_0 \sin^2(x)$) allows for a good numerical fit of the tunneling parameter as a function of the lattice depth:

$$\tilde{J} \approx C \tilde{V}_0^{\alpha} e^{-\beta \sqrt{\tilde{V}_0}}, \tag{3.19}$$

where all energy units have been adimensionalized by means of the recoil energy, $E_R = \hbar^2 / 2 m_{atom} c^2 \omega_L^2$. Several fits are available, but they roughly agree at $C \approx 1.4$, $\alpha \approx 1$ and $\beta \approx 2.1$.

The models in which the second-quantized Hamiltonian is described by a sum of local terms are called *tight-binding models* [11]. The use of tight-binding Hamiltonians is common in the literature of optical lattice simulations, and will appear ubiquitously along this thesis[4].

A final common ingredient in lattice models are particle interactions. While real materials feature long-range Coulomb forces, ultracold neutral atoms only see each other via 'head-on' s-wave scattering; that is, the two body potential goes as a delta function: $V(\boldsymbol{r}, \boldsymbol{r'}) \propto \delta(\boldsymbol{r} - \boldsymbol{r'})$. The strength of the interaction is typically parametrized by a single quantity, the scattering length a_s:

$$V(\boldsymbol{r}, \boldsymbol{r'}) \approx \frac{4\pi\hbar^2 a_s}{m_{atom}} \delta(\boldsymbol{r} - \boldsymbol{r'}). \tag{3.20}$$

---

[3] This result is only proven analytically for some separable symmetric potentials, a notable exception to which is the honeycomb lattice. However, numerical simulations tend to confirm that there is a reasonable "deep enough" for these kind of potentials too.

[4] Despite the name, the solutions of a tight-binding Hamiltonian need not be localized or "tightly bounded" whatsoever. In fact, the solutions of Hamiltonian 3.18 consist on completely delocalized wavefunctions (superfluid).

The scattering length can be measured experimentally and characterizes attractive ($a_s < 0$) and repulsive ($a_s > 0$) interactions.

The delta function description of the potential clearly restricts the interaction to particles in the same lattice site; be it bosons or fermions with different internal states. The two-body term in second quantization – here we consider bosonic operators for a less cumbersome notation – is thus:

$$\hat{H}_{int} = \frac{1}{2} U \sum_i \hat{n}_i (\hat{n}_i - 1), \tag{3.21}$$

where $U = 4\pi\hbar^2 a_s \int d\boldsymbol{r}\, |w_{\boldsymbol{R}}(\boldsymbol{r})|^4 / m_{atom}$. Here again the specfics of the interaction between cold atoms makes them convenient for the simulation of tight-binding Hamiltonians.

3.5 Light assisted tunneling

We have so far dealt with the behaviour of confined ultracold atoms in the presence of a potential generated by a light intensity pattern. This problem is rich in itself, and allows, among other things, for the simulation of many tight-binding Hamiltonians. However, there is one important extra tool that has become a standard in theoretical proposals and is taking off experimentally ([48, 4]): the addition of artificial tunneling (kinetic) terms with the help of additional laser beams, typically with the intention of simulating magnetic fields. This ingredient will be commonplace along the following chapters.

The origin of this idea is a work by Jaksch and Zoller ([48]), which was precisely put forward for simulating the Hall effect with neutral atoms, and is still the best read to become acquainted with the technique. For completitude, we will devote this section to a brief description of the quantum optics and the effective dynamics involved.

The scheme needs the atomic species chosen for the experiments to have at least two stable internal levels so that each of them admits being trapped in a lattice potential. There are two main approaches for optically coupling these two states: directly driving the transitions (which needs the on-site energy of the two lattices to be far apart) or through a third excited state (which can give rise to heating problems). In the following, we will explain the second method.

As it can be seen in Fig. 3.5, we will consider that we have two internal states (labelled $|a\rangle$ and $|b\rangle$) of the same atomic species and we want two drive transitions between them. We assume their energy separation ϵ is too small to be addressed by an optical frequency, so we use a third excited state ($|v\rangle$) and two laser beams (with frequencies ω_1 and ω_2) to couple them via an off-resonant two-photon process, described by the following Hamiltonian (the energy scales are those shown in

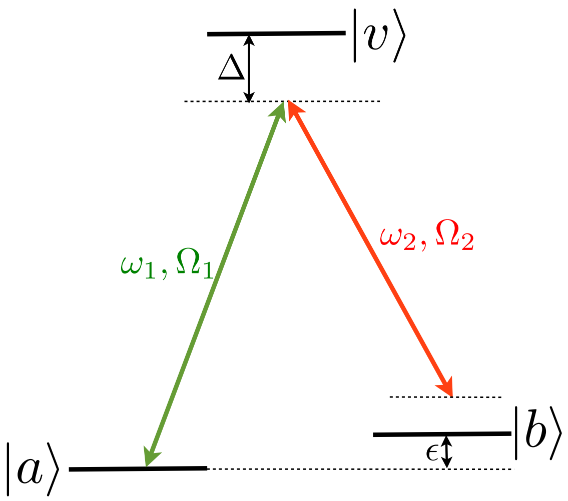

Fig. 3.2: Energy level structure for a light-assisted tunneling scheme. $|a\rangle$ and $|b\rangle$ are the two internal states trapped by the two superimposed optical lattices. The two beams have frequencies ω_1, ω_2 and Rabi couplings Ω_1, Ω_2 which need not carry the same phase. The virtual level $|v\rangle$ is so far detuned we can consider its population rate is negligible.

Fig. 3.5):

$$\begin{aligned}\hat{H} &= \hbar\epsilon\,|b\rangle\langle b| + \hbar(\omega_1+\Delta)\,|v\rangle\langle v| \\ &- \hbar\left(\Omega_1(\boldsymbol{r})e^{-i\omega_1 t}\,|a\rangle\langle v| + \Omega_1^\star(\boldsymbol{r})e^{i\omega_1 t}\,|v\rangle\langle a|\right) \\ &- \hbar\left(\Omega_2(\boldsymbol{r})e^{-i\omega_2 t}\,|b\rangle\langle v| + \Omega_2^\star(\boldsymbol{r})e^{i\omega_2 t}\,|v\rangle\langle b|\right). \end{aligned} \tag{3.22}$$

Using the “co-rotating basis” approach of Sec. 3.2, we can reduce this expression to an equivalent time-independent Hamiltonian:

$$\begin{aligned}\hat{H} &= \hbar\Delta\,|v\rangle\langle v| + \hbar\delta\,|b\rangle\langle b| \qquad (3.23) \\ &- \hbar\left(\Omega_1(\boldsymbol{r})\,|a\rangle\langle v| + \Omega_1^\star(\boldsymbol{r})\,|v\rangle\langle a|\right) - \hbar\left(\Omega_2(\boldsymbol{r})\,|b\rangle\langle v| + \Omega_2^\star(\boldsymbol{r})\,|v\rangle\langle b|\right),\end{aligned}$$

where $\delta = \epsilon + \omega_2 - \omega_1$. Now we assume $|\Delta| \gg |\delta|, |\Omega_1|, |\Omega_2|$ and perform an *adiabatic elimination* of the virtual excited state to obtain an effective two-level Hamiltonian[5]:

$$\hat{H}/\hbar = -\frac{|\Omega_1|^2}{4\Delta}\,|a\rangle\langle a| + \left(\delta - \frac{|\Omega_2|^2}{4\Delta}\right)|b\rangle\langle b| + \frac{\Omega_1\Omega_2^\star}{2\Delta}\,|a\rangle\langle b| + \frac{\Omega_1^\star\Omega_2}{2\Delta}\,|b\rangle\langle a|. \tag{3.24}$$

This Hamiltonian contains a slight energy offset for each internal state and, more importantly, an effective coupling between them. Two very important features of this Raman process are worth mentioning: first, the on-site chemical potential

---

[5] This procedure is based on the idea that, if the virtual state starts unpopulated, its population rate will be negligible compared to all other energy scales. This is standard practice, but a rigorous approach can be found in [18]

difference between the $|a\rangle$ and $|b\rangle$ species can in principle be controlled by adjusting the laser beams frequencies (ω_1, ω_2); second, the effective coupling mat carry a complex phase. Therefore, we can (and will along this thesis) use two different lattices to create one superlattice in which the tunneling elements can be imaginary.

3.6 Measurements: real space and time-of-flight

The central idea of this thesis is that the optical lattice quantum simulator allows measuring novel properties of a many-body state that were not accessible in the models or systems where such Physics was originally discovered. In this section we review the two main measurement procedures which we will assume are available in our proposals: real-space (fluorescence) imaging and momentum-space (time-of-flight) imaging.

3.6.1 Fluorescence imaging

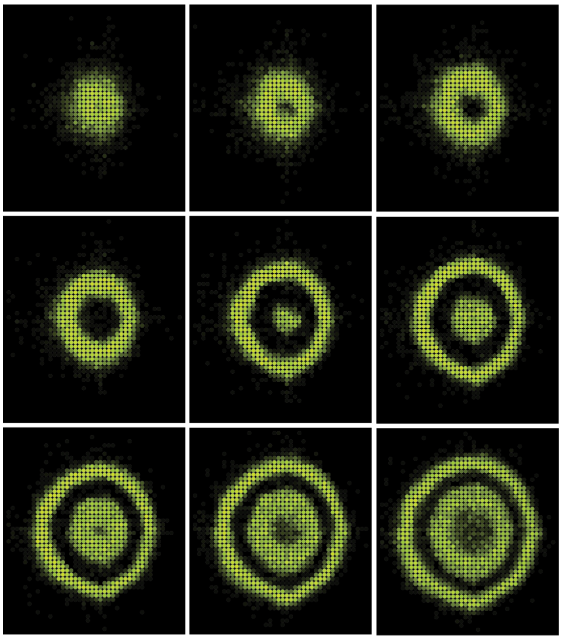

Fig. 3.3: Single-site imaging of the shell structure in a Mott insulator; in this case, a dark spot means there is an even number of atoms in that lattice site, while a bright spot signals the presence of an odd number of atoms. Figure taken from Ref.[13]

While intuitively the most desirable, single-site density measurements need a spatial resolution of half the wavelength of the beam which creates the optical lattice. This subwavelength imaging needs the fluorescent light to be collected by a very powerful microscope - the numerical aperture of the lens has to be near unity. This experimental restrictions have only recently been fulfilled in bidimensional setups, either by using a high-resolution objective very close to the optical lattice plane ([97]) or by using the lens itself to create the optical lattice on its focal plane ([14]), as it can be seen in Fig. 3.3.

Assuming that it is possible to resolve distances of the order of the latting spacing, fluorescence imaging is a straight-forward tool that is used in other systems (such as trapped ions).

3.6.2 Time-of-flight imaging

An older, much more standard, measurement technique in optical lattice experiments is time-of-flight imaging. Conceptually, this amounts to a density measurement in Fourier space (i.e. measuring $|\Psi(\boldsymbol{k})|^2$). Experimentally, the lattice is abruptly switched off and the atoms fall freely in an assumed ballistic regime (that is, there are no collisions between the atom and the motion is uniform). After a "long" time of flight (in the far-field approximation, for $t_{tof} \gg m/2\hbar a^2$), a real space image of the atomic cloud (e.g. an absorption image) is taken by means of a CCD camera. In this approximation the spatial density profile of the cloud is the same as the lattice quasimomentum distribution, $\langle \hat{n}_{tof}(\boldsymbol{r})\rangle \propto \langle \hat{n}_{lat}(\boldsymbol{k})\rangle$. Classicaly speaking, one can say that, by freeing the atoms, the quasimomentum quantum number of a particle *becomes* its real momentum, and thus determines the particle's position after a long time of ballistic expansion.

4. CHERN NUMBER AND OBSERVABLE WINDING NUMBERS IN 2D SYSTEMS

4.1 Summary

Recent theoretical and experimental developments have sparked the interest for a set of states of matter. This set, called *topological* states of matter, refer to a wide range of systems which share the impossibility of characterizing the phase by local measurements. The consequences are many, from conducting edges in insulating samples to exotic low-energy excitations which do not feature standard bosonic/fermionic statistics. This chapter will focus on the Chern number classification of pseudospin systems, and show its equivalence to a winding number in the pseudospin language.

4.2 Chern numbers in 2D systems

The first indication that the abstract concept of a topological space was of physical interest came in by the TKNN description of the integer Hall effect ([91]). This paper showed that the quantized conductivity could be understood in terms of invariant integers arising from linear response theory, by computing the conductivity through the Kubo formula. A more physical way of explaining this integer quantization is that, for a filled isolated band with non-zero integer, the wavefunction cannot be continuous over the Brillouin zone. There is a beautiful correspondence between these necessary discontinuities and the number of conducting modes at the edge - between the Chern number of the band and the quantized conductivity of the sample. Recently (see, for example, [41]) this concept of topology and bulk-boundary correspondence has been at the heart of a huge development – and controversy– in theoretical and experimental condensed matter physics.

In order to define better what do we mean by topology in this context, we will first comment on a couple of mathematical facts about the systems we will be considering in this thesis. First, any state of non-interacting particles in a lattice can be fully described in term of wavefunctions over the periodic Brillouin Zone. The Brillouin Zone, in a bidimensional system, has the structure of a 2-periodic, orientable manifold; it is topologically identical to a torus. Secondly, any translationally-invariant *gapped* model is defined by a Hamiltonian operator at each point of the torus; in our finite-dimensional case the operator is represented by an element in the space of n-by-n *non-degenerate* complex Hermitian matrices, $\mathcal{M}_n(\mathbb{C})$. In this language, we will call a model *topological* if the map from the torus to its $\mathcal{M}_n(\mathbb{C})$ submanifold is not null-homotopic ([10]). A necessary condition for the model to be topological in this sense is that a particular characteristic of this "matrix field" on the torus, the Chern number, is non-zero.

A more quantitative view on the subject might be of order: for any given energy band there is a mapping from the torus to the projection operator onto the band, P. A Chern 2-form ω can be defined on each point of the torus, and the Chern number ν will be the integration along the torus of the form $\nu \equiv \int_{T^2} \omega$.) This form can be written in terms of the projector ([12]), so we arrive to a operating formulation:

$$\nu = \frac{1}{2\pi i}\int_{T^2} Tr[P(dP \wedge dP)]. \tag{4.1}$$

The integrand corresponds to a Berry curvature, where the quasimomentum $\vec{k}$ acts as a parameter space.

In our pseudospin case, we deal with just $\mathcal{M}_2(\mathbb{C})$, which is isomorphic to a 2-sphere (the Bloch sphere). Here it is equivalent to work with the projector P or the Hamiltonian, and the physical picture of the null-homotopic classification is clearer: maps from the torus to the sphere are non-trivial, while maps from the torus to a sphere *without at least a point* are trivial.

4.3 Winding numbers in pseudospin systems

An equivalent way to analyze whether a map from the torus to $\mathcal{M}_2(\mathbb{C})$ (a translationally invariant Hamiltonian on the lattice) is trivial or not is through the concept of winding number. While an intuitive concept on a circle, a winding number (also called the degree of a mapping) can be defined for all continous mappings between manifolds of the same dimension, as it happens with the torus and the sphere. A more appropriate name in this case would be "wrapping number": if the torus is mapped to an open subset of the sphere the invariant is zero, if it is mapped to the whole sphere it is one[1]. However, we will stick with "winding number" in this thesis.

We will now compute a formula for the winding number of a 2x2 Hamiltonian. A representation of $\mathcal{M}_2(\mathbb{C})$ can be given in term of the Pauli matrices, $H(\boldsymbol{k}) = \sum_i S_i(\boldsymbol{k})\sigma_i$, for $i = x, y, z$ and $\boldsymbol{S}(\boldsymbol{k})$ some set of coefficients. We can safely ignore the identity term since we only consider gapped Hamiltonians, and we assume $|\boldsymbol{S}| = 1$ (if this is not the case, and since $\sum_i |\boldsymbol{S}| \neq 0$ in gapped Hamiltonians, we simply normalize $\boldsymbol{S}$). From now one, we will denote that normalized field by $\boldsymbol{n}(\boldsymbol{k}) = \boldsymbol{S}/|\boldsymbol{S}|$.

In this parametrization, the projector onto the ground state is (summation convention is assumed):

$$P = \frac{1}{2}\left(\mathbb{1} - n_i\sigma^i\right) \to \mathrm{d}P = -\frac{1}{2}\sigma^i \mathrm{d}n_i. \tag{4.2}$$

And the Chern number, in the form of Eq. (4.1), is expressed as:

$$\nu = \frac{-i}{8\pi}\int \mathrm{Tr}\left[n_i\sigma^i\left(\sigma^j\sigma^l\,\mathrm{d}n_j \wedge \mathrm{d}n_l\right)\right] + \frac{i}{8\pi}\int \mathrm{Tr}\left[\left(\sigma^j\sigma^l\,\mathrm{d}n_j \wedge \mathrm{d}n_l\right)\right]. \tag{4.3}$$

Using the properties of differential forms (and omitting the wedge symbol):

$$\mathrm{d}n = \frac{\partial n}{\partial k_x}\mathrm{d}k_x + \frac{\partial n}{\partial k_y}\mathrm{d}k_y, \quad \mathrm{d}k_x^2 = \mathrm{d}k_y^2 = 0, \quad \mathrm{d}k_x\mathrm{d}k_y = -\mathrm{d}k_y\mathrm{d}k_x, \tag{4.4}$$

---

[1] Since we have a mapping between oriented manifolds, the invariant can be negative; we will consider "physically equivalent" those mappings with the same winding number in absolute value.

we arrive to the equivalent formulation:

$$\nu = \frac{-i}{8\pi}\int \mathrm{Tr}\left[\sigma^i\sigma^j\sigma^l\right] n_i \left(\frac{\partial n_j}{\partial k_x}\frac{\partial n_l}{\partial k_y} - \frac{\partial n_j}{\partial k_y}\frac{\partial n_l}{\partial k_x}\right)\mathrm{d}k_x\mathrm{d}k_y. \tag{4.5}$$

The second term in Eq. (4.3) has vanished since the wedge product vanishes for equal indices, while the trace of the product of two Pauli matrices vanishes for different indices. The trace over the product of three Pauli matrices can be simplified using the Levi-Civita tensor and the property $\mathrm{Tr}\left[\sigma\right] = 0$:

$$\sigma_a\sigma_b = i\sigma_c\epsilon^{abc} + \delta_{ab} \rightarrow \mathrm{Tr}\left[\sigma^i\sigma^j\sigma^l\right] = i\epsilon^{jlc}\mathrm{Tr}\left[\sigma^i\sigma_c\right] = 2i\epsilon^{jlc}\delta^i_c = 2i\epsilon^{ijl}. \tag{4.6}$$

Therefore:

$$\begin{aligned}\nu &= \frac{1}{4\pi}\int \epsilon^{ijl} n_i(\boldsymbol{k})\left(\frac{\partial n_j}{\partial k_x}\frac{\partial n_l}{\partial k_y} - \frac{\partial n_j}{\partial k_y}\frac{\partial n_l}{\partial k_x}\right)\mathrm{d}k_x\mathrm{d}k_y \\ &= \frac{1}{4\pi}\int \boldsymbol{n}(\boldsymbol{k})\cdot\left(\frac{\partial \boldsymbol{n}(\boldsymbol{k})}{\partial k_x}\times\frac{\partial \boldsymbol{n}(\boldsymbol{k})}{\partial k_y}\right)\mathrm{d}k_x\mathrm{d}k_y. \end{aligned} \tag{4.7}$$

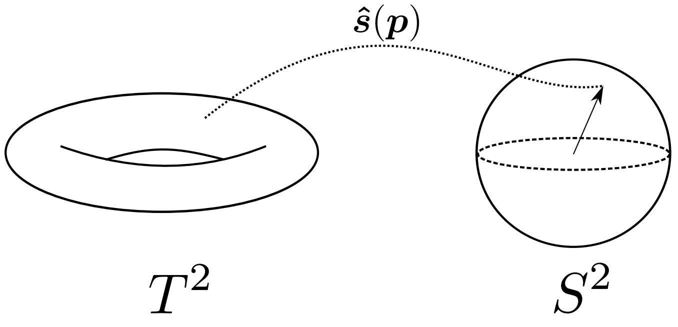

Fig. 4.1: The winding number describes the number of times the map $\boldsymbol{n}(\boldsymbol{k}) : T^2 \rightarrow S^2$ wraps around the unit 2-sphere.

4.4 Observability of the winding number

Equation 4.7 is a key result in this thesis, it establishes the equivalence between knowing the Chern number of the system to knowing a vector field (there denoted by $\boldsymbol{S}$) over the Brillouin Zone. However, these pseudospin models also have an important characteristic: the field values can be computed by measurement of Hermitian operators. In particular, we can express our 2x2 Hamiltonian in a basis of Bogoljubov operators:

$$\hat{H} = \sum_k \hat{\Psi}_k^\dagger H(\boldsymbol{k})\hat{\Psi}_k, \quad \hat{\Psi}_k = \left(\hat{a}_1\,\hat{a}_2\right)^T. \tag{4.8}$$

We can now define the spin field operators in terms of the Pauli matrices:

$$\hat{\boldsymbol{S}}(\boldsymbol{k}) = \frac{1}{2}\hat{\Psi}_k^\dagger\boldsymbol{\sigma}\hat{\Psi}_k, \tag{4.9}$$

which are Hermitian, since Pauli matrices are Hermitian themselves.

We can now go back to our ground state in Eq.4.2 to obtain the main result of this section, which links the spin field in the Brillouin Zone to the expectation value of Hermitian operators in our state:

$$\boldsymbol{S} = \left\langle \hat{\boldsymbol{S}} \right\rangle . \tag{4.10}$$

Though the notation might induce to thinking this relation is absolutely trivial, it shows an important fact: the measurement of a set (in this case, just three per k-point) of observables on our state is sufficient to determine the Chern number of the state. In particular, if our state is the ground state of some Hamiltonian, the observables completely determine the topological nature of our system. This fact will be used repeatedly along the following chapters.

4.5 The Berry Phase

It is straightforward to connect the previous results to the more usual Berry phase, which makes it clear that we are not just dealing with the properties of a model, but also of a *state* (in this case, the ground state of the aforementioned Hamiltonian). That connection is possible because in our particular case of a $\mathcal{M}_2(\mathbb{C})$ model manifold, the ground state actually fully determines the Hamiltonian (as always, up to an identity term). We will show here that the Chern number can be written as the Berry phase that the ground state accrues around the boundary of the Brillouin zone.

In order to prove this, we take the projector representation (4.1) and substitute in the definition $P_{\boldsymbol{k}} = |\psi(\boldsymbol{k})\rangle \langle\psi(\boldsymbol{k})|$:

$$\begin{aligned} \nu \;=\; & -\frac{i}{2\pi}\int_{BZ} \mathrm{d}k_x \mathrm{d}k_y \, \langle\psi(\boldsymbol{k})| \left[(\partial_{k_x} |\psi(\boldsymbol{k})\rangle \langle\psi(\boldsymbol{k})|)(\partial_{k_y} |\psi(\boldsymbol{k})\rangle \langle\psi(\boldsymbol{k})|) - \right. \\ & \left. (\partial_{k_y} |\psi(\boldsymbol{k})\rangle \langle\psi(\boldsymbol{k})|)(\partial_{k_x} |\psi(\boldsymbol{k})\rangle \langle\psi(\boldsymbol{k})|) \right] |\psi(\boldsymbol{k})\rangle . \end{aligned}$$

The ground state is normalised so we have $\partial_\mu \langle\psi(\boldsymbol{k})|\psi(\boldsymbol{k})\rangle = 0$, where $\mu = k_x, k_y$, such that

$$\langle\partial_\mu\psi(\boldsymbol{k})|\psi(\boldsymbol{k})\rangle = -\langle\psi(\boldsymbol{k})|\partial_\mu\psi(\boldsymbol{k})\rangle . \tag{4.11}$$

Expanding (4.11) we obtain

$$\nu = -\frac{i}{2\pi}\int_{BZ} \mathrm{d}k_x \mathrm{d}k_y \left(\left\langle \partial_{k_x}\psi(\boldsymbol{k}) | \partial_{k_y}\psi(\boldsymbol{k}) \right\rangle - \left\langle \partial_{k_y}\psi(\boldsymbol{k}) | \partial_{k_x}\psi(\boldsymbol{k}) \right\rangle \right) . \tag{4.12}$$

We now recognise that the integrand is the Berry curvature, $F_{k_x k_y}$,

$$F_{k_x k_y} = \partial_{k_x} A_{k_y} - \partial_{k_y} A_{k_x} = \left\langle \partial_{k_x}\psi(\boldsymbol{k}) | \partial_{k_y}\psi(\boldsymbol{k}) \right\rangle - \left\langle \partial_{k_y}\psi(\boldsymbol{k}) | \partial_{k_x}\psi(\boldsymbol{k}) \right\rangle , \tag{4.13}$$

where $\boldsymbol{A} = \langle\psi(\boldsymbol{k})|\partial|\psi(\boldsymbol{k})\rangle$ is the Berry connection. Using Stokes' theorem, the Chern number can be written

$$\nu = -\frac{i}{2\pi}\int_{BZ} \mathrm{d}k_x \mathrm{d}k_y \; F_{k_x k_y} = -\frac{i}{2\pi}\oint_{\partial BZ} d\boldsymbol{k} \cdot \boldsymbol{A}, \tag{4.14}$$

where ∂BZ is the boundary of the Brillouin zone. Hence, the Chern number can be written in terms of the Berry phase accumulated by the ground state around the boundary of the Brillouin zone.

4.6 Berry Phase to Winding Number

To complete the picture outlined in Fig. 4.2 we now derive the winding number directly from the Berry phase. We start by writing the Chern number as the integral of the Berry curvature

$$\nu = -\frac{i}{2\pi}\int_{BZ} \mathrm{d}k_x \mathrm{d}k_y \left(\left\langle \partial_{k_x}\psi(\boldsymbol{k}) | \partial_{k_y}\psi(\boldsymbol{k})\right\rangle - \left\langle \partial_{k_y}\psi(\boldsymbol{k}) | \partial_{k_x}\psi(\boldsymbol{k})\right\rangle\right) \tag{4.15}$$

Assuming the Bloch Hamiltonian is 2-dimensional we can write the projector as in Eq. 4.2. We substitute the projector into (4.15)

$$\nu = -\frac{i}{2\pi}\int_{BZ} \mathrm{d}k_x \mathrm{d}k_y \left(\partial_{k_x}\left(\langle\psi(\boldsymbol{k})| P_{\boldsymbol{k}}\right)\partial_{k_y}\left(P_{\boldsymbol{k}}|\psi(\boldsymbol{k})\rangle\right) - \partial_{k_y}\left(\langle\psi(\boldsymbol{k})| P_{\boldsymbol{k}}\right)\partial_{k_x}\left(P_{\boldsymbol{k}}|\psi(\boldsymbol{k})\rangle\right)\right). \tag{4.16}$$

We can now define the vector field $\boldsymbol{S}(\boldsymbol{k}) = \left\langle \hat{\boldsymbol{S}}(\boldsymbol{k})\right\rangle$, and using the fact that $P^2 = P$, $\{\partial_\mu \boldsymbol{n}(\boldsymbol{k})\cdot\boldsymbol{\sigma}, \boldsymbol{n}(\boldsymbol{k})\cdot\boldsymbol{\sigma}\} = 0$ and the properties of Pauli matrices we find that

$$\begin{aligned}\nu &= \frac{1}{4\pi}\int_{BZ} \mathrm{d}k_x \mathrm{d}k_y \ \left\langle \psi(\boldsymbol{k}) | \boldsymbol{\sigma}\cdot\left(\partial_{k_x}\boldsymbol{n}(\boldsymbol{k}) \times \partial_{k_y}\boldsymbol{n}(\boldsymbol{k})\right) | \psi(\boldsymbol{k})\right\rangle \\ &= \frac{1}{4\pi}\int_{BZ} d^2p \ \boldsymbol{n}(\boldsymbol{k})\cdot\left(\partial_{k_x}\boldsymbol{n}(\boldsymbol{k}) \times \partial_{k_y}\boldsymbol{n}(\boldsymbol{k})\right),\end{aligned} \tag{4.17}$$

which shows the equiavlence between the winding number and the Berry phase of a state around the Brillouin Zone.

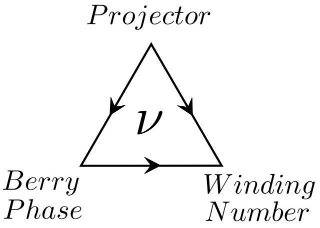

Fig. 4.2: A schematic picture of the different representations of the Chern number, ν. The arrows indicate the direction of the proofs given in this chapter.

Part II

BODY

5. WINDING NUMBERS AS TOPOLOGICAL INVARIANTS IN ENTANGLED BIPARTITIONS

5.1 Summary

We have seen in the introduction that there is an equivalence between Chern number, Berry phase and winding number in a particular family of models. We have hinted, and will explore much more deeply along this thesis, that these alternative formulations are of experimental relevance. However, there is also a scent of a theoretical research possibility: why is it that this particular set of models is selected, and just how much is this equivalence worth when we face a more complicated system?

This chapter provides the first stepping stone for the understanding of that complicated question. Its main result is as follows: The winding numbers of two coupled pseudospin degrees of freedom add up to the Chern number of the system - as long as they are not maximally entangled. This result is powerful in itself for two reasons: it provides some connection between entanglement and topology (or measures of topology) and, if we believe the connection between topology and pseudospin windings is truly helpful experimentally, it opens the way to measuring more complex (composite) systems. Indeed, we include a famous example of this usefulness at the end of the chapter, and more involved examples can be found in Chapter 8.

However, we would like to shed a light on an alternate interpretation of the main result of the chapter, which we phrase as follows: *The winding number of a pseudospin degree of freedom is a topological order parameter itself, whenever it can be defined.* While it is less precise mathematically -particularly the definability and its consequences-, it might be the door to a more thourough understanding of this field. A use of this intuition for trying to observe the topological phase transitions of a more complicated system will be reported in Chapter 9.

The structure of the chapter is outlined in the following. First, in Sec. 5.2 shows analytically that the Chern number can be decomposed as a sum of component specific winding numbers, which are themselves physically observable. Then, in Sec. 5.3 we show that the measurements required for constructing the component winding numbers also enables one to probe the entanglement spectrum with respect to component partitions. Finally, Sec. 5.4 will illustrate the method by applying it on Kane and Mele's model of a $\mathbb{Z}_2$ quantum spin Hall insulator, and show that (spin) Chern numbers are accurately reproduced.

The implementation of the method presented hereafter is particularly suited to experiments with cold atoms in optical lattices where time-of-flight images can give direct access to the relevant observables; as it will be shown in subsequent chapter of this thesis. Other experimental setups that measure spin textures in real condensed matter systems (e.g. spin-resolved ARPES) may also benefit from the kind of analysis provided in this chapter.

5.2 Decomposition of the Chern number into subsystem winding numbers

In this section we give an analytic argument for decomposing the Chern number into a sum of winding numbers associated with the different components. A detailed derivation is first presented for particle number conserving topological insulators. The argument is then shown to apply equally to particle parity conserving topological superconductors. It is assumed that the reader is familiar with the methods outlined in the introduction of this thesis (see chapter 4).

A brief word about the structure of the proof

Due to the unavoidable cumbersome notation and the required level of detail, the proof is not that easy to follow; here we provide some guidance for the more casual reader.

The proof assumes that we are studying a two-component fermionic system. It requires that the 4-dimensional wavefunction can be decomposed into a two-pseudospins structure; the choice of bipartitions typically arises from some symmetry of the problem. We can the imagine that the state at each point of the Brillouin Zone can be rotated to a canonical state (some sort of "trivial vacuum") through the application of a disentagling operation between bipartitions, followed by a unitary for each pseudospin subspace. In contrast with the proof given in the previous chapter, there is no guarantee that each pseudospin subspace is "half-filled" (i.e. a pseudospin proper); in fact, it will be generally not the case. However, we show that only "half-filled" pseudospin subspaces (here called the odd-odd subspace) contribute to the topological invariants, so we can neglect the rest. It is then shown that the Berry phase of the state can be decomposed into the sum of Berry phases of the partitions, with a coefficient that vanishes if the partitions are maximally entangled (and thus no information can be extracted from the partial invariants). The structure of the proof is similar for the two symmetry classes analyzed in this chapter, but they have been differentiated in an effort to simplify the notation in each case.

5.2.1 Decomposition for topological insulators

Let us consider a system with four distinct types of fermion, whose annihilation operators we denote by a_1, a_2, b_1 and b_2, where the *a priori* bipartition between a and b is physically motivated (such as different spin orientations, atomic internal levels or different sectors of some discrete symmetry). Assuming translational invariance with respect to these operators the Hamiltonian can always be given in momentum space as

$$H = \int_{\boldsymbol{p}\in BZ} d^2p\, \Psi^\dagger_{\boldsymbol{p}} h(\boldsymbol{p}) \Psi_{\boldsymbol{p}} \qquad \text{with} \qquad \Psi_{\boldsymbol{p}} = \begin{pmatrix} a_{1,\boldsymbol{p}} \\ a_{2,\boldsymbol{p}} \\ b_{1,\boldsymbol{p}} \\ b_{2,\boldsymbol{p}} \end{pmatrix}. \tag{5.1}$$

A general state in the Hilbert space of the system can be written as

$$|\Psi\rangle = \prod_{\boldsymbol{p}} \left(\sum_{n^a_{1,\boldsymbol{p}},n^a_{2,\boldsymbol{p}},n^b_{1,\boldsymbol{p}},n^b_{2,\boldsymbol{p}}=0,1} \alpha_{n^a_{1,\boldsymbol{p}},n^a_{2,\boldsymbol{p}},n^b_{1,\boldsymbol{p}},n^b_{2,\boldsymbol{p}}} \left|n^a_{1,\boldsymbol{p}}, n^a_{2,\boldsymbol{p}}, n^b_{1,\boldsymbol{p}}, n^b_{2,\boldsymbol{p}}\right\rangle \right) \equiv \prod_{\boldsymbol{p}} |\psi_{\boldsymbol{p}}\rangle\,, \tag{5.2}$$

where we have expressed it in the occupation basis

$$\left|n^a_{1,\boldsymbol{p}}, n^a_{2,\boldsymbol{p}}, n^b_{1,\boldsymbol{p}}, n^b_{2,\boldsymbol{p}}\right\rangle = (a^\dagger_{1,\boldsymbol{p}})^{n^a_{1,\boldsymbol{p}}} (a^\dagger_{2,\boldsymbol{p}})^{n^a_{2,\boldsymbol{p}}} (b^\dagger_{1,\boldsymbol{p}})^{n^b_{1,\boldsymbol{p}}} (b^\dagger_{2,\boldsymbol{p}})^{n^b_{2,\boldsymbol{p}}} |0000\rangle\,. \tag{5.3}$$

Here $n^{a,b}_{i,\boldsymbol{p}} = 0,1$ are the fermionic occupation numbers and $|0000\rangle$ corresponds to the vacuum state of all fermionic modes. Eigenstates of Hamiltonian 5.1 will be of this form for some set of coefficients $\alpha_{n^a_{1,\boldsymbol{p}},n^a_{2,\boldsymbol{p}},n^b_{1,\boldsymbol{p}}n^b_{2,\boldsymbol{p}}}$ that satisfy $\sum_{n^a_{1,\boldsymbol{p}},n^a_{2,\boldsymbol{p}},n^b_{1,\boldsymbol{p}}n^b_{2,\boldsymbol{p}}=0,1} |\alpha_{n^a_{1,\boldsymbol{p}},n^a_{2,\boldsymbol{p}},n^b_{1,\boldsymbol{p}}n}$
1.

Let us now assume that the system conserves particle number, i.e. $[H,N]=0$, where $N = \sum_{\boldsymbol{p},\alpha=1,2}(a^\dagger_{\alpha,\boldsymbol{p}}a_{\alpha,\boldsymbol{p}} + b^\dagger_{\alpha,\boldsymbol{p}}b_{\alpha,\boldsymbol{p}})$. At half filling the ground state $|\psi_{\boldsymbol{p}}\rangle$ satisfies the condition $\sum_{\alpha=1,2}(n^a_{\alpha,\boldsymbol{p}} + n^b_{\alpha,\boldsymbol{p}}) = 2$. This means that a complete local basis for each momentum component of the ground state is given by

$$\{|1100\rangle\,, |1010\rangle\,, |1001\rangle\,, |0110\rangle\,, |0101\rangle\,, |0011\rangle\}\,. \tag{5.4}$$

We can divide the state into two orthogonal subspaces

$$\begin{aligned} |\psi_{\boldsymbol{p}}\rangle &= A\left|\psi(n^a_{1,\boldsymbol{p}} + n^a_{2,\boldsymbol{p}} = \text{even}; n^b_{1,\boldsymbol{p}} + n^b_{2,\boldsymbol{p}} = \text{even})\right\rangle + B\left|\psi(n^a_{1,\boldsymbol{p}} + n^a_{2,\boldsymbol{p}} = \text{odd}; n^b_{1,\boldsymbol{p}} + n^b_{2,\boldsymbol{p}} = \text{o} \\ &\equiv A\,|\psi(e;e)\rangle + B\,|\psi(o;o)\rangle\,, \end{aligned}$$

where the populations $n^a_{1,\boldsymbol{p}} + n^a_{2,\boldsymbol{p}}$ and $n^b_{1,\boldsymbol{p}} + n^b_{2,\boldsymbol{p}}$ are either both even or both odd for some A and B, with $|A|^2 + |B|^2 = 1$. This partitioning of the state in this particular way facilitates our derivation.

We now perform a Schmidt decomposition on each part of the state, the even and the odd. We can write

$$\begin{aligned} |\psi(e;e)\rangle &= \cos\theta_e\,|a_e\rangle\,|b_e\rangle + \sin\theta_e\,|\tilde{a}_e\rangle \left|\tilde{b}_e\right\rangle, \\ |\psi(o;o)\rangle &= \cos\theta_o\,|a_o\rangle\,|b_o\rangle + \sin\theta_o\,|\tilde{a}_o\rangle \left|\tilde{b}_o\right\rangle, \end{aligned} \tag{5.6}$$

where $\theta_e, \theta_o \in [0, \pi/2)$ such that all the Schmidt coefficients are non-negative. It is understood that the $\left|a_{e/o}\right\rangle \left|b_{e/o}\right\rangle$ states written in the population basis have the fermionic operators ordered as in 5.3. The vectors $\left|\tilde{a}_{e/o}\right\rangle\left|\tilde{b}_{e/o}\right\rangle$ obey the orthogonality conditions $\left\langle a_{e/o}|\tilde{a}_{e/o}\right\rangle=0$ and $\left\langle b_{e/o}|\tilde{b}_{e/o}\right\rangle=0$. More explicitly we have

$$\begin{aligned} |a_o\rangle &= \left(\alpha_{01}a^\dagger_{2,\boldsymbol{p}}+\alpha_{10}a^\dagger_{1,\boldsymbol{p}}\right)|00\rangle\,, & |\tilde{a}_o\rangle &= \left(\alpha^*_{10}a^\dagger_{2,\boldsymbol{p}}-\alpha^*_{01}a^\dagger_{1,\boldsymbol{p}}\right)|00\rangle\,, \\ |b_o\rangle &= \left(\beta_{01}b^\dagger_{2,\boldsymbol{p}}+\beta_{10}b^\dagger_{1,\boldsymbol{p}}\right)|00\rangle\,, & \left|\tilde{b}_o\right\rangle &= \left(\beta^*_{10}b^\dagger_{2,\boldsymbol{p}}-\beta^*_{01}b^\dagger_{1,\boldsymbol{p}}\right)|00\rangle \end{aligned} \tag{5.7}$$

and

$$\begin{aligned} |a_e\rangle &= e^{i\phi_a}|00\rangle\,, & |\tilde{a}_e\rangle &= e^{i\tilde{\phi}_a}a^\dagger_{1,\boldsymbol{p}}a^\dagger_{2,\boldsymbol{p}}|00\rangle\,, \\ |b_e\rangle &= e^{i\phi_b}b^\dagger_{1,\boldsymbol{p}}b^\dagger_{2,\boldsymbol{p}}|00\rangle\,, & \left|\tilde{b}_e\right\rangle &= e^{i\tilde{\phi}_b}|00\rangle\,, \end{aligned} \tag{5.8}$$

where $|\alpha_{01}|^2+|\alpha_{10}|^2=|\beta_{01}|^2+|\beta_{10}|^2=1$. The phases $\phi_{a/b}$ and $\tilde{\phi}_{a/b}$ are in general non-zero. However, after multiplying $|\psi_{\boldsymbol{p}}\rangle$ by a global phase of $e^{-i(\phi_a+\phi_b)}$, we can transfer them to the odd-odd subspace through a $U(1)$ gauge transformation $a^\dagger_{1,\boldsymbol{p}}\to e^{-i(\tilde{\phi}_a+\tilde{\phi}_b-\phi_a-\phi_b)}a^\dagger_{1,\boldsymbol{p}}$. Then the only momentum dependence in the Schmidt decomposed even-even subspace is in the real and positive Schmidt coefficients, $\cos\theta_e$ and $\sin\theta_e$.

We now show that we can write the Chern number of the system as a sum of the Berry phases accrued by each subsystem. To this end, we evaluate the Chern number of the ground state of the system, 5.5, as the Berry phase (see chapter 4). Without loss of generality we can take A and B to be real and non-negative. This is achieved by absorbing possible complex phases into the states $\left|a_{e/o}\right\rangle\left|b_{e/o}\right\rangle$ and $\left|\tilde{a}_{e/o}\right\rangle\left|\tilde{b}_{e/o}\right\rangle$. Employing relation 5.5 we can write the Chern number as

$$\nu=-\frac{i}{2\pi}\oint_{\partial BZ}A^2\left\langle\psi(e;e)|\partial|\psi(e;e)\right\rangle\cdot d\boldsymbol{p}-\frac{i}{2\pi}\oint_{\partial BZ}B^2\left\langle\psi(o;o)|\partial|\psi(o;o)\right\rangle\cdot d\boldsymbol{p}, \tag{5.9}$$

where terms of the form $A\partial A$ do not contribute as, due to the reality condition on A and B, $A\partial A+B\partial B=\partial(A^2+B^2)/2=0$. Direct evaluation of the integrand in the even-even case finds it to be zero due to $\cos\theta_e\partial\cos\theta_e+\sin\theta_e\partial\sin\theta_e=\partial(\cos^2\theta_e+\sin^2\theta_e)/2=0$. Thus the first term on the right hand side of 5.9 does not contribute to the Berry phase. Noting that $\langle i_o|\partial|i_o\rangle=-\left\langle\tilde{i}_o|\partial|\tilde{i}_o\right\rangle$ in (5.7) and using the positivity and normalisation of the Schmidt coefficients, a direct evaluation gives

$$\nu=-\frac{i}{2\pi}\sum_{i=a,b}\oint_{\partial BZ}S\left\langle i_o|\partial|i_o\right\rangle\cdot d\boldsymbol{p},\qquad S=|B|^2T, \tag{5.10}$$

where $T=\cos^2\theta_o-\sin^2\theta_o$ is a measure of entanglement between the subsystems.

Thus we have succeeded in decomposing the Chern number into a sum of exclusive contributions from the a or b subsystems. Due to appearance of the function S, these contributions are not Berry phases which one could equivalently evaluate as winding numbers of vectors $\boldsymbol{n}_a(\boldsymbol{p})$ and $\boldsymbol{n}_b(\boldsymbol{p})$. However, by direct evaluation of such winding numbers, which we present below, we find that the Chern number will be additive in them. This $S \to 1$ limit corresponds to there being minimal entanglement between the subsystems, which we take as a criterion of reliability for our method. Indeed, we find in Section 5.4 that degrees of freedom that are weakly coupled by the Hamiltonian provide in general more reliable detection of the Chern number. Before doing so, we turn to defining the physical observables to construct the subsystem winding numbers.

5.2.2 Subsystem winding numbers as physical observables

In direct analogy with the single component case presented in the introduction, we define the observables for the a and b subsystems as

$$\begin{aligned}
\hat{S}_a^x &= a_{1,\boldsymbol{p}}^\dagger a_{2,\boldsymbol{p}} + a_{2,\boldsymbol{p}}^\dagger a_{1,\boldsymbol{p}}, && (5.11)\\
\hat{S}_a^y &= -i a_{1,\boldsymbol{p}}^\dagger a_{2,\boldsymbol{p}} + i a_{2,\boldsymbol{p}}^\dagger a_{1,\boldsymbol{p}}, && (5.12)\\
\hat{S}_a^z &= a_{1,\boldsymbol{p}}^\dagger a_{1,\boldsymbol{p}} - a_{2,\boldsymbol{p}}^\dagger a_{2,\boldsymbol{p}}; && (5.13)
\end{aligned}$$

whereas the $\hat{S}_b$ operators are obtained by replacing a with b in the previous relations.

Since these operators conserve the number of particles there are no cross-terms between the even and odd subspaces of (5.5), and thus the expectation values of these operators $\hat{S}_{i,\boldsymbol{p}} = \left(\hat{S}_i^x, \hat{S}_i^y, \hat{S}_i^z\right)$ read

$$\left\langle \psi_{\boldsymbol{p}} | \hat{S}_{i,p} | \psi_{\boldsymbol{p}} \right\rangle = |A|^2 \left\langle \psi(e;e) | \hat{S}_{i,p} | \psi(e;e) \right\rangle + |B|^2 \left\langle \psi(o;o) | \hat{S}_{i,p} | \psi(o;o) \right\rangle . \quad (5.14)$$

By direct evaluation we find that the contribution from the even subspace vanishes. On the other hand, the odd subspace component gives

$$\left\langle \psi(o;o) | \hat{S}_{i,\boldsymbol{p}} | \psi(o;o) \right\rangle = \cos^2\theta_o \left\langle i_o | \hat{S}_{i,\boldsymbol{p}} | i_o \right\rangle + \sin^2\theta_o \left\langle \tilde{i}_o | \hat{S}_{i,\boldsymbol{p}} | \tilde{i}_o \right\rangle = T \left\langle i_o | \hat{S}_{i,\boldsymbol{p}} | i_o \right\rangle , \quad (5.15)$$

where we have used the tracelessness of the $\hat{S}_{i,\boldsymbol{p}}$ operators that implies $\left\langle \tilde{i}_o | \hat{S}_{i,\boldsymbol{p}} | \tilde{i}_o \right\rangle = -\left\langle i_o | \hat{S}_{i,\boldsymbol{p}} | i_o \right\rangle$. Altogether we then obtain

$$\begin{aligned}
\left\langle \psi_{\boldsymbol{p}} | \hat{S}_{a,\boldsymbol{p}} | \psi_{\boldsymbol{p}} \right\rangle &= S \left\langle \psi_a(\boldsymbol{p}) | \boldsymbol{\sigma} | \psi_a(\boldsymbol{p}) \right\rangle , && (5.16)\\
\left\langle \psi_{\boldsymbol{p}} | \hat{S}_{b,\boldsymbol{p}} | \psi_{\boldsymbol{p}} \right\rangle &= S \left\langle \psi_b(\boldsymbol{p}) | \boldsymbol{\sigma} | \psi_b(\boldsymbol{p}) \right\rangle
\end{aligned}$$

where $|\psi_a(\boldsymbol{p})\rangle = \begin{pmatrix}\alpha_{01}, & \alpha_{10}\end{pmatrix}^T$ and $|\psi_b(\boldsymbol{p})\rangle = \begin{pmatrix}\beta_{01}, & \beta_{10}\end{pmatrix}^T$. In other words, we obtain two vectors $\boldsymbol{n}_a(\boldsymbol{p})$ and $\boldsymbol{n}_b(\boldsymbol{p})$ whose normalized components are given by

$$\boldsymbol{n}_i(\boldsymbol{p}) = \frac{S_i(\boldsymbol{p})}{|S_i(\boldsymbol{p})|} = \left\langle \psi_i(\boldsymbol{p}) | \boldsymbol{\sigma} | \psi_i(\boldsymbol{p}) \right\rangle , \qquad |S_i(\boldsymbol{p})| = |B|^2 |T|. \quad (5.17)$$

The fact that the norm of these vectors is equal to $|S|$ implies that the degree of entanglement between the subsystems can be probed by using the operators 5.11.

Exactly like the Berry phase and the winding number were equivalent representations of the Chern number for two component systems (see Chapter 4) , we can define a subsystem Chern number ν_i for the state $|i_o\rangle$ and represent it equivalently either as the subsystem Berry phase

$$\nu_i = \frac{i}{2\pi} \oint_{\partial BZ} \langle i_o|\partial|i_o\rangle \cdot d\boldsymbol{p}, \tag{5.18}$$

or as the subsystem winding numbers

$$\nu_i = \frac{1}{4\pi} \int_{BZ} d^2p \; \boldsymbol{n}_i(\boldsymbol{p}) \cdot \left(\partial_{p_x}\boldsymbol{n}_i(\boldsymbol{p}) \times \partial_{p_y}\boldsymbol{n}_i(\boldsymbol{p})\right). \tag{5.19}$$

Formally this comes about by viewing $|\psi_i(\boldsymbol{p})\rangle$ as the ground state of a fictitious Hamiltonian $H_i = \boldsymbol{n}_i(\boldsymbol{p}) \cdot \boldsymbol{\sigma}$ with eigenvalues $E = \pm 1$. As we have shown above, the components of the vectors $\boldsymbol{n}_i(\boldsymbol{p})$ can be obtained from the observables 5.11 and hence the subsystem Chern number is an observable.

Under the assumption of small subsystem entanglement, we assume that (5.10) is equivalent to one with $S \to 1$. In this limit the Chern number for the whole system becomes additive in the subsystem winding numbers (5.19) that in turn are physical observables. In Section 5.4 we show using two distinct examples that this assumption is justified. Before doing so, we will first show that with small modifications the same method applies directly also to topological superconductors that conserve only the particle parity.

5.2.3 Decomposition for topological superconductors

The generalisation to topological superconductors is straightforward. We take the Hamiltonian to be of the same form as (5.1) with the basis given now by $\Psi^\dagger_{\boldsymbol{p}} = \left(a^\dagger_{\boldsymbol{p}}, a_{-\boldsymbol{p}}, b^\dagger_{\boldsymbol{p}}, b_{-\boldsymbol{p}}\right)$. The general state can be written as (5.2) with the Fock space ordered as

$$\left|n^a_{\boldsymbol{p}}, n^a_{-\boldsymbol{p}}, n^b_{\boldsymbol{p}}, n^b_{-\boldsymbol{p}}\right\rangle = (a^\dagger_{\boldsymbol{p}})^{n^a_{\boldsymbol{p}}}(a^\dagger_{-\boldsymbol{p}})^{n^a_{-\boldsymbol{p}}}(b^\dagger_{\boldsymbol{p}})^{n^b_{\boldsymbol{p}}}(b^\dagger_{-\boldsymbol{p}})^{n^b_{-\boldsymbol{p}}}\left|0000\right\rangle. \tag{5.20}$$

A superconducting system conserves only the total parity, i.e. $[H, P] = 0$ with $P = \exp\left(i\pi \sum_{\boldsymbol{p}} \left(a^\dagger_{\boldsymbol{p}} a_{\boldsymbol{p}} + b^\dagger_{\boldsymbol{p}} b_{\boldsymbol{p}}\right)\right) = P_a P_b$, while component parities P_a and P_b are not independently conserved. Without loss of generality we assume that the ground state resides in the even total parity sector. This means parities in the subsystems a and b are correlated such that $P_a = P_b$, which in turn means that the ground state complies with the condition of zero overall momentum. In this parity sector the ground state is thus given in the basis spanned by the states

$$\left\{\left|0000\right\rangle, \left|0011\right\rangle, \left|1100\right\rangle, \left|1111\right\rangle, \left|0110\right\rangle, \left|1001\right\rangle\right\}. \tag{5.21}$$

As with the topological insulators, we split the Hilbert space into even and odd occupation subspaces and write

$$|\psi_{\boldsymbol{p}}\rangle = A\,|\psi(e;e)\rangle + B\,|\psi(o;o)\rangle\,. \tag{5.22}$$

Performing a Schmidt decomposition between the subsystems a and b in this parity sector, we obtain a general expression which has the same form as (5.6), but with the Schmidt bases now being given by

$$\begin{aligned} |a_e\rangle &= \left(\alpha_{00} + \alpha_{11} a^\dagger_{\boldsymbol{p}} a^\dagger_{-\boldsymbol{p}}\right)|00\rangle\,, \quad |\tilde{a}_e\rangle = \left(\alpha^*_{11} - \alpha^*_{00} a^\dagger_{\boldsymbol{p}} a^\dagger_{-\boldsymbol{p}}\right)|00\rangle\,, \\ |b_e\rangle &= \left(\beta_{00} + \beta_{11} b^\dagger_{\boldsymbol{p}} b^\dagger_{-\boldsymbol{p}}\right)|00\rangle\,, \quad \left|\tilde{b}_e\right\rangle = \left(\beta^*_{11} - \beta^*_{00} b^\dagger_{\boldsymbol{p}} b^\dagger_{-\boldsymbol{p}}\right)|00\rangle\,, \end{aligned} \tag{5.23}$$

and

$$\begin{aligned} |a_o\rangle &= e^{i\phi_a} a^\dagger_{-\boldsymbol{p}}|00\rangle\,, \quad |\tilde{a}_o\rangle = e^{i\tilde{\phi}_a} a^\dagger_{\boldsymbol{p}}|00\rangle\,, \\ |b_o\rangle &= e^{i\phi_b} b^\dagger_{\boldsymbol{p}}|00\rangle\,, \quad \left|\tilde{b}_o\right\rangle = e^{i\tilde{\phi}_b} b^\dagger_{-\boldsymbol{p}}|00\rangle\,. \end{aligned} \tag{5.24}$$

As in the case of topological insulators where all coefficients except those in the odd subspace could be made real through $U(1)$ gauge transformations, we can now take only the coefficients in the even subspace to be complex and all other coefficients to be real. The decomposition of the Berry phase proceeds in similar steps to the insulating case. The only difference is that it is now the odd subspace contribution that vanishes in (5.9), with the Chern number being now given by

$$\nu = -\frac{i}{2\pi}\sum_{i=a,b}\oint_{\partial BZ} S\,\langle i_e|\partial|i_e\rangle\cdot d\boldsymbol{p}, \qquad S = |A|^2T. \tag{5.25}$$

The relevant observables $\hat{S}_{i,\boldsymbol{p}} = \left(\hat{S}^x_i, \hat{S}^y_i, \hat{S}^z_i\right)$ to evaluate the subsystem winding numbers are now defined by

$$\hat{S}^x_a = a^\dagger_{\boldsymbol{p}} a^\dagger_{-\boldsymbol{p}} + a_{-\boldsymbol{p}} a_{\boldsymbol{p}}, \tag{5.26}$$

$$\hat{S}^y_a = -i a^\dagger_{\boldsymbol{p}} a^\dagger_{-\boldsymbol{p}} + i a_{-\boldsymbol{p}} a_{\boldsymbol{p}}, \tag{5.27}$$

$$\hat{S}^z_a = a^\dagger_{\boldsymbol{p}} a_{\boldsymbol{p}} - a^\dagger_{-\boldsymbol{p}} a_{-\boldsymbol{p}}; \tag{5.28}$$

whereas the $\hat{S}_b$ operators are obtained by replacing a with b in the previous relations.

Computing their expectation values we find that now only the even subspace contributes. The precise expressions are given by

$$\left\langle \psi(e;e)|\hat{\boldsymbol{S}}_{a,\boldsymbol{p}}|\psi(e;e)\right\rangle = S\,\langle\psi_a(\boldsymbol{p})|\boldsymbol{\sigma}|\psi_a(\boldsymbol{p})\rangle\,, \tag{5.29}$$

$$\left\langle \psi(e;e)|\hat{\boldsymbol{S}}_{b,\boldsymbol{p}}|\psi(e;e)\right\rangle = S\,\langle\psi_a(\boldsymbol{p})|\boldsymbol{\sigma}|\psi_a(\boldsymbol{p})\rangle\,, \tag{5.30}$$

where now $|\psi_a(\boldsymbol{p})\rangle = \begin{pmatrix}\alpha_{00}, & \alpha_{11}\end{pmatrix}^T$ and $|\psi_b(\boldsymbol{p})\rangle = \begin{pmatrix}\beta_{00}, & \beta_{11}\end{pmatrix}^T$. Thus the expectation values can again be used to define two vectors $\boldsymbol{n}_a(\boldsymbol{p})$ and $\boldsymbol{n}_b(\boldsymbol{p})$, that can be used to evaluate the subsystem winding numbers 5.19. Under the same assumption of non-maximal entanglement between the subsystems, the Chern number will be shown to be additive in these winding numbers.

5.3 Detection of subsystem entanglement spectrum

We found above that the observable $|\mathbf{S}_i(\mathbf{p})| \propto |\cos^2\theta_{\mathbf{p}} - \sin^2\theta_{\mathbf{p}}|$ provides a measure of entanglement between the subsystems. For $|\mathbf{S}_i(\mathbf{p})| \to 0$ the subsystems become maximally entangled, while for $\cos\theta_{\mathbf{p}} \to 1$ or $\sin\theta_{\mathbf{p}} \to 1$ the ground state becomes a product state. In fact, one can go further and use these same observables to construct the entanglement spectrum corresponding to component partitioning of the system that preserves translational symmetry [61].

As was first pointed out by Li and Haldane [63], ground states described by reduced density matrices

$$\rho_a = \mathrm{tr}_b \rho \propto e^{-\mathcal{H}_E^a} \tag{5.31}$$

contain additional information if one considers the full spectrum of the entanglement Hamiltonian $\mathcal{H}_E^a$. In the case of free or paired fermion problems, these are known to inherit the structure of the physical Hamiltonians in the sense that both can be formally written in the same basis [74]. Thus, the entanglement Hamiltonians can be readily diagonalized with their eigenvalues ϵ_i constituting the (single particle) entanglement spectrum. We now show that these can be obtained directly from the observables $|\mathbf{S}_i(\mathbf{p})|$ for free fermion problems.

It has been shown by Peschel (Ref. [74]) that the entanglement energies ϵ_i of insulators can be obtained from ground state correlation functions $C_{ij}^a = \langle a_i^\dagger a_j \rangle$. To be precise, the eigenvalues λ_i of this correlation matrix $\hat{C}^a$ are related to them through

$$\lambda_i = (e^{\epsilon_i} + 1)^{-1}. \tag{5.32}$$

For every momentum component of the ground state $\hat{C}^a$ is a 2×2 matrix. It is easy to see that e.g. $S_a^z(\mathbf{p}) = C_{11}^a - C_{22}^a$, and similarly for the x- and y-components. By direct calculation one then obtains the eigenvalues $\lambda_\pm = (N_a \pm |\mathbf{S}_a(\mathbf{p})|)/2$, where we have defined the occupation in the subsystem a as $N_a = \langle a_1^\dagger a_1 + a_2^\dagger a_2 \rangle$. Substituting this into (5.32) yields the entanglement spectrum at each momenta

$$\epsilon_\pm(\mathbf{p}) = \ln\left(\frac{N_b \mp |\mathbf{S}_a(\mathbf{p})|}{N_a \pm |\mathbf{S}_a(\mathbf{p})|}\right), \tag{5.33}$$

where $N_b = 2 - N_a$ as we consider systems at half-filling. Hence, our observables give direct access also to the component entanglement spectrum studied in [61]. The entanglement gap closes if $\epsilon_+ = \epsilon_-$ for some momentum mode $\mathbf{p}$. This is satisfied only when $|\mathbf{S}_a(\mathbf{p})| = 0$, i.e. when the subsystems are maximally entangled and our detection scheme becomes unreliable.

While a similar analytic derivation between the entanglement spectrum and the observables is more involved for paired fermion systems due to (5.32) being replaced by a more complicated relation [74], one can qualitatively understand that a similar relation must also hold for such systems. The $\mathbf{p}$-th component of ρ_a is

$$\begin{aligned}\rho_a(\mathbf{p}) = \;& |A|^2 \quad \left(\cos^2\theta_e \left|a_e\right\rangle \left\langle a_e\right| + \sin^2\theta_e \left|\tilde{a}_e\right\rangle \left\langle \tilde{a}_e\right|\right) & (5.34)\\ + \;& |B|^2 \quad \left(\cos^2\theta_o \left|a_o\right\rangle \left\langle a_o\right| + \sin^2\theta_o \left|\tilde{a}_o\right\rangle \left\langle \tilde{a}_o\right|\right), & (5.35)\end{aligned}$$

with ρ_a being a product of these components over $\mathbf{p}$. The state with greatest weight in ρ_a is the groundstate of the entanglement Hamiltonian, and since this Hamiltonian is of superconducting form, the groundstate must reside in the even parity sector. This means that the largest eigenvalue of ρ_a is

$$\prod_{\mathbf{p}} |A|^2 \max(\cos^2\theta_e, \sin^2\theta_e). \tag{5.36}$$

$|\mathbf{S}_a(\mathbf{p})| \propto |\cos^2\theta_e - \sin^2\theta_e|$ vanishes when $\cos^2\theta_e = \sin^2\theta_e$, and when this happens, the largest eigenvalue of ρ_a becomes degenerate. In other words, as in the case for insulating systems, when the subsystems are maximally entangled, the entanglement gap closes. Indeed, we will numerically show below that the observable $|\mathbf{S}_a(\mathbf{p})|$ and the entanglement gap are in exact agreement also for superconducting systems.

5.4 Case study: The Quantum Spin Hall Insulator

We now turn to demonstrate the validity of the previous analytic arguments for detecting Chern numbers through subsystem winding numbers by apply our scheme to a relevant particular example: the quantum spin Hall insulator [52]. We show that in both cases the phase diagrams are accurately reproduced, with any discrepancies being attributable to high entanglement between the spin degrees of freedom.

Let us define Kane and Mele's model for a the quantum spin-Hall insulator on a honeycomb lattice [52]. The Hamiltonian is given by

$$\begin{aligned}H = & \, t\sum_{\langle \boldsymbol{ij}\rangle} a^\dagger_{\boldsymbol{i}} b_{\boldsymbol{j}} + \lambda_v \sum_{\boldsymbol{i}} \left(a^\dagger_{\boldsymbol{i}} a_{\boldsymbol{i}} - b^\dagger_{\boldsymbol{i}} b_{\boldsymbol{i}}\right)\\ & + i\lambda_{SO} \sum_{\langle\langle \boldsymbol{ij}\rangle\rangle} \xi_{SO} \left(a^\dagger_{\boldsymbol{i}} \sigma_z a_{\boldsymbol{j}} + b^\dagger_{\boldsymbol{i}} \sigma_z b_{\boldsymbol{j}}\right) + i\lambda_R \sum_{\langle \boldsymbol{ij}\rangle} a^\dagger_{\boldsymbol{i}} \left(\boldsymbol{\sigma} \times \hat{\boldsymbol{d}}_{\boldsymbol{i}}\right)_z b_{\boldsymbol{j}}.\end{aligned} \tag{5.37}$$

where the spinors $a^\dagger_{\boldsymbol{i}} = (a^\dagger_{\boldsymbol{i},\uparrow}, a^\dagger_{\boldsymbol{i},\downarrow})$ and $b^\dagger_{\boldsymbol{i}} = (b^\dagger_{\boldsymbol{i},\uparrow}, b^\dagger_{\boldsymbol{i},\downarrow})$ denote the two sublattice degrees of freedom of the honeycomb lattice. The first two terms of magnitudes t and λ_v describe spin-independent nearest-neighbour tunnelling and a sublattice energy imbalance, respectively. The other two terms proportional to λ_R and λ_{SO} are nearest and next-nearest neighbour spin-orbit couplings, respectively. In this notation we have $\xi_{SO} = \mathrm{sign}(\hat{\boldsymbol{d}}_1 \times \hat{\boldsymbol{d}}_2)$, with $\hat{\boldsymbol{d}}_1$ and $\hat{\boldsymbol{d}}_2$ being vectors that connect the next-to-nearest neighbour sites.

By Fourier transforming the Hamiltonian (5.37) it takes the Bloch form (5.1) in the basis $\Psi_{\boldsymbol{p}} = (a_{\uparrow,\boldsymbol{p}}, a_{\downarrow,\boldsymbol{p}}, b_{\uparrow,\boldsymbol{p}}, b_{\downarrow,\boldsymbol{p}})^T$. By diagonalising this Hamiltonian Kane and Mele showed that it supports a trivial insulator and a quantum spin Hall phase, which are distinguished by a $\mathbb{Z}_2$ valued topological invariant [52]. While in a time-reversal symmetric system the Chern number is zero in all phases, the $\mathbb{Z}_2$ invariant was shown to be related to the so called spin Chern numbers that are quantised for each spin component [85]. More precisely, the $\mathbb{Z}_2$ invariant was defined as the difference of the spin Chern numbers, $\nu_S = (\tilde{\nu}_\uparrow - \tilde{\nu}_\downarrow)/2$, that only takes non-zero value in the quantum spin Hall phase. The phase diagram as a function of the microscopic parameters is shown in Fig. 5.1.

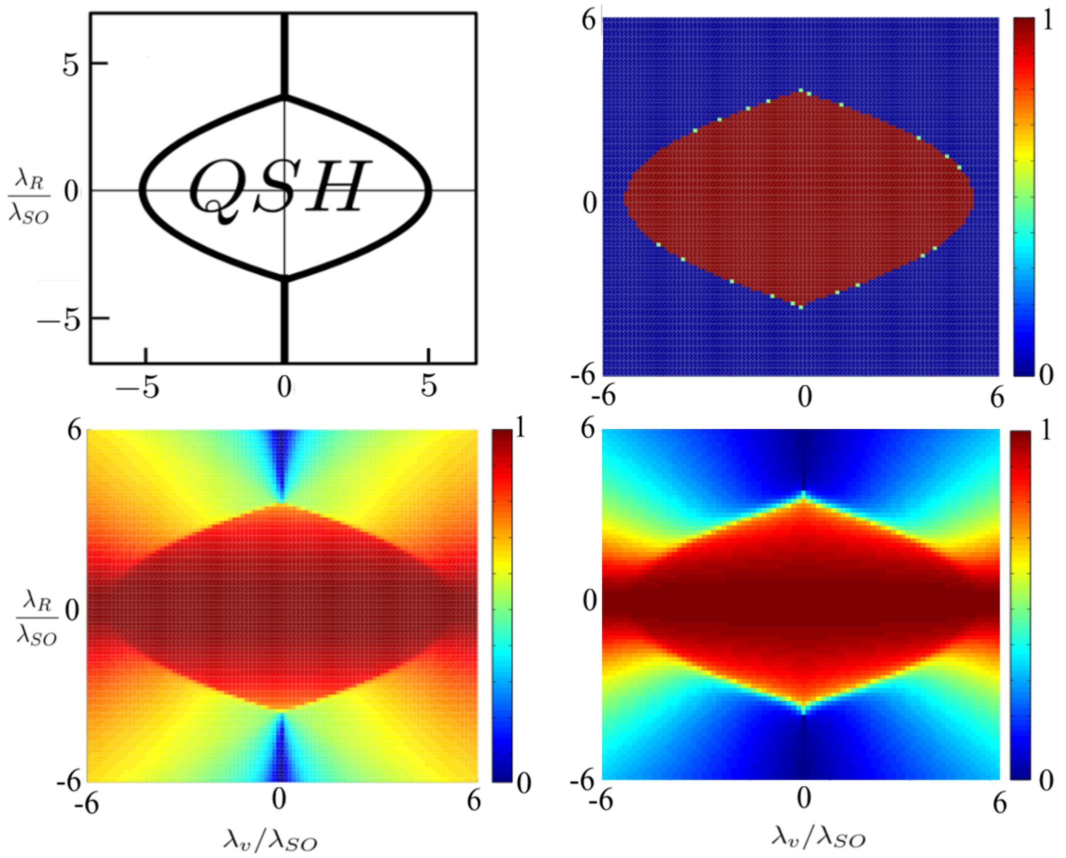

Fig. 5.1: *Top Left*: Theoretical phase diagram in the parameter-space λ_R/λ_{SO}, λ_V/λ_{SO} of Hamiltonian (5.37). The trivial phase corresponds to $\nu_S = 0$, while the QSH phase corresponds to $\nu_S = 1$. *Top Right*: Numerical computation of the phase diagram as the winding spin Chern number $(\tilde{\nu}_\uparrow - \tilde{\nu}_\downarrow)/2$. *Bottom Left*: The minimum of the spin component entanglement measure across the Brillouin zone, $\min_{\boldsymbol{p}} |\boldsymbol{s}_i(\boldsymbol{p})|$. We find the spin components becoming maximally entangled only around the transitions between the two trivial insulators, while between trivial and spin Hall phases we find a discontinuity. *Bottom Right*: The gap of the entanglement spectrum corresponding to the spin up subsystem. This gap is defined to be $\min_{\boldsymbol{p}} \lambda_+ - \max_{\boldsymbol{p}} \lambda_-$ and is seen to close when $\boldsymbol{s}_i(\boldsymbol{p}) = 0$, in agreement with the theoretical arguments presented in section 5.3.

The spin Chern number has a natural counterpart in our constrution if we identify the spin up and spin down components as the two subsystems with respect to which the ground state is Schmidt decomposed. The corresponding operators for evaluating the subsystem winding numbers are

$$\begin{aligned}\hat{S}^x_\uparrow &= a^\dagger_{\uparrow,\boldsymbol{p}} b_{\uparrow,\boldsymbol{p}} + b^\dagger_{\uparrow,\boldsymbol{p}} a_{\uparrow,\boldsymbol{p}},\\ \hat{S}^y_\uparrow &= -i a^\dagger_{\uparrow,\boldsymbol{p}} b_{\uparrow,\boldsymbol{p}} + i b^\dagger_{\uparrow,\boldsymbol{p}} a_{\uparrow,\boldsymbol{p}},\\ \hat{S}^z_\uparrow &= a^\dagger_{\uparrow,\boldsymbol{p}} a_{\uparrow,\boldsymbol{p}} - b^\dagger_{\uparrow,\boldsymbol{p}} b_{\uparrow,\boldsymbol{p}} \end{aligned} \tag{5.38}$$

and similarly for the $\downarrow$-spin component. We construct the vectors $\boldsymbol{n}_\uparrow(\boldsymbol{p})$ and $\boldsymbol{n}_\downarrow(\boldsymbol{p})$ from these observables and by inserting them into 5.19, calculate the corresponding subsystem winding numbers $\nu_\uparrow$ and $\nu_\downarrow$. We find that these observables give then precisely the spin Chern numbers $\tilde{\nu}_\uparrow$ and $\tilde{\nu}_\downarrow$, with Figure 5.1 showing that the phase diagram is precisely reproduced. The figure also shows that the subsystem entanglement measure $|S|$ remains large within the QSH phase, which confirms that the spin components are minimally entangled in this phase. We take this as confirming the reliability of our method for non-maximally entangled states.

5.5 Conclusions

We have presented a method to detect Chern numbers of topological multi-component insulators and superconductors. This method is based on an analytic decomposition of the Chern number as the sum of subsystem winding numbers, which in turn can be expressed in terms of the expectation values of observable quantities. The decomposition of the Chern number in terms of the component winding numbers makes no *a priori* assumptions on the physical nature of the components; however, for an reliable experimental application of our method, one should employ observables associated with components that are not close to being maximally entangled.

We have also provided numerical evidence on how this method can be useful to extract partial topological invariants even in the case where the overall state has a zero Chern number, as it happens with Kane and Mele's model for QSHE. The observed low entanglement between spin components in the QSH insulator can also be viewed as a complementary argument for the robustness of the spin Chern number in the presence of the spin mixing Rashba term [85].

It has been shown analytically that the entanglement between the components was directly related to the gap in the translation symmetry preserving component entanglement spectrum [61], with gap closures corresponding to maximally entangled modes. As the component entanglement is a physical observable in itself, this result provides a rare example of entanglement properties that can be probed through physical measurements.

An crucial open question is the generalisation of this analytic argument for the Chern number decomposition to n component systems. While Schmidt decompositions are hard to generalise for systems with more than two components [2], convoluted bi-partite Schmidt decompositions might be a possible path. However, we will see in chapter 9 another road: to take the winding number seriously even in the absence of a complete understanding or characterization of the topological nature of the state. As a final note, another interesting future direction to study what other entanglement (spectrum) properties, in particular those related to other types of system partitions [63, 87, 44], could be accessed through measurements.

6. SIMULATION OF A COMPLETE DIRAC HAMILTONIAN IN AN OPTICAL HONEYCOMB LATTICE

6.1 Summary

This chapter contains a proposal to make full use of optical lattice technology to create, manipulate and measure the properties of particles which obey a (2+1) Dirac Hamiltonian. It will review how the continuum limit of a bidimensional honeycomb lattice model can give rise to Dirac pseudoparticles; and show that the tuning of the microscopic parameters gives rise to the addition of various sorts of particle properties, from the appearence of a map to being subject to a non-Abelian potential.

We propose to implement these phenomena through the creation of a spin-dependent optical lattice loaded with an alkaline atomic species with two degenerate hyperfine internal states, and we identify the tunable microscopic parameters in this setup. In line with the rest of the thesis, a special emphasis is set on how the properties of the system can be measured; we show that the band structure can be probed by several techniques, such as few-particle dynamics ([90]) or spin textures at half-filling. The measurement procedures introduced here will be reutilized in subsequent chapters of this thesis to signal the presence of entanglement and topological order.

The ideas here presented borrow from the discussions on how to implement artificial fields or gap tuning by strains and external fields in condensed matter systems (mainly graphene). We relate the parameters of the continuum description of the Dirac field to the microscopic parameters, and show quantitatively how these can be modified by means of laser intensity patterns. The Wannier functions for the two interpenetrating triangular lattices are calculated, and this analysis opens the door for a experimetal study of the effect of interactions between Dirac particles.

This chapter is organized as follows: First, there is a review of the band structure of a tight-binding honeycomb lattice and how its low-energy excitations at half-filling can be described by a continuous Dirac field. Then a method for calculating the relation between real-space modulations of the lattice parameters and the field description is developed. We then show how all possible terms of a 2+1 abelian Dirac Hamiltonian can be recreated in the lattice, and extend the analysis to include non-abelian (valley mixing) terms. Subsequently, we formulate our optical lattice proposal, and specify how all the tight-binding terms described above can be experimentally implemented. Finally, a set of possible measurement schemes are explained, each with the capability of probing different characteristics of the Dirac field.

6.2 Dirac fields as low-energy excitations in a honeycomb lattice

We have seen in section 3.4 that deep lattices, such as high-intensity optical lattices, admit a description of its dynamics in terms of second-quantization tight-binding models. Here we will review a theoretical framework in which 2D fields arise as

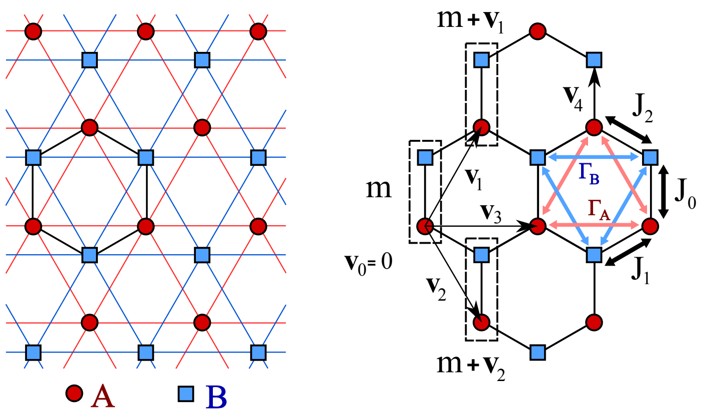

Fig. 6.1: Two triangular sub-lattices displaced one with respect to the other to generate a honeycomb lattice. The vectors $\vec{v}_1$ and $\vec{v}_2$ are the hexagonal lattice generator vectors, whose length is the triangular lattice period, $d = |\vec{v}_{2,3}|$. In addition we define $\vec{v}_0 = 0$ and $\vec{v}_3 = \vec{v}_1 + \vec{v}_2$. The unit cells are shown with dashed rectangles, and are labelled by m. Γ_A and Γ_B are the hopping parameters related with jumps between positions inside sub-lattices A and B while J_i are the hopping parameters related with hexagonal jumps between sublattices, each one related with the corresponding $\vec{v}_i$, $i = 0, 1, 2$.

the continuum approximation to a quadratic tight-binding model on a honeycomb lattice. We will focus on fixing the notation and on the abstract model. More precisely, we are interested in the derivation of honeycomb lattice band structure, whose excitations behave as relativistic Dirac particles.

6.2.1 Tight-binding model for two coupled sub-lattices

Consider a system of fermionic particles in a strong confining periodic potential. We model these particles with fermionic creation and annihilation operators which describe the presence or absence of a fermion in a particular lattice site. The lattice is bipartite, which means that it can be divided into two disjoint sets of sites A and B, where the nearest neighbours of any A-site are all elements of B, and viceversa [cf. figure 6.1a)]. We consider nearest-neighbour hoppings between different sublattices of a bipartite lattice, and also next-to-nearest-neighbour (or intra-lattice) hoppings. For the hexagonal spatial geometry shown in figure 6.1, our model Hamiltonian reads:

$$\begin{aligned} H &= \sum_{m} \left(J_0 a_m^\dagger b_m + J_1 a_m^\dagger b_{m-v_1} + J_2 a_m^\dagger b_{m+v_2} + \text{H.c.} \right) \qquad (6.1) \\ &+ \sum_{v=v_1}^{v_3} \left(\Gamma_A a_m^\dagger a_{m+v} + \Gamma_B b_m^\dagger b_{m+v} + \text{H.c.} \right), \end{aligned}$$

where the J_i are the hopping parameters related with the nearest neighbour hoppings; Γ_A and Γ_B model the tunneling effect inside sublattices A and B respec-

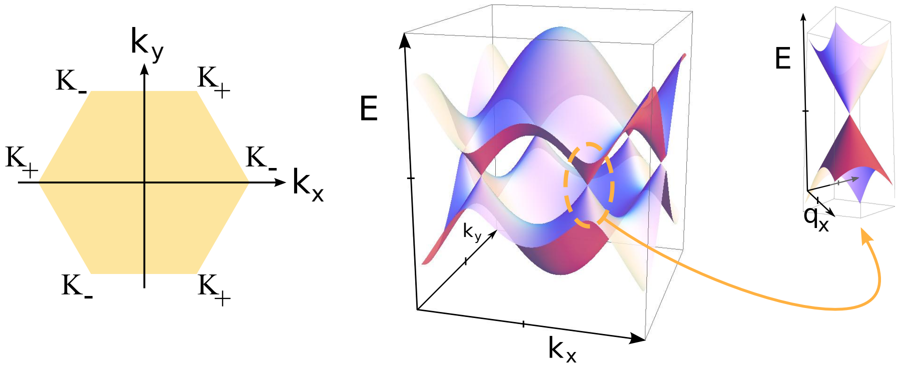

Fig. 6.2: *Left*: First Brillouin Zone (1BZ) for an hexagonal lattice. The $K_\pm$ points written in black are the non-equivalent Dirac Points. *Center*: three-dimensional representation of the energy bands of the honeycomb lattice. The two surfaces represent the positive and the negative energy solutions equation (6.4) meeting together in the Dirac points where $E = 0$. *Right*: zoom around the Dirac points where the energy bands take conical shape and the Hamiltonian of the system can be approximated as a Dirac Hamiltonian, being $E \propto |\vec{q}|$, equation (6.6).

tively; $a_m^\dagger$ and a_m ($b_m^\dagger$ and b_m) are the creation and annihilation operators for an atom in the position m of sublattice A (B), and the v's refer to the $\vec{v}$ vectors represented in figure 6.1b. The first line of equation (6.1) represents the hexagonal hoppings, and the second line represents the two kinds of triangular hoppings. Note also that J_0, J_1, J_2, Γ_A and Γ_B all have units of energy in this notation.

6.2.2 Energy bands and Dirac field

The honeycomb Hamiltonian is recovered from equation (6.1) by making $J_0 = J_1 = J_2 \equiv J$ and $\Gamma_A = \Gamma_B = 0$:

$$H_{hon} = J \sum_m \left\{ a_m^\dagger b_m + a_m^\dagger b_{m-v_1} + a_m^\dagger b_{m+v_2} + H.c. \right\}. \tag{6.2}$$

To calculate the energy bands, we do a Fourier transform over the creation and annihilation operators as

$$a_m^\dagger = \int_\Omega \frac{\mathrm{d}^2 k}{2\pi} e^{i\vec{k}\cdot\vec{r}_m} a_{\vec{k}}^\dagger, \tag{6.3}$$

where $\vec{k}$ is the momentum, $\vec{r}_m$ is the position of the site m, the integration limit Ω makes reference to the first Brillouin Zone (1BZ) and a similar expression is used for b. The diagonalization of the Hamiltonian in momentum space leads to the eigenvalues of the energy that form the energy band structure; namely

$$E_\pm(\vec{k}) = \pm J \sqrt{3 + 4\cos\left(\frac{1}{2}k_x d\right)\cos\left(\frac{\sqrt{3}}{2}k_y d\right) + 2\cos\left(k_x d\right)}, \tag{6.4}$$

which are represented in figure 6.2. There are six points in the 1BZ for which $E = 0$, but only two of them are non-equivalent and we name them $K_{\pm} = (\mp\frac{4\pi}{3}, 0)/d$, where d is the *triangular* lattice spacing [84]. Assuming only small energy perturbations around $E = 0$, the excitations will be confined to the so called Dirac cones. To find the effective theory for these low-energy and long-wavelength excitations one makes an expansion around the Dirac points of $E(\vec{k})$, introducing $\vec{q} = \vec{k} - \vec{K}_{\pm}$ and assuming that for the relevant states it remains "small" (i.e. $|\vec{q}| \times d \ll 1$). Under these conditions, it is possible to work with the Dirac cones as if they extended over all values of $\vec{q}$, with integrals in $\mathrm{d}^2\mathrm{k}$ over the 1BZ being replaced by an integral in $\mathrm{d}^2\mathrm{q}$ over the whole momentum space. By transforming the operators back to position space via inverse Fourier transform

$$\phi_a^{\dagger}(\vec{r}) = \int \frac{1}{2\pi} a^{\dagger}_{\vec{K}+\vec{q}} e^{i(\vec{K}+\vec{q})\cdot\vec{r}} \mathrm{d}^2\mathrm{q}, \tag{6.5}$$

one gets an effective theory for the continuum fields $\{\phi_a(\vec{r}), \phi_b(\vec{r})\}$, satisfying the Dirac-like Hamiltonian (cf. equation 6.15)

$$h_{+}(\vec{q}) \propto \vec{\sigma} \cdot \vec{q}, \quad h_{-}(\vec{q}) = -h_{+}(\vec{q})^{\star}, \tag{6.6}$$

where $\vec{\sigma} = (\sigma_x, \sigma_y)$ are the usual Pauli matrices and the subscript ± stands for the choice of cone ($K_{\pm}$).

6.2.3 Derivation of the Dirac Hamiltonian in position space

While the previous discussion reveals the main ingredients of the relativistic fields which arise from the discrete Hamiltonian, two concerns appear. One is the added difficulty of treating spatially dependent perturbations, since this analytic derivation involves two consecutive Fourier transforms. The other concern is the little attention paid to the fact that there are two intrinsically different cones, which in line with previous literature we call the two "flavours" (or "valleys") of Dirac particles in the lattice. As we will show later, flavour plays a role in the simulation of non-Abelian fields.

In order to extend the derivation of the Dirac dispersion relation to setups in which translational invariance is weakly broken, we rely on a continuum-field approach that bypasses the use of momentum space [46]. Starting with our tight-binding Hamiltonian (6.2), we approximate the Fock operators at each lattice site as the value of a continuous field defined over all space, but which varies so smoothly that it is approximately constant over each unit cell. Moreover, since low-energy excitations are restricted to the vicinity of the $K_{\pm}$ quasimomenta, these fields are the envelope of quasi-plane wavepackets around those points

$$\hat{a}_m \to \sqrt{\mathrm{d}^2 r}\left(\hat{\Psi}_{a+}(\vec{r}_m) e^{-i\vec{K}_{+}\cdot\vec{r}_m} + \hat{\Psi}_{a-}(\vec{r}_m) e^{-i\vec{K}_{-}\cdot\vec{r}_m}\right), \tag{6.7}$$

with an equivalent expression for $\hat{b}_m$. Here $\mathrm{d}^2 r$ is the unit cell area and the exponential containing the Dirac points $\vec{K}_{\pm}$ implements the desired wavepacket ansatz.

Substituting these operators in the tight-binding model produces the following limit Hamiltonian

$$\hat{H} \propto \sum_{\tau,\zeta,i} \int e^{i\vec{r}(\vec{K}_\tau - \vec{K}_\zeta)} \left[\hat{\Psi}^\dagger_{a\tau}(\vec{r})\hat{\Psi}_{b\zeta}(\vec{r}+\vec{v}_i)e^{-i\vec{K}_\tau\cdot\vec{v}_i} + \text{H.c.}\right] \mathrm{d}^2 r, \tag{6.8}$$

where the Greek indices stand for the two possible flavour choices (± cones). Note that the index $i = 0, 1, 2$ runs over the three vectors $\vec{v}_0, -\vec{v}_1, \vec{v}_2$ depicted in figure 6.1 and which connect different unit cells. This is so, because we are free to define the smoothly varying fields Ψ_a and Ψ_b on the middle point of the unit cell.

Since we have enforced the fields to be slowly varying, the presence of the rapidly oscillating exponential $e^{i\vec{r}(\vec{K}_\tau - \vec{K}_\zeta)}$ imposes the condition $\tau = \zeta$ and we end up with two flavour-decoupled integrals. A more quantitative argument would compare the $\tau = \zeta$ term with one that oscillates with $\vec{K}_+ - \vec{K}_-$. Since both are proportional to J, we only need to compare their ratio. Integrating by parts the oscillating term and using periodic or open boundary conditions we may write the rapidly oscillating term correction as

$$\sum_{\tau\neq\zeta} \int e^{i\vec{r}(\vec{K}_\tau - \vec{K}_\zeta)} \left[\hat{\Psi}^\dagger_{a\tau}(\vec{r}) \left(\frac{\vec{K}_\tau - \vec{K}_\zeta}{|\vec{K}_\tau - \vec{K}_\zeta|^2}\cdot\nabla\right)\hat{\Psi}_{b\zeta}(\vec{r}+\vec{v}_i) + \text{H.c.}\right] \mathrm{d}^2 r, \tag{6.9}$$

which becomes small if the fields oscillate slowly, that is $d|\nabla\Psi| \ll |\Psi|$.

At this point one may expand $\hat{\Psi}(\vec{r}+\vec{v}) \simeq [1+\vec{v}\cdot\mathbf{\nabla}]\hat{\Psi}(\vec{r})$ so that the Hamiltonian reads:

$$\hat{H} \propto \sum_{\tau,i} \int \left\{\hat{\Psi}^\dagger_{a\tau}(\vec{r})\,[1+\vec{v}_i\mathbf{\nabla}]\,\hat{\Psi}_{b\tau}(\vec{r})e^{-i\vec{K}_\tau\cdot\vec{v}_i} + \text{H.c.}\right\} \mathrm{d}^2 r. \tag{6.10}$$

Our resulting Hamiltonian is therefore diagonal both in position and in flavour space but couples the internal degrees of freedom *a*-*b* via an off-diagonal operator with only one nontrivial term:

$$C_\tau = 1 + e^{-i\vec{K}_\tau\cdot\vec{v}_2}[1+\vec{v}_2\cdot\mathbf{\nabla}] + e^{i\vec{K}_\tau\cdot\vec{v}_1}[1-\vec{v}_1\cdot\mathbf{\nabla}] \tag{6.11}$$

Since $1 + e^{-i\vec{K}_\tau\cdot\vec{v}_2} + e^{i\vec{K}_\tau\cdot\vec{v}_1}$ vanishes due to the definition of the Dirac cones, the coupling term simplifies to

$$C_\pm = e^{-i\vec{K}_\pm\vec{v}_2}\vec{v}_2\cdot\mathbf{\nabla} - e^{i\vec{K}_\pm\cdot\vec{v}_1}\vec{v}_1\mathbf{\nabla} = \frac{\sqrt{3}d}{2}[\partial_y - \pm i\partial_x]. \tag{6.12}$$

Introducing a momentum operator $\vec{q} = -i\mathbf{\nabla}$, our coupling term becomes $C_\tau \sim \tau q_x + i q_y$ and the Hamiltonian spatial density is therefore:

$$\begin{aligned} h_+(\vec{r}) &= c\begin{pmatrix} 0 & C_+ \\ C^\star_+ & 0 \end{pmatrix} = c\begin{pmatrix} 0 & q_x + iq_y \\ q_x - iq_y & 0 \end{pmatrix} = c\,\vec{q}\cdot\vec{\sigma} \\ h_-(\vec{r}) &= -h^*_+(\vec{r}) \end{aligned} \tag{6.13}$$

which is the expression of the massless Dirac Hamiltonian with Fermi velocity $c = \sqrt{3}Jd/2\hbar$. Note that changing flavour is equivalent to changing the sign of q_x in the Hamiltonian.

6.3 Extending the Dirac Hamiltonian by modifying the lattice parameters

We now generalize the free Dirac Hamiltonian to include a variety of external fields:

$$H_D = c\,\vec{\alpha}\cdot\vec{p} + \beta mc^2 + \beta V_{cov}. \tag{6.14}$$

Here m is the mass of the particles and V_{cov} is the most general covariant potential containing scalar, vector, matrix, pseudoscalar, pseudovector and pseudotensor fields. The Dirac matrices $\alpha^i = \gamma^0\gamma^i$ and $\beta = \gamma^0$, are defined in terms of the generators of the Clifford group, γ^μ. In 2+1 dimensions this is a set of 2×2 matrices satisfying the anticommutation relations $\{\gamma^\mu, \gamma^\nu\} = 2\eta^{\mu\nu}$ with $\eta^{\mu\nu} = diag(1,-1,-1)$, where $\mu,\nu = 0,1,2$. The choice $\vec{\alpha} = \vec{\sigma} = (\sigma_x, \sigma_y)$ and $\beta = \sigma_z$ corresponds directly to the Hamiltonian in equation (6.6). The Dirac Hamiltonian then has the form

$$H_D = c\,\vec{\sigma}\cdot\left(\vec{p} - e\vec{A}(\vec{r})\right) + eA^0(\vec{r})\,\mathbb{I} + \left(mc^2 + V(\vec{r})\right)\sigma_z, \tag{6.15}$$

where $A^0(\vec{r})$ and $\vec{A}(\vec{r})$ are the usual scalar and vector potential that give rise to observable electric and magnetic fields, and $V(\vec{r})$ is a scalar potential that mimics the effect of an imposed mass; e is an effective charge. Note that since the fields $\vec{A}$ and A^0 do not have any dynamics, we may assume $e = 1$, for convenience. Let us now show how to recover all terms in equation (6.15) by slightly perturbing the tight-binding model.

6.3.1 Generating a mass term

The simplest term that we can add to Hamiltonian equation (6.2) is an energy difference between atoms in sublattices A and B:

$$\delta H = \sum_m \left(\frac{\varepsilon}{2} a_m^\dagger a_m - \frac{\varepsilon}{2} b_m^\dagger b_m\right), \tag{6.16}$$

which in the continuum limit becomes

$$\delta H = \sum_\tau \int \left(\frac{\varepsilon}{2}\hat{\Psi}_{a\tau}^\dagger(\vec{r})\hat{\Psi}_{a\tau}(\vec{r}) - \frac{\varepsilon}{2}\hat{\Psi}_{b\tau}^\dagger(\vec{r})\hat{\Psi}_{b\tau}(\vec{r})\right)\mathrm{d}^2 r \tag{6.17}$$

or equivalently

$$\delta h(\vec{r}) \sim \sigma_z \frac{\varepsilon}{2}. \tag{6.18}$$

Comparing this with equation (6.15), we see that the position-independent term proportional to σ_z can be identified with an effective mass.

6.3.2 Abelian potentials

We can extend our model by starting from equation (6.2) and smoothly modifying the hoppings as $J_i = J + \epsilon_{i,m}$ where $|\epsilon| \ll |J|$:

$$\delta H = \sum_{m,i} \epsilon_{i,m} a^{\dagger}_{m} b_{m+v_i} + \text{H.c.} \tag{6.19}$$

In the continuum limit this renders

$$\delta H = \sum_{\tau,i} \int e^{i\vec{K}\cdot\vec{v}_i} \epsilon_i(\vec{r}) \hat{\Psi}^{\dagger}_{a\tau}(\vec{r}) \hat{\Psi}_{b\tau}(\vec{r}+\vec{v}_i) \mathrm{d}^2 r. \tag{6.20}$$

In the notation of the previous section, this is equivalent to a change in the "coupling term" between pseudospins:

$$\delta C_\tau = \frac{\sqrt{3}}{2}\left(\tau\frac{\epsilon_0}{J} - \tau\frac{\epsilon_1+\epsilon_2}{2J} + i\frac{(\epsilon_2-\epsilon_1)}{J}\right) \tag{6.21}$$

therefore allowing us to formally derive an Abelian external potential

$$H = c\,\vec{\sigma}\cdot\left(\vec{q} - \vec{A}(\vec{r})\right) \tag{6.22}$$

where $\vec{A} = (\tau\mathrm{Re}[\delta C_\tau], \mathrm{Im}[\delta C_\tau])$.

6.3.3 Scalar fields

Consider now perturbations which are diagonal in the internal space to the tight-binding Hamiltonian, such as those given by intralattice hoppings in equation (6.1):

$$\delta H = \sum_m \sum_{i=1}^{3} \Gamma_A a^{\dagger}_m a_{m+v_i} + \Gamma_B b^{\dagger}_m b_{m+v_i} + h.c. \tag{6.23}$$

Following the continuum limit performed in section 6.3.1 the Hamiltonian in momentum space around the K_τ point can then be written as

$$H'_\tau = c\,\vec{\sigma}\cdot\vec{q} - \begin{pmatrix} \sum_i e^{-i\vec{K}_\tau\cdot\vec{v}_i}\Gamma_A(\vec{r}) & 0 \\ 0 & \sum_i e^{-i\vec{K}_\tau\cdot\vec{v}_i}\Gamma_B(\vec{r}) \end{pmatrix}, \tag{6.24}$$

or purposefully rewritten (reabsorbing the constant $\sum_i e^{-i\vec{K}_\tau \vec{v}_i}$ flavour-dependent factor) as

$$H'_\tau = c\,\vec{\sigma}\cdot\vec{q} - \frac{(\Gamma_A(\vec{r}) + \Gamma_B(\vec{r}))}{2}\mathbb{I} - \frac{(\Gamma_A(\vec{r}) - \Gamma_B(\vec{r}))}{2}\sigma_z \tag{6.25}$$

which has both a term proportional to $\mathbb{I}$ representing an electric potential, $\phi_\pm(\vec{r}) = \sum_i e^{-i\vec{K}_\pm\cdot\vec{v}_i}\frac{1}{2}[\Gamma_A(\vec{r}) + \Gamma_B(\vec{r})]$, and a term proportional to σ_z which contributes to the effective mass.

6.3.4 Flavour-coupling perturbations

We have seen that spatial variations of the hopping elements emerge as an Abelian external field. These variations have to be *small*, but it should be stated that, in order to keep flavours decoupled, they also have to be *spatially smooth.* Otherwise, and if there is a modulation with wavevector comparable to the order $(\vec{K}_+ - \vec{K}_-)$, the flavour-coupling terms $\tau \neq \zeta$ in equation (6.8) do not vanish. The simplest flavour-coupling perturbation is a plane wave whose wavelength is comparable to the lattice constant and thus bridges the difference in momentum between cones. For instance

$$\delta\hat{H} = \sum_{m,i} 2\chi_{x,i,m} \cos\left[\vec{r}\cdot(\vec{K}_+ - \vec{K}_-)\right] a_m^\dagger b_{m+v_i} \tag{6.26}$$

with a constant coupling strength $\chi_{x,i,m} = \chi_x$. These rapid oscillations only allow the survival of terms that couple different cones, cancelling all terms inside the same cone. The most general perturbation of this sort is

$$\delta\hat{h}(\vec{r}) = \chi_x(\vec{r})\left(\hat{\Psi}_{a+}^\dagger\hat{\Psi}_{b-} + \hat{\Psi}_{a-}^\dagger\hat{\Psi}_{b+} + \text{H.c.}\right), \tag{6.27}$$

where χ_x is the spatial dependence of the slow envelope that surrounds our perturbation (6.26). Actually, this envelope can be "remodulated" in order to make flavour coupling also weakly spatial-dependent. Moreover, we can also introduce in equation (6.26) sine terms, $\epsilon(\vec{r}) = \chi_y \sin\left[\vec{r}\cdot(\vec{K}_+ - \vec{K}_-)\right]$, which make the flavour-coupling term complex.

6.3.5 The complete Dirac Hamiltonian

Since there exist no pseudo-potentials ($\gamma^5 = 1$ in $2+1$ dimensions), our idea of perturbing the tight-binding model parameters allows us to reconstruct all possible external potentials of the Dirac equation, plus an additional coupling between different types of particles. With all these elements we have the following effective single-particle Hamiltonian:

$$h(\vec{r}) = \begin{pmatrix} c\,\vec{\sigma}\cdot[\vec{q}-\vec{A}(\vec{r})] + m\sigma_z c^2 + \phi_+(\vec{r}) & \chi_x\sigma_x + \chi_y\sigma_y \\ \chi_x\sigma_x + \chi_y\sigma_y & -c\{\vec{\sigma}\cdot[\vec{q}-\vec{A}(\vec{r})]\}^* + mc^2\sigma_z + \phi_-(\vec{r}) \end{pmatrix}. \tag{6.28}$$

6.4 Trapping of atoms in an optical honeycomb lattice

This section will be a small extension of chapter 3, in that it reviews the optical lattice technology that is used in this proposal. Here we explain how to construct a honeycomb lattice with two state-dependent triangular optical lattices. We then discuss how to implement the previous tight-binding Hamiltonians and propose an experimental setup to obtain the Dirac field and the external potentials by using solely Raman and detuned laser beams.

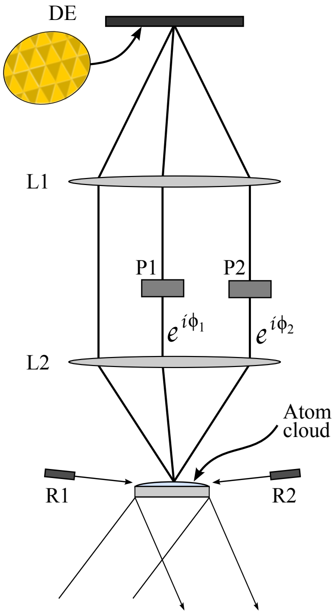

Fig. 6.3: Proposal of experimental setup. DE is the diffraction element, L1 and L2 are the required lenses to make the beams parallel and to focalize them on the lattice plane, R1 and R2 are the lasers used for the Raman transitions, P_1 and P_2 are phase plates used to change the relative phases, $e^{i\phi_{1,2}}$, of the σ^+ and σ^- beams.

6.4.1 From two triangular sub-lattices to a honeycomb lattice

Recent advances in the development of high-aperture objectives and their integration in optical traps open the door to the generation of almost arbitrary two-dimensional potential landscapes for ultracold atoms. The basic idea is that off-resonant light may be used to tightly confine atoms in the maxima or minima of intensity, recreating sophisticated lattice models [47]. While those minima and maxima are ususally generated through the interference of multiple laser beams [38, 47], a novel paradigm consists on shaping and organizing those intensity profiles by simply projecting sophisticated images on the two-dimensional focal plane of a lens. Some experiments along this line have reproduced the usual square lattice quantum simulations [14] and also demonstrated triangular lattices [55].

In this proposal we are particularly interested in the last of those setups, which combines two triangular lattices [55] in the same plane. In this kind of experiment the trapping laser beams are first diffracted by a holographic mask with a triangular pattern, selecting the first diffraction orders, which are then collected by a powerful lens to create the imprinted intensity pattern at its focal plane. The relative phases of the three diffracted beams may be independently controlled in a way that allows the displacement of the resulting triangular lattice (cf. figure 6.3). When this procedure is applied to two laser beams that differ in frequency or polarization, it becomes possible to produce two triangular lattices, A and B, which coexist on the same plane and have a tunable relative separation. The result is the original setup introduced in figure 6.1 in an abstract way, where now A and B are physically implemented by an optical potential.

In order to jump from two independent triangular lattices to the setup introduced in figure 6.1, we need means to introduce the couplings between different lattice sites, that is hoppings from one lattice to another, or within the same lattice. The most direct way to implement this in an optical system is to use the two lattices A and B to trap atoms of the same species but in different internal states, $|a\rangle$ and $|b\rangle$ respectively. We also need a way to rotate between $|a\rangle$ and $|b\rangle$, which can be implemented via Raman transitions. In a situation with all these ingredients two kinds of hoppings are allowed for the atoms: on the one hand an atom in sub-lattice A (B) can tunnel between positions in its own sub-lattice, as contemplated in our model by the hopping parameter Γ_A (Γ_B). This parameter can be controlled by increasing or decreasing the intensity I_A (I_B) of the laser beam generating each sublattice. On the other hand a Raman-induced change in the internal state of an atom from $|a\rangle$ to $|b\rangle$ (from $|b\rangle$ to $|a\rangle$) will make the atom shift from sublattice A to sublattice B (B to A). These nearest-neighbour jumps can be different in each of the three possible directions, and are modelled by the hopping parameters J_0, J_1 and J_2 which are associated with the vectors $\vec{v}_0$, $\vec{v}_1$ and $\vec{v}_2$ shown in figure 6.1.

6.4.2 Realization of two state-dependent triangular sub-lattices

How do we implement in practice the ideas from the previous subsection, and in particular the coupling between lattices? The engineering and control of state-dependent lattices is a mature technology [47, 64], which nevertheless requires some careful control of the atomic states and decoherence. We will briefly describe how this works for fermionic alkaline atoms and how this integrates with the projected lattices scheme. However, it must also be noted that hard work is being done to try to implement state-dependent lattices with alkaline-earth atoms, which are less prone to heating [31].

As sketched in figure 6.4, it is possible to find a wavelength $\bar{\lambda}_l$ falling between the $D1$ and $D2$ lines of an alkaline atom for which polarised light only traps atoms in one of the ground states manifolds. More precisely, the fine-structure energy levels of alkaline atoms are denoted by $|L, J, m_J\rangle$, where L is the electron angular momentum quantum number, $\vec{J}$ the combined orbital and spin momentum and m_J is its projection along the quantization axis. When we illuminate with σ^+ polarised light at a frequency $\omega = \frac{1}{2}(\omega_{D1} + \omega_{D2})$, the ac-Stark shift that it induces on the $\left|0, \frac{1}{2}, -\frac{1}{2}\right\rangle$ cancels due to the positive and negative contribution of off-resonant $D1$ and $D2$ transitions. The result is that circularly polarized $\sigma^{\pm}$ light can only trap atoms in the $\left|0, \frac{1}{2}, \pm\frac{1}{2}\right\rangle$ states, respectively.

In practice, however, the situation is more subtle because atoms also have

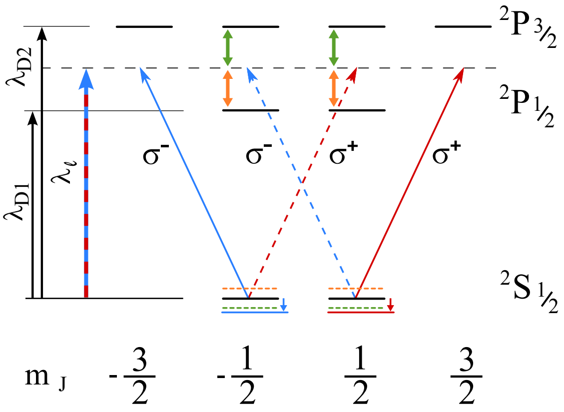

Fig. 6.4: Fine-structure energy levels of an alkaline atom. *Not to scale.* λ_{D1} and λ_{D2} are the wavelengths of the D1 and D2 lines respectively. λ_l is the wavelength of the optical lattice lasers. Dashed lines mark the cancelled ac-Stark effects: a σ^+ (σ^-) polarised photon incident on a $\left|L=0, J=\frac{1}{2}, m_J=-\frac{1}{2}\right\rangle$ $\left(\left|0,\frac{1}{2},+\frac{1}{2}\right\rangle\right)$ state would see both the $\left|1,\frac{1}{2},\frac{1}{2}\right\rangle$ and the $\left|1,\frac{3}{2},\frac{3}{2}\right\rangle$ $\left(\left|1,\frac{1}{2},-\frac{1}{2}\right\rangle \text{ and } \left|1,\frac{3}{2},-\frac{3}{2}\right\rangle\right)$ states in such a way that the ground level energy displacements cancel with each other. The net effect is then only due to σ^- (σ^+), marked with continuous lines.

some hyperfine structure, induced by the coupling between the electronic and nuclear angular momenta. Let us focus on the fermionic species ^{6}Li, in line with previous proposals [55]. Out of the hyperfine ground-states $|F, m_F\rangle_{HF} = c_1\left|J=\frac{1}{2}, m_J=\frac{1}{2}\right\rangle + c_2\left|J=\frac{1}{2}, -\frac{1}{2}\right\rangle$ where $\vec{F} = \vec{I} + \vec{J}$ being $\vec{I}$ the nuclear angular momentum of ^{6}Li $(I=1)$, we select $|a\rangle = \left|\frac{1}{2}, -\frac{1}{2}\right\rangle_{HF} = -\sqrt{\frac{2}{3}}\left|\frac{1}{2}, \frac{1}{2}\right\rangle + \frac{1}{\sqrt{3}}\left|\frac{1}{2}, -\frac{1}{2}\right\rangle$ and $|b\rangle = \left|\frac{3}{2}, -\frac{3}{2}\right\rangle_{HF} = 1\left|\frac{1}{2}, -\frac{1}{2}\right\rangle$. If V_+ and a V_- are the intensity distributions that result by illuminating with light in the σ^+ and σ^- polarisations, the states $|a\rangle$ and $|b\rangle$ will feel the ac-Stark potentials $V_A = \frac{2}{3}V_+ + \frac{1}{3}V_-$ and $V_B = V_-$. As shown in figure 6.5, the combined potentials can look like two displaced triangular lattices by choosing the adequate relative phases between the diffracted beams. Furthermore, the relative depths can be controlled by changing the ratio V_+/V_-, but this may require a new tuning of the relative phases.

The last ingredient is a coupling between both lattices. This can be done using a Raman laser that couples both internal states, $|a\rangle$ and $|b\rangle$. When an atom in state $|a\rangle$ is affected by the laser, it will switch state, but since the energy must be conserved, this implies tunneling to a neighboring site in the other lattice. This qualitative description assumes that atoms in the A and B sublattices are confined to the lowest energy band.

It is therefore important to ensure that the presence of the optical lattice does not lead to unwanted transitions and heating of the system. Since the lattice laser frequency has to lie between the D1 and D2 lines, the maximum detuning from a resonance is half the difference between those transition energies. Because of the narrow fine structure of ^{6}Li, we estimate a loss rate of about $0.01J - 0.1J$

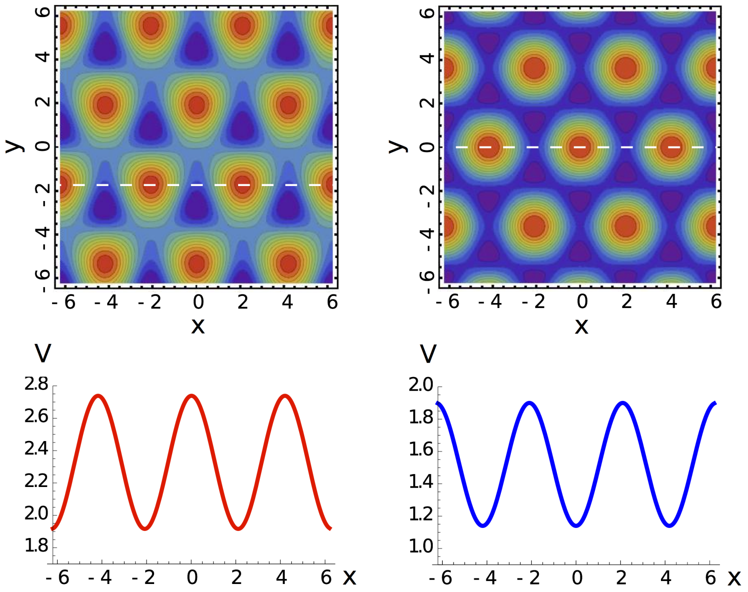

Fig. 6.5: *Left*: sub-lattice generated by $V_A = \frac{2}{3}V_+ + \frac{1}{3}V_-$. *Right*: sub-lattice generated by $V_B = V_-$. *Top*: trapping potentials as functions of x and y, in arbitrary units. The red zones represent the potential minima where the atoms are trapped. It is apparent that both sub-lattices are triangular and displaced one with respect to the other. By superimposing both images one obtains the structure of an hexagonal lattice. *Bottom*: transversal cut corresponding to the white dashed line along the x direction. The difference in potential depth can be controlled by changing the ratio V_+/V_-, but this will affect the relative positions of the potential minima.

for lattice depths of $5E_R - 30E_R$ (E_R is the recoil energy, see below) and $J \simeq$ 1kHz. This problem can be better addressed by using ^{40}K, which for an analogous lattice features a loss rate below $10^{-3}J$, or by using alkaline-earth species (such as Yb) [31]. A very important question is whether this tight-binding approximation is compatible with the Raman laser. This will be discussed in the following section.

6.4.3 Band structure calculations

Our experimental proposal relies on the possibility to combine two different lattices and couple them via Raman assisted tunneling. The feasibility of this procedure has been experimentally demonstrated in a superlattice experiment [4]. It has also been discussed at length in the various works that suggest implementing gauge fields via photon-assisted tunneling, beginning with the seminal paper by Jaksch and Zoller [48]. Despite this, it is very illustrative to do a quantitative discussion of the lattice parameters involved in this setup, with the aim of clarifying what hopping, $\Gamma_{A,B}$ and coupling strengths, J_i, can be achieved, and what is the limit of weak perturbations that we will rely on later in the chapter.

Our basic tool in this discussion is the expansion of the field operator in terms of Wannier wavefunctions(see Sec. 3). We will assume that the two triangular lattices are defined using a similar potential, $V_{\text{triang}}(\vec{x})$, which for the sake of concreteness we choose to be

$$V_{\text{triang}}(\vec{x}) = V_0\left[3 - 2\cos(2\pi x)\cos(2\pi y/\sqrt{3}) - \cos(4\pi y/\sqrt{3})\right]. \tag{6.29}$$

This potential gives rise to two single-particle Hamiltonians, with a relative displacement given by $\vec{v}_4$(see figure 6.1):

$$\begin{aligned} H_A &= -\frac{\hbar^2}{2m}\boldsymbol{\nabla}^2 + V_{\text{triang}}(\vec{x}/d), && (6.30)\\ H_B &= -\frac{\hbar^2}{2m}\boldsymbol{\nabla}^2 + V_{\text{triang}}[(\vec{x}-\vec{v}_4)/d], && (6.31)\end{aligned}$$

whose eigenstates are the Bloch waves $\psi_{\vec{k}}(\vec{x})$. The Wannier functions are sums over these Bloch states in a Brillouin zone, $w(\vec{x}) = \frac{1}{|\mathcal{B}|^{1/2}}\int \psi_{\vec{k}}(\vec{x})\mathrm{d}^2k$ and we assume that they have the same shape for both lattices. Furthermore, we assume that there is a strong confining harmonic potential in the z-direction such that the atoms are restricted to its vibrational ground state with an approximate length scale $(\hbar/m\omega)^{1/2} \sim d$.

In the low energy limit that is usual for these experiments, the fermionic field may be approximated by a linear combination of these localized states

$$\hat{\psi}_a(\vec{x})^\dagger \simeq \sum_m \hat{a}_m^\dagger w(\vec{x}-\vec{x}_m),\ \hat{\psi}_b(\vec{x})^\dagger \simeq \sum_m \hat{b}_m^\dagger w(\vec{x}-\vec{x}_m-\vec{v}_4). \tag{6.32}$$

In this limit, the motion of particles is described by a tight-binding Hamiltonian, where the intralattice hopping amplitude is defined as the nearest-neighbor term of the Hamiltonian using this expansion, or

$$\Gamma_A = \int w(\vec{x}-\vec{v}_{1,2,3})^\star H_A w(\vec{x})\mathrm{d}^2x, \tag{6.33}$$

and similarly for Γ_B. If we also include a Raman coupling among lattices, characterized by a Rabi frequency Ω, we may still use the tight-binding approximation provided that this frequency is much smaller than the gap between the lowest energy band and the first excited band of the triangular lattice, $|\Omega| \ll \Delta E$. If this is the case, we will have that the interlattice coupling can be estimated as

$$J = \Omega\int w(\vec{x}-\vec{v}_4)^\star w(\vec{x})\mathrm{d}^2x. \tag{6.34}$$

Note that for equation (6.32) to remain valid, Ω has to be small when compared with ΔE, not with the actual hoppings. This means that the ratio between J and $\Gamma_{A,B}$ is not fixed, and that one hopping does not have to be small with respect to the other one.

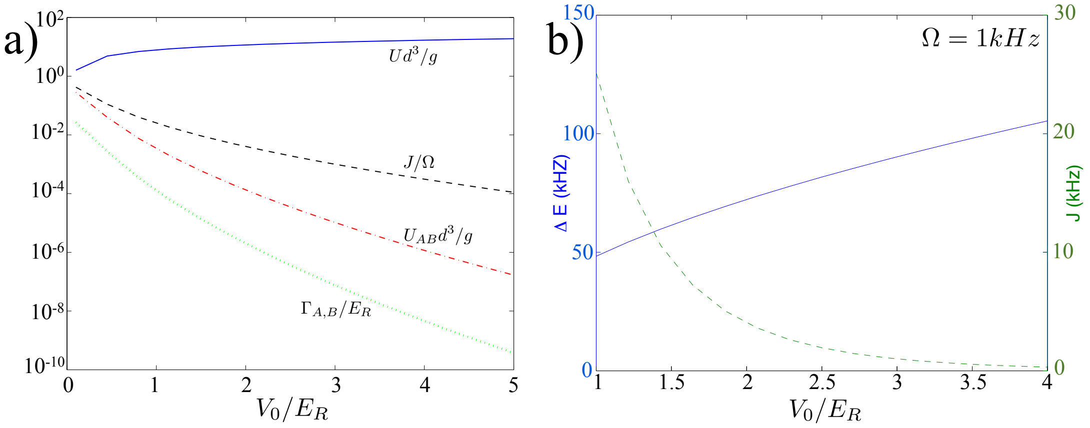

Fig. 6.6: a) Dependence of the tight-binding parameters on the intensity of the confining lattice potential. We have numerically calculated the values of the on-site interaction strength Ud^3/g (solid, blue), the hexagonal tunneling amplitude J/Ω (black, dashed), the interlattice interaction stregth $U_{AB}d^3/g$ (red, dotted-dashed) and the triangular tunneling amplitude $\Gamma_{A,B}/E_R$ (green, dotted). b) Comparison between the Bloch band energy gap (solid line; left axis) and the tunneling parameter J (dashed, right axis) for ^{40}K and varying lattice depths. $\Omega = 1kHz$ has been chosen so that $\Omega \ll \Delta E$ while keeping J still significant. The band gap is even bigger for ^{6}Li, because of its larger E_R.

We have computed numerically the Wannier functions for a triangular lattice setup using a discretization of the Brillouin zone with 100 modes and expanding the Bloch wave with up to 625 modes. Using this we have estimated the integrals corresponding to the hoppings, and also to the on-site and nearest-neighbor interactions, given by

$$U = \frac{g}{d}\int_{\mathcal{C}} |w(\vec{x})|^4 \mathrm{d}^2x \tag{6.35}$$

$$U_{AB} = \frac{g}{d}\int_{\mathcal{C}} |w(\vec{x})|^2 |w(\vec{x}-\vec{v}_4)|^2 \mathrm{d}^2x, \tag{6.36}$$

where $\mathcal{C}$ denotes the surface of the unit cell. The results are shown in Fig. 6.6a, where we used the recoil energy $E_R = 4\pi^2\hbar^2/2md^2$ as unit of energy to ease the comparison, typical values for the lattice spacing $(400-600\ \mathrm{nm})$, and interaction strength values for alkaline fermions which range from $g/d^3 \simeq 0.01E_R$ (^{40}K) to $g/d^3 \simeq 0.1E_R$ (^{6}Li) [55]. Note how the ratio J/Ω is at least 100 times larger than $\Gamma_{A,B}/E_R$ for reasonable values of the potential depth. This means that even if we have to impose $\Omega \ll \Delta E$, we still can reach a regime in which $J \simeq \Gamma_{A,B}$, as shown in Fig. 6.6b. Note also that while the interlattice term U_{AB} decreases rapidly, there is still a window of values where it might be comparable to the influence of hopping, opening the door to experiments with gauge fields *and* interactions.

6.5 Perturbing the hopping parameters

In the previous discussion we have presented a feasible setup to obtain a honeycomb tight-binding Hamiltonian with neutral atoms in an optical lattice. In this section we take the scheme one step further so that the hopping parameters can be locally changed to incorporate mass terms and pseudofields to the Dirac Hamiltonian. We propose to optically control the Dirac field physics much in the way mechanical strains have been suggested in graphene sheets [73, 94]. Two proposals to implement variations are presented, the first of which is best in line with the setup shown in the previous section, the other being a more formal approach to general hopping calculations across potential wells.

6.5.1 Spatial dependence of Raman intensity

Interlattice hoppings are assisted by an external laser beam inducing Raman transitions between the internal states of the atoms, thus creating a transition amplitude which scales with the intensity of the beam. By changing the spatial dependence of this amplitude one can overprint a first-neighbours hopping perturbation $\epsilon_i(\vec{r})$. This method is the easiest to implement in this setup, but is very limited and unable to act on intralattice (next-to-nearest-neighbour) transitions. Therefore it is the chosen method to add Abelian vector potentials and non-Abelian coupling terms.

6.5.2 Lattice distortions

A more general analysis can be made by considering spatial distortions of the lattice, that is, either through a relative displacement of one site with respect to its neighbor or by adjusting the width of the individual potential wells. The displacement may be achieved by controlling the relative phases of the conforming beams through the phase modulators *P1* and *P2* in figure 6.3. The width of the potential wells can be modified by a change in the height of the confining potential, using a mask which modulates the intensity of the laser beams. We now develop a simple model for calculating the influence of these two modifications in the hopping parameters.

We assume that the ideal (unperturbed) hopping parameters between wells behave as if lattice sites were spatially separated harmonic oscillators in an original reference frame $\vec{r}'$. The lattice distortion described locally by the transformation $\vec{r}' = A\vec{r}$ renders the following single-well Hamiltonian:

$$\hat{H} = \frac{-\hbar^2}{2m}\Delta + \frac{m\tilde{\omega}^2}{2}\vec{r}^T A^T A\vec{r} \tag{6.37}$$

where the frequency of the site trap is also changed $\omega \to \tilde{\omega}(\vec{r})$, due to modulations of the intensity of the confining beam (the kinetic energy terms are not transformed since they are expressed in “real” space, while the potential term is meant to look like a perturbed harmonic oscillator). The localized Wannier function in the well is

$$\psi_{GS}(x) = \frac{1}{\sqrt{N}} \exp(-\frac{1}{2\sigma^2} \vec{r}^T B \vec{r}) \tag{6.38}$$

where $B = \sqrt{A^T A}$, $\sigma^2 = \hbar/m\tilde{\omega}$ and $N = \pi\sigma^2/\sqrt{|B|}$. Notice that B is positive-definite by construction and σ is $\vec{r}$-dependent. If we assume no vibrational levels can be excited, the hopping parameter between first-neighbour wells separated by a vector $\vec{a}$ is simply proportional to the overlap between wavefunctions

$$J \sim \int \psi^*_{GS}(\vec{r}) \psi_{GS}(\vec{r} - \vec{a}) \mathrm{d}^2 r = \exp(-\frac{\vec{a}^T B \vec{a}}{4\sigma^2}). \tag{6.39}$$

This will be valid as long as variations are smooth and small, corresponding to the wavefunctions being good approximations to the ground state of the potential well and the restriction to the lowest vibrational level. Therefore the dislocation must be small: $A \simeq \mathbb{I} + \epsilon C \rightarrow G = A^T A \simeq \mathbb{I} + \epsilon(C + C^T)$, defining C as our generator. Let us call the unperturbed vector connecting both wells $\vec{a}_0$, so that the actual vector becomes $\vec{a} = A^{-1}\vec{a}_0 = (\mathbb{I} - \epsilon C)\vec{a}_0$. The bilinear matrix expands as $B = \sqrt{G} \simeq \sqrt{\mathbb{I} + \epsilon(C + C^T)} \simeq \mathbb{I} + \frac{1}{2}\epsilon(C + C^T)$. Substituting these values yields:

$$\begin{aligned} J &\sim \exp(-\frac{\vec{a}^T B \vec{a}}{4\sigma^2}) \Rightarrow J = J_0 \exp(-\epsilon\delta), \\ \delta &= -\frac{m\tilde{\omega}(\vec{r})}{8\hbar} \vec{a}_0^T (C + C^T)) \vec{a}_0. \end{aligned} \tag{6.40}$$

This result can be readily interpreted. There are two contributions: one $(C + C^T)$ which modifies the hopping due to the change in distance between wells, and another $(\tilde{\omega}(\vec{r}))$ which refers to the intensity profile of the confining laser beam. We can therefore tune these parameters, e.g. displacing or rotating one sublattice on top of the other, to allow for variations of the tight-binding hoppings. As explained before, all these changes are used to simulate Abelian and non-Abelian external gauge fields.

6.6 Experimental detection

The most direct consequence of the appearance of Abelian and non-Abelian external fields is the distortion of the energy bands, ranging from the movement of the Dirac cones in momentum space to the appearance of a gap in the spectrum. Two methods are proposed here to observe these changes: the first one is the measurement of the momenta after removing the confining potential so as to explore the form of the energy bands; the second one focuses on measuring how these fields affect the dynamics of a single particle (or small group of particles) moving in the lattice.

It is worth mentioning that some of the techniques first commented here will prove crucial to extract information about the topological nature of the cloud, as we will see in the following chapters.

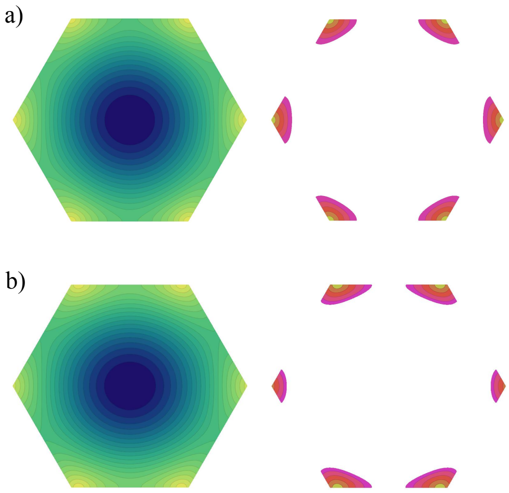

Fig. 6.7: Expected momenta distribution for B (*left*) and A (*right*) atoms associated with the E_- and E_+ energy bands respectively (see text). The two *top* images correspond to the unperturbed honeycomb tight-binding Hamiltonian, and the *bottom* ones correspond to the *Abelian potential* case described in section 6.3 due to a perturbation in J_0.

6.6.1 Time of flight images

It is possible to probe the atomic population within the first Brillouin zone (BZ) of an optical lattice. The procedure consists of the following steps: (i) adiabatically switching off the lattice potentials so that the atoms quasimomenta are converted into real momenta, (ii) then letting the atoms expand freely during a certain time of flight and (iii) finally taking an absorption image of the expanded cloud [56].

In our setup the situation is a bit more complicated. Let us denote by $|+,\vec{k}\rangle$ and $|-,\vec{k}\rangle$ the eigenstates associated with upper and lower energy bands, $E_+(\vec{k})$ and $E_-(\vec{k})$, of the tight-binding Hamiltonian (6.2). In a ground state with a Fermi energy slightly above zero, we would have many atoms in the lower band sector occupying the whole of the first BZ and only few atoms in the upper band, concentrated around Dirac points (See figure 6.7a). Despite the difference, by means of absorption images one can not distinguish between $|+\rangle$ and $|-\rangle$ states as both have components corresponding to the $|a\rangle$,$|b\rangle$ internal states of the atoms.

In order to picture the Dirac cones we need a method that discriminates between energy bands, say, transforming all the $|+\rangle$ states into $|a\rangle$'s and all the $|-\rangle$ states into $|b\rangle$'s, while preserving the momentum, $\vec{k}$. The adiabatic theorem provides us the way for doing this. Our starting point is the honeycomb lattice Hamiltonian in momentum space

$$\tilde{H} = J\sum_{\vec{k}} u^{\dagger}_{\vec{k}} \left[f(\vec{k})\sigma^{+} + f^{\star}(\vec{k})\sigma^{-} \right] u_{\vec{k}}, \tag{6.41}$$

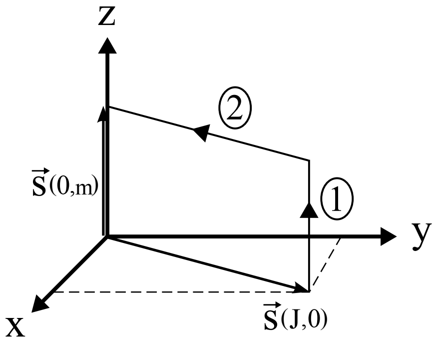

Fig. 6.8: Adiabatic path for a transformation of the $|+\rangle$, $|-\rangle$ states into $|a\rangle$, $|b\rangle$ states. The hamiltonian of the system is written as $H \sim \vec{s}(J, m) \cdot \vec{\sigma}$, so $\vec{s}_{initial} = \vec{s}(J, 0)$ lies in the x, y plane while $\vec{s}_{final} = \vec{s}(0, m)$ lies along the z axis. During the first step m is adiabatically increased, and during the second J is adiabatically decreased until zero.

Tab. 6.1: summary table of all the considered perturbations of the hopping parameters with their physical effects.

Lattice modification	Hamiltonian modification	Effect
$J_i = J + \epsilon_i$ i=0,1,2 small hopping parameter modification	$H \to c\vec{\sigma} \cdot (\vec{q} - \vec{A})$ $\vec{A} = (\tau \mathrm{Re}[\delta C_\tau], \mathrm{Im}[\delta C_\tau])$	Abelian field
$+\sum_m \left(\frac{\varepsilon}{2} a_m^\dagger a_m - \frac{\varepsilon}{2} b_m^\dagger b_m\right)$ energy difference between A and B	$H \to c\vec{\sigma} \cdot \vec{q} + \frac{\varepsilon}{2}\sigma_z$	Mass term
Γ_A, Γ_B intrasublattice triangular hoppings	$H \to c\vec{\sigma} \cdot \vec{q} + \frac{1}{2}(\Gamma_A + \Gamma_B)\mathbb{1} + \frac{1}{2}(\Gamma_A - \Gamma_B)\sigma_z$	Scalar field
$\epsilon(\vec{r}) = \chi_x \cos(\vec{r}(\vec{K}_+ - \vec{K}_-))$	$\delta\hat{h}(\vec{r}) = \chi_x(\hat{\Psi}_{a+}^\dagger \hat{\Psi}_{b-} + \hat{\Psi}_{a-}^\dagger \hat{\Psi}_{b+} +$ H.c.)	Flavour coupling

written with the pseudospin structure $u_{\vec{k}} = (a_{\vec{k}}, b_{\vec{k}})$, the couplings $f(\vec{k}) = 1 + e^{i\vec{k}\cdot\vec{v}_1} + e^{-i\vec{k}\cdot\vec{v}_2}$, and the Pauli ladder operators $\sigma^\pm$. Note how the Hamiltonian is a composition of commuting terms for each value of the momentum, $\vec{k}$. We will adiabatically distort all terms, following the route in figure 6.8, which consists on first adding a mass term, $\sim m\sigma^z$, and then decreasing J down to zero. The protocol maps the two eigenstates of the initial Hamiltonian, $|+\rangle$ and $|-\rangle$, to $|a\rangle$ and $|b\rangle$, accurately.

This technique would allow for the experimental observation of the effects of an Abelian potential described in section 6.3, as represented in figure 6.7b, where the Dirac cone displacement manifests as a deformation of the $|a\rangle$-momentum distribution. In general all other effects, which are summarized in Table 6.1, could be observed by similar methods.

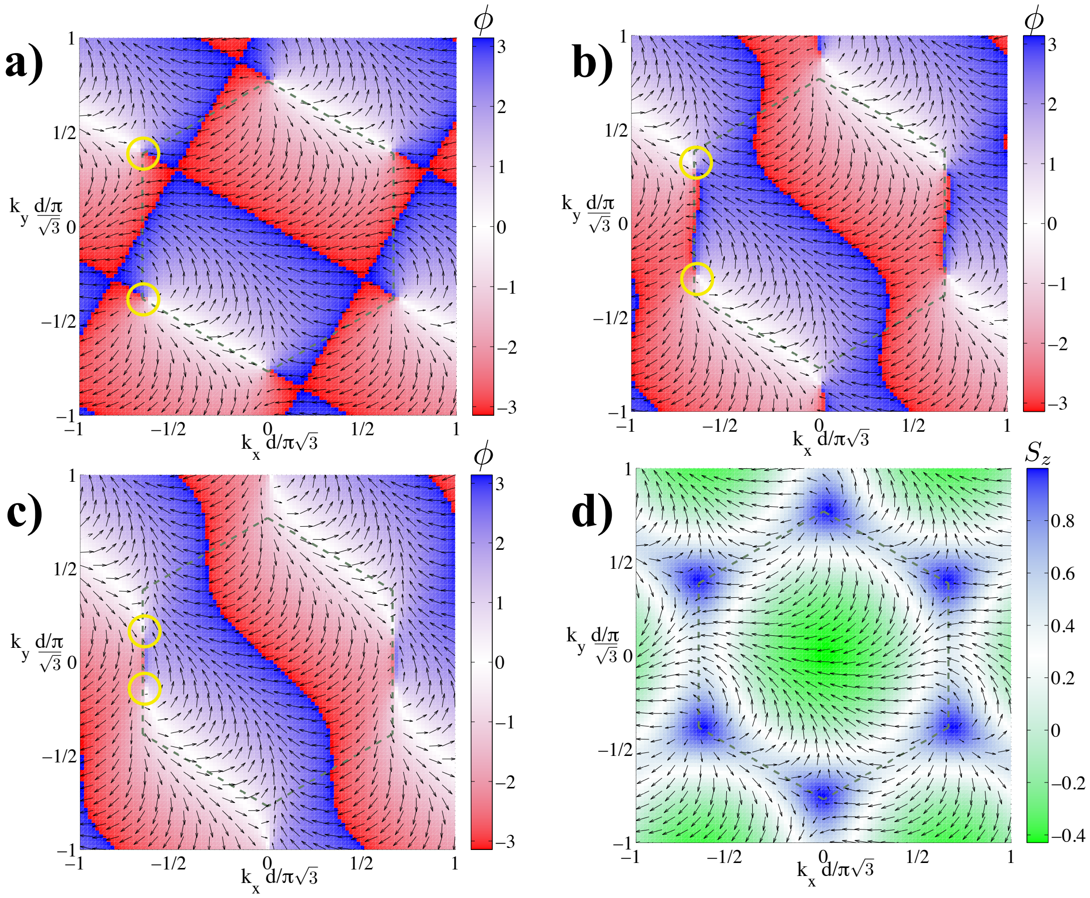

Fig. 6.9: a),b),c): Effect of the Abelian potential by the spin texture method. In color scale, $\phi = \tan^{-1}(S_y/S_x)$. The yellow circles show the position of the Dirac cones for $\vec{A} = \vec{0}, (1/\sqrt{48}, 0)/d, (1/\sqrt{12}, 0)/d$ respectively. d) Effect of a non-zero intralattice hopping ($\Gamma_A \neq 0$). In all panels, the (S_x, S_y) vector field is plotted to show the Dirac cones, where the value of S_z is maximal. This reveals that the intralattice hopping generates a gap in the energy spectrum.

6.6.2 Spin textures in time-of-flight images

The bipartite nature of the honeycomb lattice allows us to separately probe the atomic population densities for each hyperfine state. We can compare these values at each point of the Brillouin zone to obtain a field $\hat{S}_z(\vec{k}) = a_k^\dagger a_k - b_k^\dagger b_k$. Moreover, an adiabatic protocol such as the one described in the previous subsection or in-flight Raman-assisted internal state rotations provide a way of measuring the "rotated" fields $\hat{S}_x(\vec{k}) = a_k^\dagger b_k + b_k^\dagger a_k$ and $\hat{S}_y(\vec{k}) = i(a_k^\dagger b_k - b_k^\dagger a_k)$. This observable vector field on the Brillouin zone ($\boldsymbol{S}(\vec{k}) = \left\langle \hat{S}_x, \hat{S}_y, \hat{S}_z \right\rangle$) is a powerful tool to analyze some distinct features of the ground state: the presence of a gap in the energy band structure ($S_z(\vec{K}_\pm) \neq 0$), the characteristic state differences between cones or even the topological nature of the ground state [6].

In figure 6.9 we show a simulation of such a measurement in two distinct cases: figures 6.9a, 6.9b, 6.9c feature the value of the phase $\phi = \tan^{-1}(S_y/S_x)$ for different values of the Abelian potential $\vec{A}$. The displacement of the cones provoked by $\vec{A}$ along the Brillouin zone is apparent, as it is the fact that the cones are vortices in the S_x, S_y vector field. Figure 6.9d illustrates how a gap or effective mass created by a non-zero value of Γ_A can be observed by measuring S_z. Once again, the Brillouin zone and the S_x, S_y vector field are depicted to illustrate the vortex effect of the Dirac cone.

6.6.3 Few particle dynamics

The method in the previous subsection gives us access, among other things, to the best known experimental observable in condensed matter physics, which is the density of states. It has been the easiest to measure and therefore has become the default choice in optical lattice simulations of solid state physics. However, the distinctive characteristics of the excitations in a half-filled hexagonal lattice may be worth an extra effort: trying to observe the behaviour of a group of particles with well-defined momentum obeying a complete Dirac equation will reveal some of the distinctive features of the simulated fields.

As an example we suggest using the Klein tunneling effect [54] to probe and measure the energy gaps between the two bands. Let us add a uniform electric field pointing along one direction, say x, described by a linearly growing potential, Vx. As explained in Ref. [22], the effect of this potential is to accelerate particles, continuously increasing their momenta in time,

$$k_x(t) = k_x(0) - Vt/\hbar c, \tag{6.42}$$

until the particle reaches a boundary of the Brillouin zone. We have set an adimensional time scale $t = (time) \times J/\hbar$. At this point two things may happen. If the particle is far away from a Dirac singularity, or the minimum gap between energy bands (the effective mass m) is large compared to the acceleration, $mc^2 \gg V$, the particle will simply reappear through the opposite side of the Brillouin zone, reversing its velocity and performing the so called Bloch oscillations. However, if the particle hits against the proximities of the $K_\pm$ points and the gap is small, $mc^2 \ll V$, the particle will experience a Landau-Zener process and jump to the opposite energy band, maintaining its group velocity.

As shown in figure 6.10, we have simulated numerically this process for different masses of the Dirac field. As a signature of the jump between bands we simply use the expectation value of $\vec{k} \cdot \vec{\sigma}$, which is directly correlated to band excitation probability but easier to measure. Note how for the gapless phase, $m = 0$, there is a perfect jump (Figure 6.10a), and how the probability is well approximated by the Landau-Zener formula (Figure 6.10b), which allows us to reverse-engineer the experiment and fit the value of m.

How would this be implemented in an experiment? The idea would be to do the same optical lattice setup with a small number of fermions cooled down to

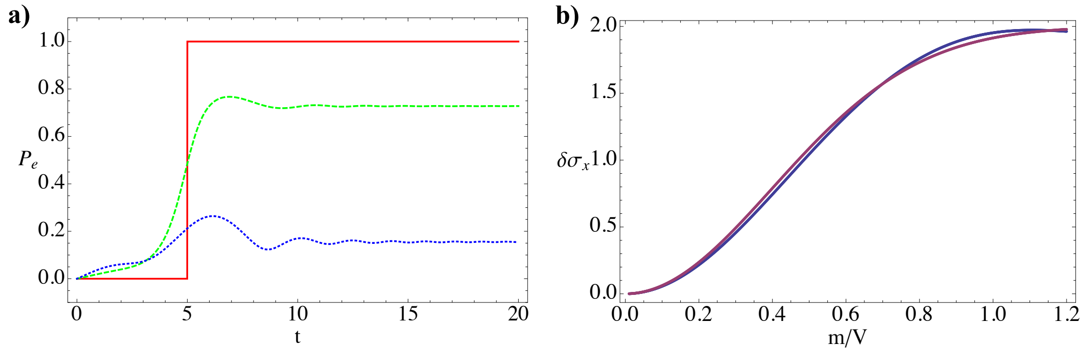

Fig. 6.10: a) Excitation probability for three different ramp speeds V (equation (6.42)): No gap (m=0, solid line), medium gap (m=V, dashed line) and large gap ($m = 2.5V$, dotted line) against time. While the gapless state gets immediately promoted once it reaches the Dirac points, the gapped states have reduced positive energy contributions. b) Change in $\langle\sigma_x\rangle$: $\langle\sigma_x(t=\infty)\rangle - \langle\sigma_x(t=-\infty)\rangle$ depending on the value of the effective mass. We compare the change in $\langle\sigma_x\rangle$ by an exact simulation of the particle dynamics with the Landau-Zener formula (purple). We denote by $t = +(-)\infty$ the times where the particle is still (already) away from the cone.

the lowest value of the momenta, $\vec{k} = 0$, in a honeycomb lattice that implements the desired Dirac Hamiltonian, with or without effective mass. One would then activate an electric field along the direction $\vec{w}$, for a certain time t. After this time one would measure the state of the atoms, or more precisely the expectation value $\langle\vec{\sigma}\rangle$. By changing the duration of the field and its intensity, and monitoring the changes in $\vec{k}\cdot\vec{\sigma}$, one would be able to reconstruct not only the Klein effect but also the whole spin texture of the bands, as discussed in the previous subsection.

6.7 Conclusions

This chapter has presented an experimental proposal to simulate Dirac fermions interacting with an effective gauge field. The fermionic component of the model is obtained by trapping atoms in two triangular optical lattices that are connected to form a honeycomb lattice [84]. The low-energy excitations of such a model have been described using an effective theory that consists of two flavors of non-interacting Dirac fermions. The gauge fields, on the other hand, arise from perturbations of the atom dynamics, such as lattice distortions, short- and long-wavelength modulations of the hopping amplitudes and state-dependent external potentials. Such perturbations are more feasible in the proposed setup, which consists of two independent lattices.

This optical lattice-oriented proposal is in line both with recent developments in the field of graphene [73, 94] and with the field of quantum simulation of synthetic gauge fields [48, 86, 66, 65], but presents various advantages. On the implementation side, the optical lattice setup allows for a single-site resolution and a local customization of the potentials which is hard to think of in solid state implementations. Moreover, the use of two atomic species in a bipartite lattice introduces new measurement possibilities, such as the direct observation of the fermionic fields [See section 6.6.2], or the study of state-dependent Bloch oscillations [Section 6.6.3]. In comparison with other ultracold atom proposals, while this one still relies on the use of assisted tunneling, ours is a static and straightforward setup, where tunneling is implemented by a simple optical field without hopping unitaries, and which nevertheless allows for realistic values of the couplings.

The contents of this chapter are also of purely theoretical interest. The work with optical lattices allows us to make an accurate and rigorous connection between the microscopic theory of trapped atoms and the simulated quantum field theory. While similar work has been done for strained and curved graphene sheets [94], the optical lattice setup allows us to compute from first principles how the microscopic changes in the optical potential lead to "strain" and hopping distortions. In some cases, as in section 6.5.1 a simple modulation of the Raman lasers translates into a similar modulation of the hoppings, giving rise to the gauge fields. In other cases, we may concentrate on geometric deformations of the trapping potential and rigorously work out how they affect the hopping matrices, in a theoretically pleasant and flexible way. We foresee that the same tools here developed will also help solve an open problem in the graphene world, which is the relation between microscopic deformations of the honeycomb lattice and the appearance of an effective metric and curvature. Instead of introducing an effective spin connection by hand, as it is currently done for carbon layers [94], the same metric could be directly derived from deformations of the optical potential. Experimentally, our setup demands the temperature of the atoms to be lower that the typical width of the cone given by the hopping parameters, i.e., $T < J/k \simeq 50\text{nK}$. This low temperatures should be achievable by adiabatically coupling the sublattices, much the reverse of the process highlighted in section 6.6.1.

Finally, it is also remarkable the fact that these models allow for the introduction of on-site and nearest-neighbor atomic interactions at little cost and with realistic values [Section 6.4.3]. At this point the model stops being a single-particle theory and becomes numerically intractable, entering the regime in which quantum simulation provides both new problems and interesting answers.

7. MEASUREMENT OF THE CHERN NUMBER IN TOPOLOGICAL INSULATORS

7.1 Summary

In the previous chapters, we have established a relationship between a mathematical characterization of topological order (the Chern number) and a set of observable operators in the family of pseudospin models. In the simplest case, that in which the Hamiltonian can be decomposed as a commuting sum of 2x2 Hamiltonian terms, these concepts are identical. Here we provide an optical lattice proposal to obtain direct access to the complete set of observables, in order to robustly and unambigously characterize the topological order of your state.

It is important to distinguish that the method here proposed provides a direct signal of the topological order of the *state* itself. The difference vanishes in the proposal made in this chapter, where we assume that our state completely fills an topoligically non-trivial energy band. However, we have seen in Chapter 5 that the measurement of the winding number constitutes a topological invariant in and of itself, regardless the actual dynamics of your system -which, in practice, might be far away from the theoretical model. Indeed, some new results at the time of writing suggest that a non-trivial *model* has been experimentally implemented, much in line with techniques explained in this chapter and the previous one ([90, 51]).

Nonetheless, we will illustrate our measurement method by making a proposal which uses a specific tight-binding model, first suggested by Haldane ([40]). In particular we present a slightly modified version of Haldane's model for a Chern insulator. The modifications we introduce to the model are mainly aimed at increasing the experimental feasibility of the proposal[1]. We calculate the analytical phase diagram and superimpose numerical simulations with realistic atomic parameters, and show excellent agreement. Subsequent works indicate that the model here introduced might be very convenient not only to characterize bulk invariants, but also to probe the dynamics of the edge states which appear ([9]).

We will now outline the structure of this chapter. Finally, we will comment on how time-of-flight measurements in optical lattices are specially suitable to access these non-local bulk observables.

7.2 Presentation of the model

Let us consider a honeycomb lattice constructed out of two triangular sublattices, A and B [Fig. 7.1a]. Each of the sublattices hosts fermionic alkali atoms in a different internal state, $|a\rangle$ and $|b\rangle$. The model is parameterized by four couplings: the hopping amplitudes inside the same species lattice, t_a and t_b, the energy difference between A and B sublattices, ε, and the coupling between sublattices, t_{jk}, which can be induced by a Raman laser and controlled at will [27]. If the lat-

---

[1] The model here introduced presents a richer phenomenology, but the main topological properties -except for an indirect-gap semimetal phase- remain the same. A thorough treatment of the particularities of the model can be found in [32]

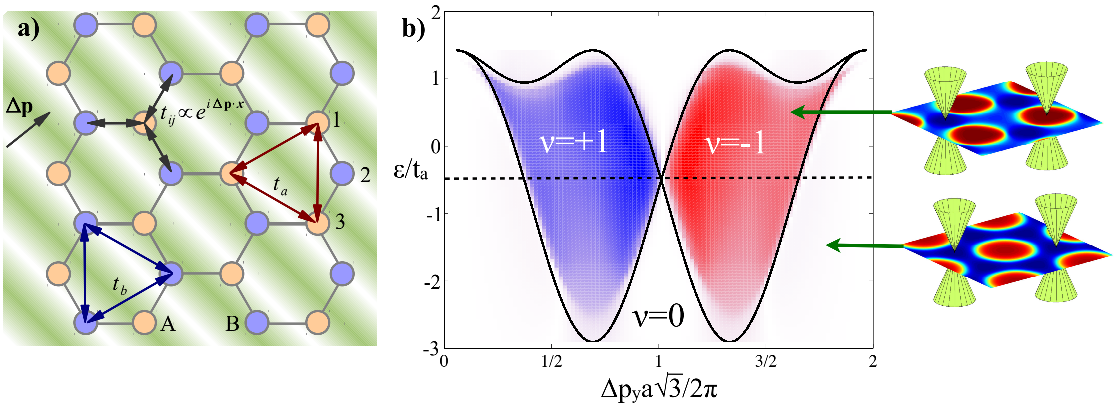

Fig. 7.1: Haldane-type model. (a) Two triangular optical lattices (A and B) are Raman coupled by a laser that makes an atom switch sublattice ($A \leftrightarrow B$). This allows for both next-nearest neighbor hoppings, $t_{a,b}$, and a complex nearest neighbor hopping, t_{jk}, whose phase depends on the momentum imparted by the Raman laser, $\Delta\mathbf{p}$. (b) Phase diagram of the zero-energy ground states, as a function of the energy imbalance between lattices, ε/t_a, and the momentum imparted by the laser, $\Delta\mathbf{p} = (0, \Delta p_y)$. We plot the exact phase boundary in the thermodynamic limit (black solid line), together with a color graded simulation of the Chern number for a finite lattice with $2 \times 17 \times 17$ sites and 20×20 pixels. The diagrams on the right hand side show how the Dirac points are displaced on the distribution of Bloch vectors $S_z(\mathbf{k})$ induced by the Hamiltonian (blue negative, red positive).

tice is deep enough and the tunneling amplitudes and interaction energies remain small compared to the interband separation, we may use single band tight-binding model [2]

$$\begin{aligned} H = & \sum_{\langle a_i, b_j\rangle} (t_{ij} b_i^\dagger a_j + t_{ij}^\star a_i^\dagger b_j) + \sum_j \varepsilon (a_j^\dagger a_j - b_j^\dagger b_j) \\ & + \sum_{\langle\langle a_i, a_j\rangle\rangle} t_a a_i^\dagger a_j + \sum_{\langle\langle b_i, b_j\rangle\rangle} t_b b_i^\dagger b_j. \end{aligned} \tag{7.1}$$

In the presence only of the hopping t_{ij} the energy spectrum consists of two energy bands that meet at two “Dirac points”. At half filling the low energy physics of the system is dominated by the linear dispersion around these points, the “Dirac cones” [84]. Due to the presence of t_a, t_b and ε, the effective Dirac fermions acquire a mass that depends weakly on momentum (see previous chapter). The position of the Dirac points on the mass landscape determines whether the model is topologically ordered or not. In our cold atoms simulation this is controlled using the Raman lasers to attach a phase to the hopping [48]

$$t_{jk} \sim t \exp(i\phi_{jk}), \quad \phi_{jk} = \Delta\mathbf{p} \cdot (\mathbf{x}_j + \mathbf{x}_k)/2. \tag{7.2}$$

---

[2] The neighbor relations are expressed on the honeycomb lattice and the labels i and j run over the unit cell indices. Details about how this Hamiltonian can be experimentally implemented can be found in the previous chapter.

This phase displaces the energy bands created by the Raman hopping, t, relative to mass landscape generated by the other contributions, $t_{a,b}$ and ε, as shown in Fig. 7.1b. When the Dirac points have opposite signs of the mass, the Chern number (8.1) automatically becomes non-zero. Intuitively, while the total flux over each hexagonal plaquette is zero, the bipartite nature of the lattice allows the phases ϕ_{jk} to have a non-trivial effect: along the path $1 \to 2 \to 3 \to 1$, depicted in Fig. 7.1a the local effective magnetic flux, $\phi_{12} + \phi_{23}$, is also different from zero.

The momentum space Hamiltonian associated to (7.1) has the pseudospin structure given in the introduction (see Chapter 4):

$$\mathcal{H}(\mathbf{k}) = \chi(\mathbf{k})\mathbb{1} - E(\mathbf{k})\,\mathbf{S}(\mathbf{k}) \cdot \boldsymbol{\sigma}, \tag{7.3}$$

with two energy bands, $\pm E(\mathbf{k})$, the Pauli matrices $\boldsymbol{\sigma} = (\sigma^x, \sigma^y, \sigma^z)$ and a normalized pseudospin $\mathbf{S}(\mathbf{k})$ labeling the state of the atoms in the $\{|a\rangle, |b\rangle\}$ space. In our model $\mathbf{S}(\mathbf{k}) \propto (t\,\mathrm{Re}f(\mathbf{k} - \boldsymbol{\Delta}\mathbf{p}), t\,\mathrm{Im}f(\mathbf{k} - \boldsymbol{\Delta}\mathbf{p}), \varepsilon + (t_a - t_b)g(\mathbf{k}))$, with the complex functions $f(\mathbf{k}) = \sum_{n=0,1,2} e^{-i\mathbf{k}\cdot\mathbf{v}_n a}$ and $g(\mathbf{k}) = \sum_{n=3,4,5} \cos(\mathbf{k} \cdot \mathbf{v}_n a)$, a set of displacements $\mathbf{v}_i \in \frac{1}{2} \times \{(-2,0), (1,\sqrt{3}), (1,-\sqrt{3}), (0,2\sqrt{3}), (3,\sqrt{3}), (3,-\sqrt{3})\}$ and the honeycomb lattice spacing a. The energy shift $\chi = (t_a + t_b)g$ does not affect the topological phase.

The topological properties of the model can be obtained from the field $\mathbf{S}(\mathbf{k})$. In particular, the lowest energy band has a total Chern number

$$\nu = \frac{1}{4\pi} \int_{\mathcal{B}} \mathbf{S} \cdot \left(\partial_{k_x}\mathbf{S} \times \partial_{k_y}\mathbf{S}\right) d^2k. \tag{7.4}$$

Fig. 7.1b summarizes the three different phases that can be accessed by means of the effective magnetic flux, $\boldsymbol{\Delta}\mathbf{p} = (0, \Delta p_y)$, and the imbalance between lattices, ε/t_a. First of all we find a trivial region, $\nu = 0$, which is topologically equivalent to graphene with a mass term. When we interpret the associated spin texture as a map onto the Bloch sphere, both cones have the same effective Dirac mass and point to the same pole, $S_z > 0$. Since they cover the same polar cap in opposite senses, we have $\nu = \pm(\frac{1}{2} - \frac{1}{2}) = 0$. Moving across the solid black line in Fig. 7.1b, the lattice undergoes a quantum phase transition into a topologically non-trivial phase. Now the cones on inequivalent Dirac points are positioned at opposite poles of the Bloch sphere, forming a skyrmion [Fig. 7.3a] that covers the whole sphere and thus $\nu = \pm(\frac{1}{2} + \frac{1}{2}) = \pm 1$.

7.2.1 Differences with the original Haldane model

The idea of implementing a variation of Haldane's model by using two interpenetrated triangular lattices presents two main advantages: it is one of the ways to implement an imaginary hopping element (another useful option is to shake the lattices, see Refs. [88]) and it allows for independent time-of-flight measurements for each internal level. However, this has some consequences (of little topological

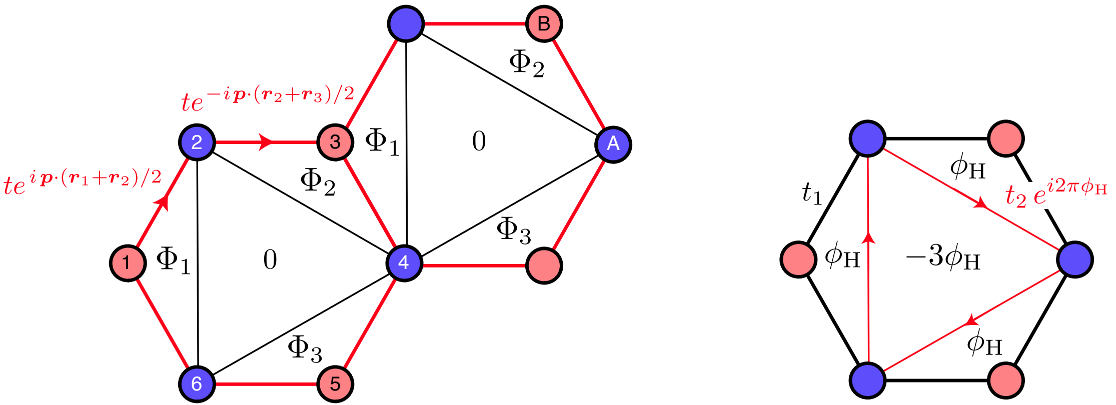

$$\boldsymbol{p} = p_1\boldsymbol{b}_1 + p_2\boldsymbol{b}_2 \longrightarrow \begin{array}{l} \Phi_1 = (p_2 - p_1)/2 \\ \Phi_2 = -\,p_2/2 \\ \Phi_3 = p_1/2 \end{array}$$

Fig. 7.2: *Left*: Pattern of phases arising from Hamiltonian 7.1 in real space, which depend on the choice of the both components of the momentum carried by the Raman beam ($\mathbf{b}_1$ and $\mathbf{b}_2$ are a basis for the reciprocal space vectors). *Right*: Flux configuration in the Haldane model, characterized by a single parameter Φ_H. *Note:* This figure has been taken from Ref. [32]

impact) in the description of the model. For further discussion on the subtleties of the model here introduced, please check Refs. [32] and [9].

The main difference between this model and Haldane's original model ([40]) is that Hamiltonian 7.1 has an imaginary nearest neighbour hopping and real next-to-nearest neighbour hopping whereas Haldane presented a model in which the opposite was true. Moreover, as illustrated in Fig.7.2, the choice of the momentum added by the Raman beam has an extra degree of freedom. While the topological phase diagram is mostly unchanged, an interesting topological semimetal phase may arise due to this extra freedom: in this case, chiral edge states appear even though there is no actual gap in the spectrum (the bands never touch, but the gap is indirectly closed). Again, a more detailed discussion can be found in [32].

7.3 Optical lattice proposal

The setup in Fig. 7.1a may be experimentally realized along the lines of Ref. [5], combining spin-dependent potentials [64, 47], with recent techniques for creating dipole traps using microscope objectives [14]. In line with the techniques explained in the previous chapter, we suggest projecting two triangular lattice patterns on a two-dimensional sheet of light that traps the fermionic atoms. An electro-optic phase modulator controls the relative displacement of the lattices [16] and the appropriate weights of left and right circularly polarized light [64, 47]. The result is two hyperfine ground states of the same fermionic species confined on the two

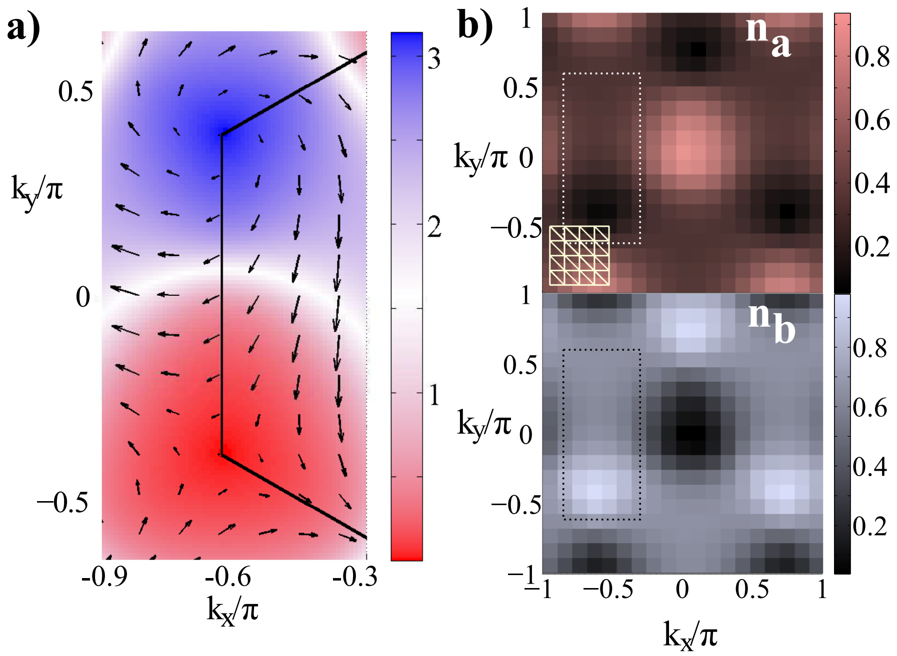

Fig. 7.3: (a) Spin texture of the Haldane model, interpreted as a mapping from momentum space, (k_x, k_y), onto the Bloch sphere, $\mathbf{S} = \langle \boldsymbol{\sigma} \rangle \propto (\cos\phi \sin\theta, \sin\phi \sin\theta, \cos\theta)$. The colors and arrows show the polar angle $\theta(\mathbf{k})$, and the azimutal component of the spin, (S_x, S_y), for a topological phase $\nu = +1$. (b) Interference pictures for this phase which result in momentum density distributions for the a (up) and b (down) particles. A square lattice of 20×20 pixels partitioned into triangles (yellow) is used to compute the estimate $\nu_D = 0.9$ [Eq. (7.5)]. The enclosed area corresponds to (a).

triangular sublattices of the honeycomb pattern. Thanks to this configuration, the distribution $\mathbf{S}(\mathbf{k}) \propto \langle \boldsymbol{\sigma} \rangle$ can be experimentally determined from the TOF images that appear when the atoms are released from the optical trap. A typical experiment would begin with a Mott state in which only the A sublattice is filled, and adiabatically progress to larger values of t_a, t and ε. Once the approximate ground state is prepared, switching off the trap in adequate timescales [56] projects the atom cloud into the momentum density distributions, $n_{a,b}(\mathbf{k})$, giving direct access to one of the pseudospin components $S_z(\mathbf{k}) = \frac{1}{2}[n_a(\mathbf{k}) - n_b(\mathbf{k})]/[n_a(\mathbf{k}) + n_b(\mathbf{k})]$. A fast Raman pulse during TOF allows us to rotate the atomic states and map S_x and S_y to S_z, reconstructing the whole vector field. Actual experiments "pixelize" the time of flight images, counting the number of atoms on each "square" of the effective Brillouin zone and estimating the averages of S_x, S_y or S_z. Either through repetitions or through self-averaging in an experiment with multiple copies of the lattice, we will obtain a set of normalized vectors $\{\mathbf{n}_m\}_{m=1}^{L\times L}$, where $\mathbf{n} = \mathbf{S}/|\mathbf{S}|$, evenly sampled over momentum space. As shown in Fig. 7.3b, we suggest identifying the pixels with the nodes of a triangular lattice, $T = \{\mathbf{n}_{j_T}, \mathbf{n}_{k_T}, \mathbf{n}_{l_T}\}$,

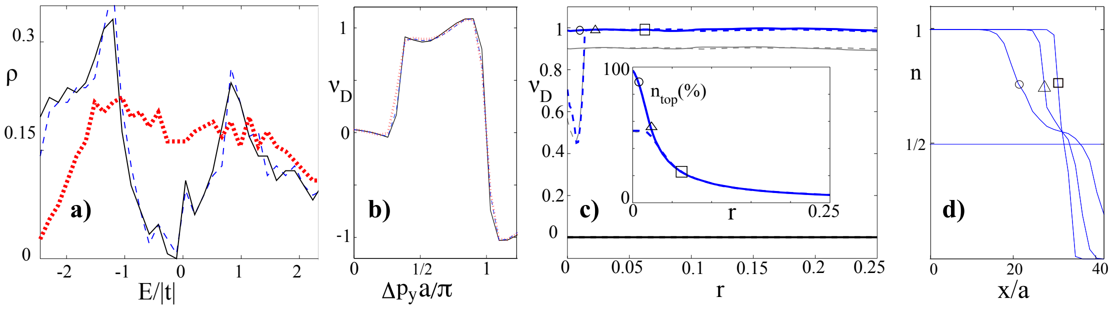

Fig. 7.4: (a) Density of states and (b) Chern number simulation at $\varepsilon/t_a = -0.5$ for a lattice with $r = 0$ (black), 10^{-3} (dashed) and 0.02 (dotted). (c) Chern number for $\varepsilon/t_a = -0.5$ and $p_y = 3\pi/4a$ (blue, above) or $2\pi/a$ (black, below) vs. confining potential strength, r, starting with $1/2$ (solid) or $1/4$ particles per site (dashed) on a lattice with 50×50 sites. The values obtained using 50×50 pixels are compared with those from a 20×20 matrix (gray). (d) Density plots for the points marked in (c), showing the wedding cake structure where regions with $n = 1$ do not contribute to the Chern number.

approximating the integral ν by its discretization[3]

$$\nu_D := \frac{1}{8\pi} \sum_T \mathbf{n}_{j_T} \cdot \mathbf{n}_{k_T} \times \mathbf{n}_{l_T} = \nu + \mathcal{O}(4\pi^2/L^2). \tag{7.5}$$

The value ν_D has the properties of a topological quantity —stability and robustness against local perturbations—, and is also stable with respect to the discretization [30].

We have compared the thermodynamic limit distribution $\mathbf{n}(\mathbf{k})$ with realistic finite-size lattices with imperfections. For this we have exactly diagonalized Eq. (7.1) on a finite lattice with up to 20000 sites, including the additional harmonic confinement term, $\frac{1}{2}m\omega^2 x_i^2$, which is typical from cold atom experiments. Our plots report simulations with $t/\hbar = 1$ kHz, $t_a/t = 0.5$ and $t_b = 0$, using $r = m\omega^2 a^2/2t$ to parameterize the influence of the harmonic confinement. Realistic values for a lattice with $a \sim 400$nm range from $r = 10^{-3}$ (^{6}Li in a trap with $\omega/2\pi = 60$ Hz) to $r = 0.02$ (^{40}K in a trap with $\omega/2\pi = 100$ Hz), but we probed up to $r = 0.25$. The results are very insensitive to the number of atoms, as already for 17×17 sites the interference pattern provides the right phase diagram [Fig. 7.1b]. The Chern number is also very robust with respect to the discretization: a 20×20 pixelization deviates from the theoretical value of ν only 10% [Fig. 7.4b], in line with the error $\mathcal{O}(4\pi^2/L^2)$, expected from a discretization with a smooth integrand. Moreover, ν_D still captures the discontinuity across the topological phase transition [Fig. 7.1b]. Contrary to the global density of states and the eigenenergies, the approximate Chern number ν_D is also robust against inhomogeneities. Already for a confining trap with $r = 0.02$ the Dirac cones are no longer evident [Fig. 7.4a], but

---

[3] A more sophisticated approximation of the integral of the solid angle by a sum can be found in Chapter 9.

the Chern number is still close to ±1 with a good signal-to-noise ratio [Fig. 7.4c]. This is due to the wedding cake structure introduced by the harmonic trap [101]: for sufficiently strong traps there is always one ring or disc hosting n_{top} atoms in a topological phase [Fig. 7.4c-d]. Only these atoms contribute to the total Chern number, much like only superfluid atoms add to the interference peaks in experiments with bosons in optical lattices [29]. Note also how, as shown in Fig. 7.4d, for low densities there are not enough atoms to form a topological phase and the Chern number deviates from ±1. However, raising the trap brings the chemical potential up to a level in which the first disc with particles in a topological phase is created, and ν_D converges to ±1. Finally, we expect also a good behaviour in finite-temperature simulations because the effect of temperature only changes the length of vector $\langle \S \rangle$ (i.e. the signal), but not its orientation.

7.4 Conclusions

Summing up, we have presented a robust and very general method to detect topological order in momentum space using ultracold atoms in various internal states and TOF images. As a very relevant application we have introduced an experimental proposal to implement and sligtly enrichen Haldane's model [40]. The topological phases and our detection method are both robust under (i) use of small finite lattices (ii) coarse grain measurements of the spin texture, (iii) inhomogeneous potentials superimposed on top of the lattice, and (iv) errors in the exact values of the chemical potential, number of atoms or finite temperature. This proposal is thus advantageous with respect to other indirect detection schemes —edge transport, eigenstate preparation [36] or local estimates of the density of states [101]—, which may be more sensitive to temperature and imperfections. Compared also to the numerical protocol in Ref. [79], our method only requires a single set of measurements instead of reconstructing spatially dependent correlators in position space, which are not easily accessible in optical lattices. Finally, the implementation of these ideas would represent a first direct visualization of the topological order of a state.

8. SIGNATURES OF MAJORANA MODES IN OPTICAL LATTICES: CHERN NUMBERS IN TOPOLOGICAL SUPERCONDUCTORS

8.1 Summary

This chapter generalizes the possibility of measuring a topological invariant to a different class of symmetry - a topological superconductor. In this case, the Chern number of the system can also be written in terms of an observable winding number (see Chapter 4), but the different symmetry class analyzed here -as opposed to the previous chapter (chiral to particle-hole, see Chapter 7)- means that the bulk observables should be changed accordingly. The new observables allow us to robustly characterize this kind of topological order in our state.

The most direct consequence of the presence of a non-trivial state in this symmetry class is the emergence of the elusive Majorana zero modes: zero energy quasiparticles that are their own anti-particles [cita]. There has been sustained research for this particles- not least because of their possible applications in topological quantum computation ([69])- but only recently an experiment has (somewhat controvesially) claimed to have found them ([68]) [1]. The robust detection of a non-zero invariant in a topological suprconductor would be an unambigous signature of their presence.

Also in line with the previous chapter, we propose a model specifically tailored to implement this kind of topological order in an optical lattice experiment. The model is adiabatically equivalent to Kitaev's honeycomb lattice model ([53]), and we are therefore able to show that it gives rise to $\nu = \pm 1$ phases, where vortices bind Majorana fermions, and to $\nu = \pm 2$ phases that emerge as the unique collective state of such vortices. However, the version presented here is meant to increase drastically its experimental feasibility, and an analysis of the realistic experimental parameters is also provided. (necessity of a new test model / cite other proposals)

The most challenging aspect of the experimental proposal lies in the implementation of a BCS-like pairing term between fermions, since p-wave pairing between neutral atoms is too weak in any reasonable tight-binding setup. Our proposed model only requires experimental accessible s-wave pairing, while an additional superlattice engineers the staggered tunnelling pattern that mimics the necessary spin-orbit coupling. However, this added degree of freedom breaks the pseudospin nature of our model, making it a challenge to connect the actual observables with the true Chern number of the state (in fact - and restricting ourselves to the theory that has been laid in the previous chapters - the computation of the Chern number through an observable map on the Brillouin zone is not challenging, but impossible). Fortunately, this change sets up the perfect scenario for applying the theory developed in Chapter 5, where we compute *two* separate invariants and use them to compute both the Chern number and the entanglement between sublattice partitions.

The rest of the chapter is structured as follows: First, we briefly review the theoretical tools for measuring topological order in composite systems, as outlined

---

[1] The controversy is a consequence of the indirect detection methods which are widely used in solid state systems. The signature provided in this chapter is, in this sense, definitive.

in chapters 4 and 5 We include a brief subsection which provides a much simpler, ambiguous phase measurement based on the symmetries of the problem. We then build a model which presents a rich topological phase diagram, which we solve and prove to be equivalent to Kitaev's model. We numerically show that the winding number measurements are robust against a variety of perturbations. Finally, we make an experimental proposal in an optical lattice, and provide quantitative details about its feasibility.

8.2 Chern number as an observable in topological superconductors

In this section we review how the Chern number of a translationally invariant topological superconductor can be computed as a physically observable winding number, and how In addition to the detection of the full Chern number, we will also show that its parity can be obtained from experimentally accessible density measurements. While not providing full characterization, this provides a simple method to distinguish between phases which can and can not support Majorana modes.

8.2.1 The Chern as a winding number in a spinless system

Formally, the Chern number, ν, can be defined as the winding number of the projector onto the ground state [91]. When the Bogoliubov-de Gennes Hamiltonian is a 2×2 matrix, i.e. the system is fully translationally invariant, it can always be written as $H(p) \propto \mathbf{S}(p) \cdot \vec{\sigma}$ for some vector field $\mathbf{S}(p)$. Here $\vec{\sigma}$ denotes a vector of Pauli matrices. The Chern number, ν, is then equivalent to the winding number

$$\tilde{\nu}[\mathbf{S}] = \frac{1}{4\pi} \int_{BZ} \mathbf{n}(p) \cdot \left(\frac{\partial \mathbf{n}(p)}{\partial p_x} \times \frac{\partial \mathbf{n}(p)}{\partial p_y} \right) \mathrm{d}^2 p \in \mathbb{Z}, \tag{8.1}$$

which counts how many times the normalised vector $\mathbf{n} = \mathbf{S}/|\mathbf{S}|$ winds around the Bloch sphere in the particle-hole space as one spans the whole Brillouin zone [91]. We can evaluate this quantity if we know the components of the vector field $\mathbf{S}(p)$. These components are observables that can be obtained as the ground state expectation values

$$\mathbf{S}(\mathbf{p}) = \langle \psi | \hat{\boldsymbol{S}}_p | \psi \rangle , \qquad \hat{\boldsymbol{S}} = \frac{1}{2} \hat{\Psi}^\dagger_{\mathbf{p}} \vec{\sigma} \hat{\Psi}_{\mathbf{p}}, \tag{8.2}$$

with the physical observables $\hat{\boldsymbol{S}}_p$ being given in the basis $\hat{\Psi}^\dagger_{\mathbf{p}} = (\hat{a}^\dagger_p, \hat{a}_{-p})$ of the BdG Hamiltonian $H(p)$:

$$\begin{aligned} \hat{S}^x_p &= \hat{a}^\dagger_p \hat{a}^\dagger_{-p} + \hat{a}_{-p} \hat{a}_p, \\ \hat{S}^y_p &= -i \hat{a}^\dagger_p \hat{a}^\dagger_{-p} + i \hat{a}_{-p} \hat{a}_p, \\ \hat{S}^z_p &= \hat{a}^\dagger_p \hat{a}_p - \hat{a}_{-p} \hat{a}^\dagger_{-p}. \end{aligned} \tag{8.3}$$

This set of observables are a basis for the single pseudospin Hamiltonian and constitute a natural extension of the operators which construct the winding number in the case of topological insulators [6].

While S^z is experimentally readily obtained from density measurements $\hat{S}^z_p$, the experimental measurement of the operators $\hat{S}^x_p$ and $\hat{S}^y_p$ is challenging, since they violate a superselection rule: the number of particles. However, one can in general go around this by mapping them to experimentally accessible operator $\hat{S}^z_p$ with suitable rotations on the state. This can typically be achieved by using operators present in the Hamiltonian (such as $\hat{S}^{x,y}_p$ themselves). We will later illustrate with a particular example how this could be performed in an optical lattice experiment.

8.2.2 Winding numbers for the multi-component case

To generalise the construction of the Chern number as a physically observable winding number to a system with m-site unit cell (or more generally, m degrees of freedom giving 2^m dimensional Hilbert space per unit cell), we define an independent vector field $\mathbf{S}_{(i)}(p) = \langle\psi| \hat{\boldsymbol{S}}_{(i),p} |\psi\rangle$ for each of the sublattices, $i = 1, \dots, m$. We can then apply the full theoretical body of Chapter5, which shows that the Chern number can be expressed as a sum of the subsystem winding numbers computed through the aforementioned independent vector fields:

$$\tilde{\nu} = \sum_{i=1}^{m} \tilde{\nu}_{(i)}. \tag{8.4}$$

We note that for this decomposition to make sense, we assumed that the vectors $\mathbf{S}_{(i)}$ can be robustly determined, i.e. that they have a finite norm. This requirement thus provides a physical constraint for the detection of the Chern number: The Chern number is reproduced as the sum of the sublattice winding numbers only when the sublattices are not maximally entagled (as explained in chapter 5). As the entanglement given by the norm $|\mathbf{S}_{(i)}|$ is also a physical observable, it can be used in the experiments as a measure of reliability of the characterization provided by the winding number 8.4. We will numerically verify in the we present next that the decomposition indeed fails only in the maximal entanglement limit.

8.2.3 Chern number parity from density measurements

While the Chern number can be obtained by using the full set of observables, for practical purposes a coarser classification of the phases can be sufficient. For instance, to distinguish between phases that support localized Majorana modes (odd ν) from those that do not (even ν), it is sufficient to know only the parity of the Chern number. Or to classify all the topological phases up to their chiralities, the knowledge of $|\nu|$ is sufficient. Remarkably, both can be obtained from $\Sigma^z_{(i)}$ measurements that are directly experimentally accessible.

Let us consider first the properties of the spinless case. Due to the presence of both translational and particle-hole symmetries the surface $\mathbf{S}(p)$ has always the topology of a torus and it is always symmetric around the z-axis. This means that by just counting the extremal and saddle points of the $S^z(\mathbf{p})$, we can infer whether the surface $\mathbf{S}(p)$ encloses the origin or not. The key observation is that $\tilde{\nu} \neq 0$ is possible only if it does. The parity of the winding number $|\nu| (\mathrm{mod}\, 2)$ can thus be obtained using the following simple protocol: (i) Find the null-gradient-points (local maxima and minima and saddle points) of the S^z distribution in the Brillouin zone, and (ii) assign $|\tilde{\nu}| = 0(1)$ if the number of such points with $S^z > 0$ is even (odd). Phases with $|\nu| = 0(1)$ will correspond to phases with even (odd) Chern numbers.

In a system with m components one has m winding numbers $\tilde{\nu}_{(i)}[\mathbf{S}_{(i)}]$ whose parities can be independently obtained using the same protocal as above. This allows for a richer characterization of the phases beyond just the Chern number parity. In fact, when we apply in the next section the parity measurements to a particular example, we find that the absolute value of the Chern number can be consistently obtained as the sum of the sublattice winding parities, i.e. that $|\nu| = \sum_i |\tilde{\nu}_{(i)}|$. We postulate that this is a general property, which allows for the full characterization of different types of topological phases in multi-component systems based on the experimentally accessible density measurements only.

8.3 A case study model: Staggered spinless fermions with s-wave pairing

In this section we demonstrate our detection scheme for the Chern number in the context of a particular model. First we introduce a model of staggered spinless fermions whose phase diagram contains topological phases characterized by Chern numbers $\nu = 0, \pm 1$ and ± 2. We show its adiabatic connection to Kitaev's honeycomb model and the way this connection allows the model to exhibit collective signatures of Majorana modes. We then demonstrate that the phase diagram of the model can be robustly captured using the detection methods described in Section II.

Our model is defined for spinless fermions on a square lattice and combines staggered complex hopping with a uniform superconducting s-wave interaction. The Hamiltonian is

$$\begin{aligned} H &= \sum_{\mathbf{j}} \Big[\mu_{\mathbf{j}} a_{\mathbf{j}}^\dagger a_{\mathbf{j}} + it(-1)^{j_x} a_{\mathbf{j}}^\dagger a_{\mathbf{j}+\hat{\mathbf{x}}} + t a_{\mathbf{j}}^\dagger a_{\mathbf{j}+\hat{\mathbf{y}}} \\ &\qquad + \Delta \big(a_{\mathbf{j}}^\dagger a_{\mathbf{j}+\hat{\mathbf{x}}}^\dagger + a_{\mathbf{j}}^\dagger a_{\mathbf{j}+\hat{\mathbf{y}}}^\dagger \big) \Big] + \mathrm{H.c.}, \end{aligned} \tag{8.5}$$

where $a_{\mathbf{j}}^\dagger$ creates a fermion at site $\mathbf{j} = (j_x, j_y)$, the tunnelling amplitude t and the pairing potential Δ are both real and the chemical potential $\mu_{\mathbf{j}} = \mu + (-1)^{j_x}\delta$

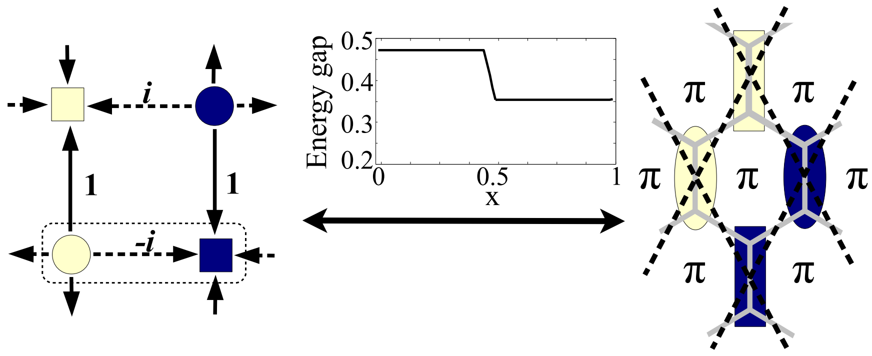

Fig. 8.1: *Left:* Staggered topological superconductor with s-wave pairing on a square lattice 8.5. The numbers denote the relative phases of the tunnelling amplitudes, while the black (white) sites experience a chemical potential $\mu_b = \mu + \delta$ ($\mu_w = \mu - \delta$). Circles and squares denote the underlying distinct, but fixed internal atomic states that facilitate the optical lattice implementation. The dashed box denotes the two site "magnetic" unit cell. *Right:* When Kitaev's honeycomb model with π-flux vortex per plaquette is written in the basis of complex fermions, the vertical links become the sites of a square lattice, with the fermions subject to a staggered chemical potential. As detailed below, a linear interpolation $xH + (x-1)H_{\text{HC}}$ for $x \in [0,1]$ shows that our model 8.5 can be adiabatically connected to the honeycomb model with Hamiltonian H_{HC}.

is staggered by the detuning δ. Translational symmetry is broken along the x-direction with the "magnetic" unit cell consisting of two adjacent sites with detuned chemical potentials, as shown in Fig. 8.1. Inspired by the Kogut-Susskind fermions [89, 65] we interpret this lattice degree of freedom as a "pseudospin" $\tau \in \{b, w\}$ of the fermions $a^\dagger_{\tau,\mathbf{j}}$. The Hamiltonian 8.5 can thus be viewed as an effective pseudospin-orbit coupled system: Tunnelling along the $x(y)$-direction changes (conserves) the pseudospin state, which effectively realises an anisotropic Rashba type spin-orbit coupling, while the chemical potential detuning plays the role of a Zeeman term. Thus, by adding s-wave pairing, one expects to find Majorana mode supporting topological phases [7].

To verify this, we will solve Eq.8.5 by Fourier transforming it with respect to the magnetic unit cell. From the analytic solution presented below, we obtain the phase diagram shown in Fig. 8.5. We find that by varying only the chemical potentials we can move between a variety of extended topological phases with Chern numbers $\nu = 0, \pm 1$ and ± 2.

8.3.1 Analytic solution

The Hamiltonian 8.5 can be Fourier transformed with respect to the two site unit cell illustrated in Fig. 8.1. Writing it in the particle-hole basis $\psi^\dagger_p = (a^\dagger_{b,p}, a^\dagger_{w,p}, a_{b,-p}, a_{w,-p})$, we obtain the quadratic Bogoliubov-de Gennes Hamiltonian $H = \int_{BZ} \psi^\dagger_p H(p) \psi_p \mathrm{d}^2 p$, where

$$H(\mathbf{p}) = \begin{pmatrix} f_+ & ig_+^* & ih & g_-^* \\ -ig_+ & f_- & -g_- & ih \\ -ih & -g_-^* & -f_+ & ig_+^* \\ g_- & -ih & -ig_+ & -f_- \end{pmatrix}, \tag{8.6}$$

with

$$\begin{array}{rcl} f_pm & = & (\mu \pm \delta) + 2t\cos(p_y), \\ g_+ & = & t(1 + e^{2ip_x}), \\ g_- & = & \Delta(1 - e^{2ip_x}), \\ h & = & 2\Delta\sin(p_y). \end{array}$$

The Hamiltonian can be diagonalised with a Bogoliubov transformation, which gives the four particle-hole symmetric energy bands

$$E_n^{\pm}(p) = \pm\sqrt{A(p) + (-1)^n\sqrt{A^2(p) - 4B(p)}}, \tag{8.7}$$

where

$$\begin{array}{rcl} A(p) & = & f_+^2 + f_-^2 + 4\left(|g_+|^2 + h^2 + |g_-|^2\right), \\ B(p) & = & |g_+|^4 + h^4 + |g_-|^4 + f_+^2 f_-^2 + \\ & & h^2(f_+^2 + f_-^2) - 2f_+f_-(|g_+|^2 - |g_-|^2) - \\ & & 2h^2(|g_+|^2 + |g_-|^2) - 2\mathrm{Re}(g_-g_+^*)^2. \end{array}$$

The particle-hole symmetry is represented by $C = \sigma^x \otimes \mathbb{1}$ that swaps the creation and annihilation operators of opposite momenta. It acts on 8.6 as

$$CH(p)C^{-1} = -H^*(-p), \tag{8.8}$$

which implies that zero energy eigenstates at the momenta $p = (0,0), (0,\pi)$ will be self-conjugate. Fig. 8.2 shows that in the $\nu = 1$ and $\nu = 2$ phases the edge states indeed cross zero energy at these momenta, implying that they are (dispersing) Majorana modes. In the presence of a vortex (a puncture in the plane with π-flux through it), they will thus become localised at the vortex cores [24]. Odd number of edge states (odd ν) implies that an isolated Majorana mode will always remain localised at zero energy at the vortex core, while an even number of them (even ν) leads to complete hybridisation with all the Majorana modes pairing up to localised Dirac fermions. In the $\nu = 0$ phases no edge states cross zero energy (although high energy edge states can still exist as shown in Fig. 8.2), and vortices will not bind localised low-energy states of either Majorana or Dirac type.

8.3.2 Adiabatic connection to Kitaev's honeycomb model

We now proceed to show that our model is adiabatically connected to Kitaev's honeycomb model [53]. This connection, which is schematically illustrated in Fig. 8.1, enables us immediately to understand some of the features of the phase diagram of our model.

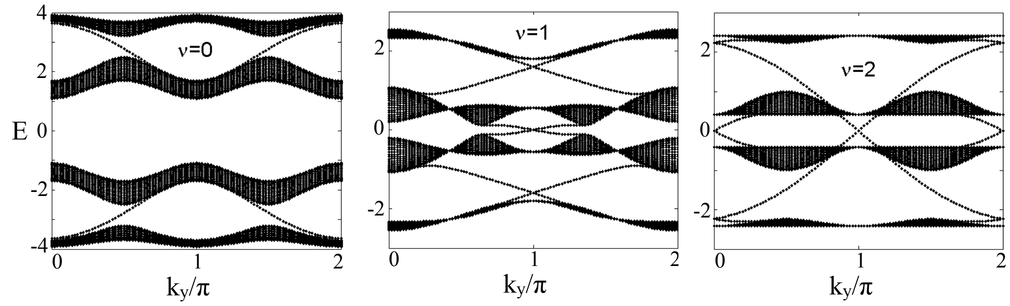

Fig. 8.2: Edge states in the different topological phases. The spectral flow on a cylinder (open boundary conditions in x-direction) for the (a) $\nu = 0$ $[(\delta, \mu) = (5, 0)]$, (b) $\nu = 1$ $[(\delta, \mu) = (5, 2)]$ and (c) $\nu = 2$ $[(\delta, \mu) = (2, 0)]$ phases shows $|\nu|$ edge states per edge crossing zero energy. The plots are for $t = \Delta = 1$.

In particular, Kitaev's model is known to support localised Majorana modes with short-range interactions [57]. We show this explicitly for the $\nu = 2$ phase, which we connect to the $\nu = 2$ phase arising in the full-vortex sector as the unique collective state of the Majorana modes bound at the vortex cores [59, 58].

In nutshell, the honeycomb model is a local spin lattice model that contains nearest-neighbour two-spin interactions (of magnitudes J_x, J_y and J_z depending on link orientations) and next-nearest-neighbour three-spin interactions (of magnitude K) that break time-reversal symmetry. When mapped to a tight-binding model of free Majorana fermions on the honeycomb lattice, the spin interactions map into nearest and next nearest neighbour tunnelling, respectively. The model becomes exactly solvable when restricted to a particular symmetry sector that corresponds to some background pattern of π-flux vortices. [53]

We are interested in the full-vortex sector (π-flux on each hexagonal plaquette), which supports topological phases with Chern numbers $\nu = 0, \pm 1$ and ± 2 [59]. When the honeycomb model is restricted to it, the tight binding Hamiltonian can be written as:

$$\begin{aligned} H_{\text{f.v.}} = & \; i \sum_{\mathbf{j}} \left[(-1)^{j_x} J_z a_{\mathbf{j}} b_{\mathbf{j}} + J_x a_{\mathbf{j}} b_{\mathbf{j}+\hat{\mathbf{x}}} + J_y a_{\mathbf{j}} b_{\mathbf{j}+\hat{\mathbf{y}}} \right] \\ & + iK \sum_{\mathbf{j}} (-1)^{j_x} \left[a_{\mathbf{j}} a_{\mathbf{j}-\hat{\mathbf{x}}} + a_{\mathbf{j}} a_{\mathbf{j}+\hat{\mathbf{y}}} + b_{\mathbf{j}} b_{\mathbf{j}+\hat{\mathbf{x}}} + b_{\mathbf{j}} b_{\mathbf{j}-\hat{\mathbf{y}}} \right], \end{aligned} \tag{8.9}$$

where $a_{\mathbf{j}}^\dagger = a_{\mathbf{j}}$ and $b_{\mathbf{j}}^\dagger = b_{\mathbf{j}}$ are Majorana operators on the two triangular sublattices of the honeycomb lattice. To simplify the demonstration of the adiabatic connection, we have included only four out of the six possible next nearest neighbour hoppings, as illustrated in Fig. 8.3. The omitted terms are $a_{\mathbf{j}} a_{\mathbf{j}+\hat{\mathbf{x}}+\hat{\mathbf{y}}}$ and $b_{\mathbf{j}} b_{\mathbf{j}+\hat{\mathbf{x}}+\hat{\mathbf{y}}}$, that have been shown to be adiabatically tuneable to zero while staying in the same phase [99].

The full-vortex sector is encoded in the $(-1)^{j_x}$ factors that stagger the signs of the Majorana hopping amplitudes J_z and K. Pairing the Majorana operators

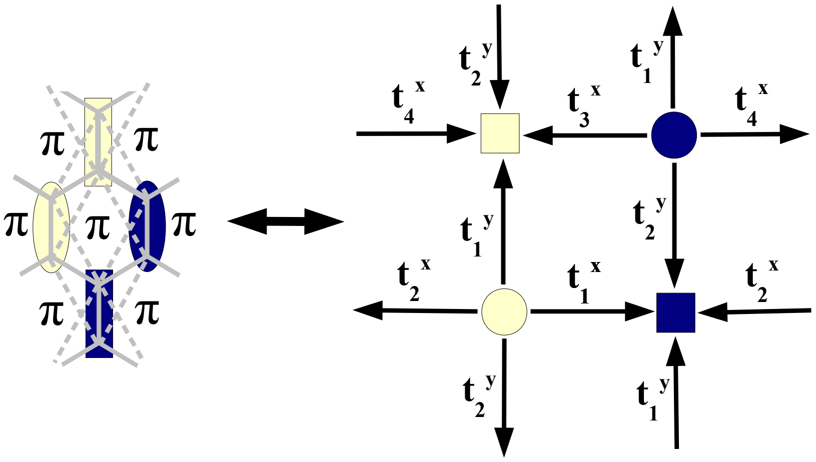

Fig. 8.3: *Left:* The honeycomb model 8.9 with a π-flux on every plaquette. When mapped into a tight-binding model of Majorana fermions, the nearest neighbour hopping is along the solid links (of magnitude J_z along the vertical links and J_x or J_y along the other two oriented links) and the included next-nearest-neighbour hopping along the dashed ones (of uniform magnitude K). The vortex lattice is encoded in the staggered signs of the J_z hopping[59]. When the Majorana fermions are paired into complex fermions, the vertical links become the sites of a square lattice, with J_z translating into sign staggered chemical potential. *Right:* When the tunnelling couplings $t^x_{\mathbf{j}}$ and $t^y_{\mathbf{j}}$ in 8.12 are explicitly written out, one finds six independent couplings, which we denote as $t^x_1, t^x_2, t^x_3, t^x_4, t^y_1$ and t^y_2. Redefining the operators on the circle (square) sites by $c_{\mathbf{j}} \to e^{i\chi}c_{\mathbf{j}}(c_{\mathbf{j}} \to e^{-i\chi}c_{\mathbf{j}})$ preserves the real pairing potential for arbitrary χ, while unitarily transforming the hopping amplitudes. For $\chi = \phi/2 - \pi/4$ they are brought to the form 8.13.

into complex fermions $c_{\mathbf{j}}$ by

$$a_{\mathbf{j}} = e^{i\theta_{\mathbf{j}}}c_{\mathbf{j}} + e^{-i\theta_{\mathbf{j}}}c^\dagger_{\mathbf{j}}, \qquad b_{\mathbf{j}} = \frac{1}{i}(e^{i\theta_{\mathbf{j}}}c_{\mathbf{j}} - e^{-i\theta_{\mathbf{j}}}c^\dagger_{\mathbf{j}}), \tag{8.10}$$

the phase $\theta_{\mathbf{j}}$ to be defined below, the vertical links with couplings J_z connecting the $a_{\mathbf{j}}$ and $b_{\mathbf{j}}$ sites of the honeycomb lattice become the sites of a square lattice, as illustrated in Fig. 8.3. The Hamiltonian takes the form

$$\begin{aligned} H_{\text{f.v.}} &= \sum_{\mathbf{j}} \big[\mu_{\mathbf{j}} c^\dagger_{\mathbf{j}} c_{\mathbf{j}} + t^x_{\mathbf{j}} c^\dagger_{\mathbf{j}} c_{\mathbf{j}+\hat{\mathbf{x}}} + t^y_{\mathbf{j}} c^\dagger_{\mathbf{j}} c_{\mathbf{j}+\hat{\mathbf{y}}} \\ &\qquad \Delta_x c_{\mathbf{j}} c_{\mathbf{j}+\hat{\mathbf{x}}} + \Delta_y c_{\mathbf{j}} c_{\mathbf{j}+\hat{\mathbf{y}}}\big] + \text{H.c.}, \end{aligned} \tag{8.11}$$

where we have defined

$$\begin{aligned} \mu_{\mathbf{j}} &= 2J_z(-1)^{j_x} \\ t^x_{\mathbf{j}} &= re^{i(-1)^{j_x}(2-(-1)^{j_y})\phi}, \\ t^y_{\mathbf{j}} &= 2Je^{-i(-1)^{j_x+j_y}\phi}, \\ \Delta_x &= 2J, \\ \Delta_y &= r, \end{aligned} \tag{8.12}$$

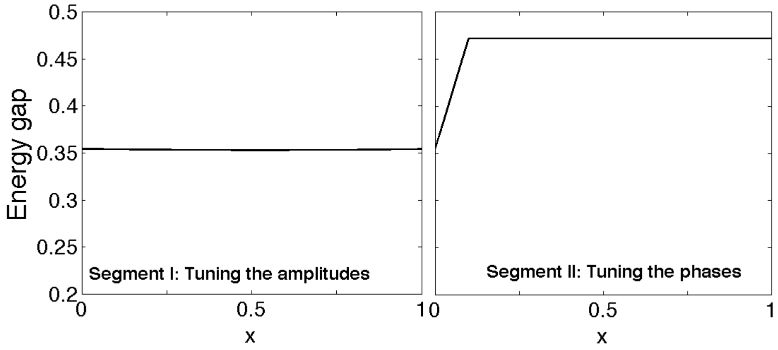

Fig. 8.4: Adiabatic connection between the $\nu = 2$ phases in the full-vortex sector of the honeycomb model and in 8.5. We set $J_z = J = 1$ and $K = -0.1$, which through the identifications 8.12 give the chemical potential $\delta = 2$, $\mu = 0$, while for the coupling amplitudes we get $\Delta_x = |t_j^y| = 2$ and $\Delta_y = |t_j^x| = \sqrt{4.16} \approx 2.04$. *Left:* In the first segment of the adiabatic path we tune $t = \Delta_y = |t_j^x| \to \Delta_x = |t_j^y|$ to equalise all the amplitudes. The plot shows the energy gap of $H_{\text{f.v.}}[t(x)]$, where $t(x) = (1-x)\sqrt{4.16} + 2x$, increasing monotonously during the process. *Right:* At the second step we tune the tunnelling phase $\phi = \arctan(5) \to \pi/4$. The plot shows the energy gap of $H_{\text{f.v.}}[\phi(x)]$, where $\phi(x) = (1-x)\arctan(5) + x\frac{\pi}{4}$, again first increasing and then settling to a constant value. Both transitions are performed with a linear ramp parameterised by $x \in [0,1]$.

with $J = J_x = J_y$, $r = \sqrt{(2J)^2 + (4K)^2}$ and $\phi = \arctan(J/(2K))$. In terms of these variables the local phase $\theta_\mathbf{j}$ in 8.10, that is chosen such that the pairing potentials Δ_x and Δ_y are real, is given by $\theta_\mathbf{j} = -(-1)^{j_x}\frac{1-(-1)^{j_y}}{2}\phi$.

The variables $t_\mathbf{j}^x$, $t_\mathbf{j}^y$, r and ϕ are all functions of the honeycomb couplings J, J_z and K. From now on we will treat them as independent variables and show that Hamiltonian 8.11 can be adiabatically connected to Hamiltonian 8.5. We do this by explicitly constructing a path in the parameter space along which the energy gap remains finite. Due to the periodically alternating signs in the chemical potential $\mu_\mathbf{j}$, we begin with identifying the detuning δ with $2J_z$, where the overall chemical potential is set to $\mu = 0$. The first segment of the adiabatic path consists of tuning $r \to 2J \equiv t$, which makes both the tunnelling and pairing amplitudes equal ($|t_\mathbf{j}^x| = |t_\mathbf{j}^y| = \Delta_x = \Delta_y = t$). Fig. 8.4 shows the gap essentially remaining constant during this process.

At the second segment we tune the phases of $t_\mathbf{j}^x$ and $t_\mathbf{j}^y$ to match those of 8.5. Writing out the tunnelling terms explicitly, we find the periodic pattern to consist

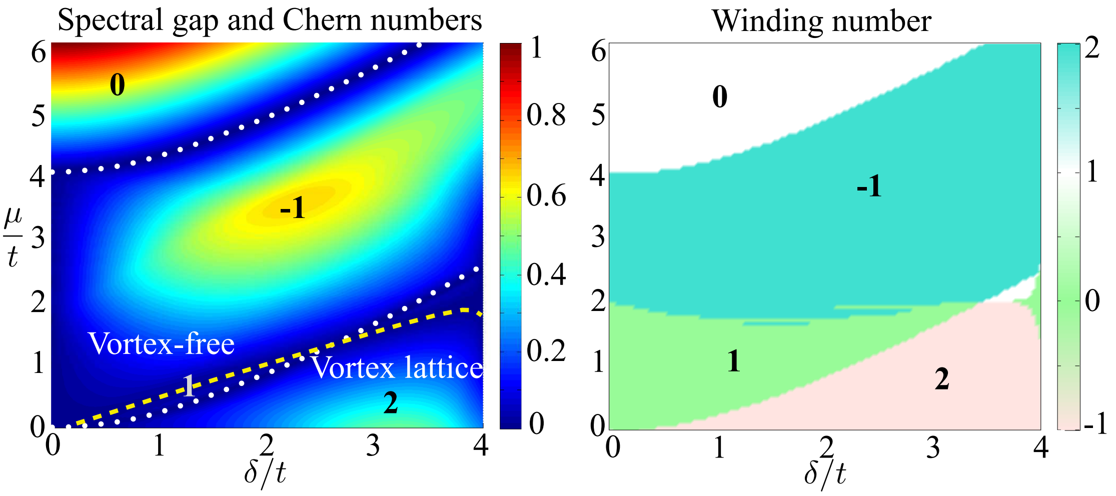

Fig. 8.5: *Left:* The phase diagram of Ham.8.5 as a function of the overall chemical potential μ and its detuning δ. Colour encodes the magnitude of the fermionic spectral gap, the dashed lines show the phase boundaries at which the gap closes. The Chern number ν for each phase is also shown. The phase diagram is symmetric with respect to $\mu \to -\mu$, while for $\delta \to -\delta$ all the Chern numbers become time reversed ($\nu \to -\nu$). The regions $\mu \lesssim \delta/2$ ($\mu \gtrsim \delta/2$) can be identified with Kitaev's honeycomb model in the presence (absence) of a vortex lattice. *Right:* The total winding number $\tilde{\nu}$, as defined in Eq. 8.4, (encoded in colour). It shows perfect agreement with the Chern number except in regions where sublattices are close to being maximally entangled (see Fig. 8.6). Both plots are for $\Delta/t = 2$.

of six independent ones, which are unitarily equivalent to

$$\begin{array}{rcll} t_1^x & = & te^{i\pi/2} & \to \; it, \\ t_2^x & = & te^{-i\pi/2} & \to \; -it, \\ t_3^x & = & te^{4i\phi-i\pi/2} & \to \; it, \\ t_4^x & = & te^{-4i\phi+i\pi/2} & \to \; -it, \\ t_1^y & = & te^{-2i\phi+i\pi/2} & \to \; t, \\ t_2^y & = & te^{2i\phi-i\pi/2} & \to \; t, \end{array} \tag{8.13}$$

as illustrated in Fig. 8.3. The arrow denotes the second segment of the adiabatic path where we tune $\phi \to \pi/4$ to make the tunnelling phases match those of 8.5. Fig. 8.4 shows the gap remaining again robust, which implies that our staggered model of spinless fermions is adiabatically connected to Kitaev's honeycomb model in the full-vortex sector. Indeed, for equal couplings $J = J_z = 1$ and $K < 0$ the honeycomb model is known to be in a $\nu = 2$ phase [59, 58]. These honeycomb couplings correspond to $t = \Delta_x = \Delta_y = \delta = 2$ and $\mu = 0$ for which, as shown in Fig. 8.5, we also find a $\nu = 2$ phase.

The phase diagram of the full-vortex sector of the honeycomb model has been studied in [59]. The adiabatic connection between the models enables us to understand some of the features of the phase diagram of our model. First, we showed

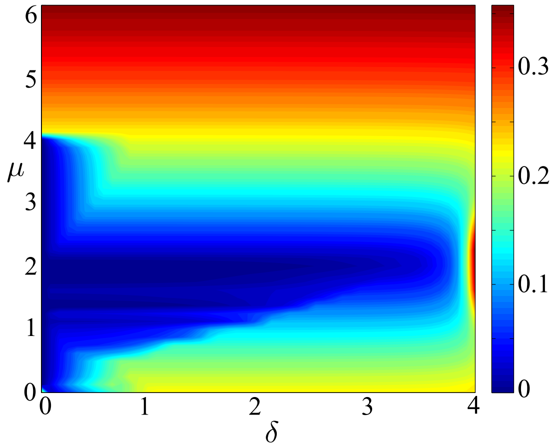

Fig. 8.6: The sublattice entanglement, as characterized by the minimum value $\min_{\mathbf{p}} |\mathbf{S}_{b/w}(p)|$, as functions of μ and δ. Comparison to Fig. 8.5 shows that the winding number $\tilde{\nu}$ reproduces the Chern number everywhere except where the sublattices are close to being maximally entangled ($\min_{\mathbf{p}} |\mathbf{S}_{b/w}(p)| \lesssim 0.1$). In these regimes numerical errors due the momentum space coarse graining become significant as $|\mathbf{S}_{b/w}(p)|$ becomes very small.

above that the full-vortex sector with equal couplings $|J_x| = |J_y| = |J_z|$ can be mapped onto the $\mu = 0$, $\delta > 0$ line of Fig. 8.5. Thus we can immediately understand the $\nu = 2$ phase to correspond to the $\nu = 2$ phase in the honeycomb model that is known to arise as the unique collective state of the Majorana modes bound to the vortex cores. When the staggering $\delta = 2J_z$ of the hopping in 8.9 is gradually suppressed by introducing a finite μ by hand, it has been shown that for $\mu \gtrsim \delta/2$ the non-Abelian $\nu = 1$ phase is recovered, even if some sign staggering remains. This is in agreement with Fig. 8.5, which shows along the $\mu \approx \delta/2$ line a similar transition between the Abelian $\nu = 2$ and the non-Abelian $\nu = -1$ phases (the change in the sign of the Chern number does not occur in the honeycomb model, but due to adiabatic deformation we expect only qualitatively similar behaviour in our model). The $\mu > \delta/2$ region of our model is thus adiabatically connected to the non-Abelian phase in the vortex-free sector (which in turn is adiabatically connected to the weak-pairing phase of a p-wave superconductor [99]). Finally, in the dimerised limits $|J_z| \gg |J|$ one should always find a $\nu = 0$ phase, that corresponds to the strong pairing phase in p-wave superconductors. Indeed, Fig. 8.5 shows a $\nu = 0$ phase emerging in both $\delta \gg \mu$ and $\mu \gg \delta$ limits.

8.3.3 Measuring the phase diagram through observables

Fig. 8.5 shows the comparison between the Chern numbers calculated from the ground state and the winding number (Eq.8.4) calculated from the observables (Eq.8.3) particularized for the black and white sublattices. In general, we find excellent agreement between the two invariants. The only discrepancies occur

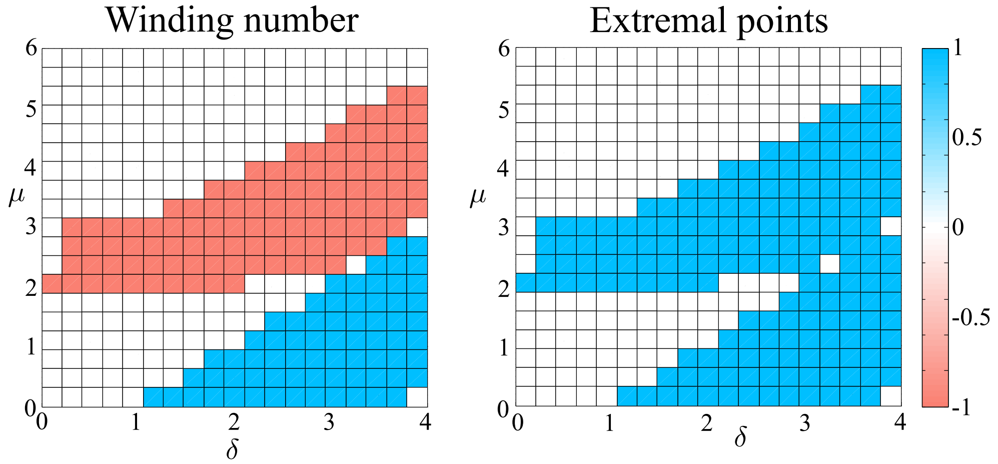

Fig. 8.7: Comparison between the winding number $\tilde{\nu}_{(w)}$ (left) and its parity as computed from the null-gradient-points of S^z_w (right). The parity is in perfect agreement across the phase diagram. The simulation is performed on 20×10 lattice sites.

in regions where the spectral gap is small. As anticipated in Section II.B, we can attribute this to the sublattices becoming close to maximally entanglement. Fig. 8.6 shows that in regimes where the norm $|\mathbf{S}_{b/w}|$ becomes small, thus causing numerical errors due to momentum space coarse graining. So only $|\nu|$ may be captured (which however is still sufficient to characterize the type of topological order). Everywhere else the full Chern number is accurately reproduced. Thus the sublattice entanglement, as measured by the norm $|\mathbf{S}_{b/w}|$, indeed provides a good experimental measure for the fidelity of the winding number.

8.3.4 Distinguishing topological phases by only parity measurements

In Section II.C we argued that the parity of the winding numbers should be detectable from the density measurements only. These correspond to $\hat{S}^z_{(i)}$ measurements that, when applied to our staggered model, will give the compact surfaces $\mathbf{S}_b(p)$ and $\mathbf{S}_w(p)$ (see Fig. 8.8 for an illustration). By applying the protocol of counting the saddle points, assigning the parities $|\tilde{\nu}_b|$ and $|\tilde{\nu}_w|$ accordingly and adding them up, Fig. 8.7 shows that we can accurately reproduce the absolute value of the Chern number everywhere in the phase diagram. To be precise, we find that the following always holds: (i) $N = |\tilde{\nu}_b| + |\tilde{\nu}_w| = 0$ coincides always with the trivial $\nu = 0$ phase, (ii) $N = 1$ corresponds always to the non-Abelian topological phase with $|\nu| = 1$, and (iii) we find $N = 2$ only when the system is in the $|\nu| = 2$ phase. Thus the experimentally accessible density measurements are sufficient to distinguish between all the topological phases of our model.

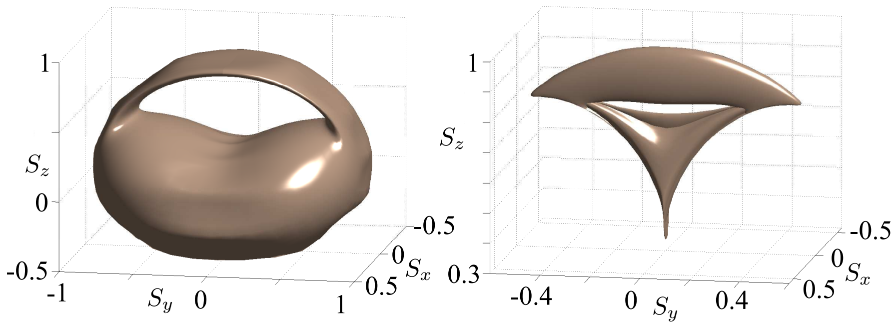

Fig. 8.8: Illustration of the vector fields $\mathbf{S}_{(i)}(p)$ for a $\nu = -1$ phase. Here we plot the values of $\mathbf{S}_{(b)}$(left) and $\mathbf{S}_{(w)}$(right) for (δ, μ)=(1,3). It can be seen that $\mathbf{S}_{(b)}$ winds once around the origin, thus giving a partial $|\tilde{\nu}_b| = 1$ contribution, while $\mathbf{S}_{(w)}$ does not enclose the origin so it gives zero contribution. Thus we verify that $|\nu| = |\tilde{\nu}_b| + |\tilde{\nu}_w|$

8.3.5 Robustness to perturbations

So far we shown that our detection scheme based on decomposition to sublattice observables accurately captures the phase diagram of our model except for special regions where the sublattices are too entangled. While this imposes accuracy limitations when applying the scheme, one may also ask how reliable the scheme is to the presence of perturbations in the Hamiltonian 8.5. In the next section we will propose an optical lattice implementation of our model. Here, we consider two general types of imperfections that one expects to be present in cold atom experiments: a harmonic trapping potential that breaks translational invariance, and finite temperature.

We numerically simulate the trap in a finite $L \times L$ lattice with open boundary conditions by introducing in our Hamiltonian (Eq.8.5) the chemical potential term $\mu_{\mathbf{j}} = \mu + (-1)^{j_x}\delta + Md^2\omega^2[(j_x - L/2)^2 + (j_y - L/2)^2]$, where M is the mass of the atomic species and d is the lattice spacing. Assuming that a local density approximation holds [47], a spatially dependent chemical potential induces in general the coexistence of different phases: some of insulating character, some not; some with topological order, some with no order at all. The Chern number is no longer defined in the absence of translational invariance. However, the winding number (8.1) can still be used to identify the existence of topological order, because regions in a trivial phase do not contribute to the expectation values $\mathbf{S}_{(i)}$ [6]. Indeed, Fig. 8.9 shows that all topological phases are robust for a wide range of trapping frequencies ω. We conclude that at least for small perturbing potentials the winding number 8.4 will still offer a reliable characterization of the phase diagram.

To model the effect of finite temperature T we restrict to fermionic excitations in the lower band with no thermal vortex excitations. The thermal state is then a product state in the momentum space. Computing the expectation values 8.2 both numerically and analytically, we find that temperature only leads to a change

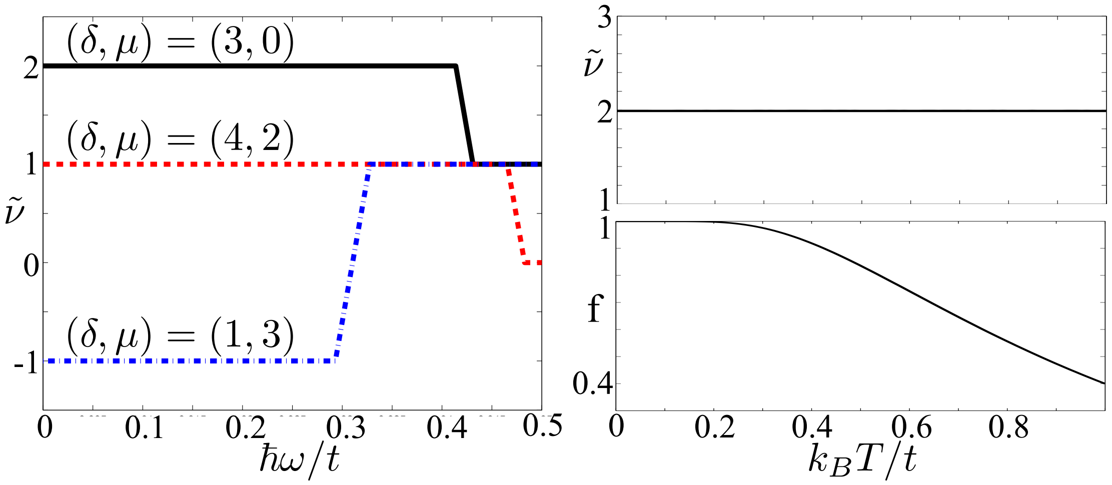

Fig. 8.9: *Left:* Winding numbers $\tilde{\nu}$ as functions of the trapping frequency ω in a finite 15×15 site system. *Right:* The winding number and the visibility, i.e. norm of the vector field $\mathbf{S}^{\text{th}}_{(i)}(\mathbf{p},T) = f(k_BT)\mathbf{S}_{(i)}(\mathbf{p},0)$ at finite temperature T, in a uniform system without a trap.

in the norm of the observables, $\mathbf{S}^{\text{th}}_{(i)}(\mathbf{p},T) = f(k_BT)\mathbf{S}_{(i)}(\mathbf{p})$. While theoretically such effect can just be normalized away, experimentally this corresponds to a reduced visibility ($0 < f(k_BT) < 1$) in the time-of-flight measurements. Since the supression of the norm, exactly like high entanglement between subattices, makes it harder to obtain $\mathbf{S}_{(i)}(\mathbf{p})$ accurately, finite temperature implies that higher resolution measurements are required. Assuming that this is within the state-of-the-art experimental precision, we numerically verify in Fig. 8.9 that the winding number 8.1 still faithfully reproduced. Thus we conclude that finite temperature can be compensated for by increased precision and therefore it does not pose a fundamental challenge for our detection scheme.

8.4 Optical lattice implementation and the experimental detection of the winding numbers

In this last section we first outline a scheme to implement our staggered model with cold atoms in an optical lattice. We then show how to recover, from time of flight images in this particular setup, the winding numbers with which the phase diagram from Fig. 8.5b can be experimentally reconstructed. A quantitative analysis of the parameters for a particular implementation is then presented.

8.4.1 Optical lattice implementation

As Hamiltonian 8.5 describes spinless fermions, it can be implemented with atoms in a single internal state only. However, it can also be implemented with two atomic states, which can be advantageous for two reasons. First, by trapping the distinct atomic states in a checkerboard state-dependent optical lattice, denoted by the circles and squares in Fig. 8.1, we can use Raman-assisted tunnelling [48] to implement both the complex tunnelling amplitudes and control the chemical potentials. Second, using two atomic states we can implement the pairing terms between neighbouring sites using s-wave Feshbach resonances [19, 49]. If we were using only a single atomic state, the Pauli exclusion principle would force us to employ p-wave Feshbach resonances, which are harder to observe [78, 39].

We propose to generate the lattice of model 8.5 by focusing the diffracted image from a holographic mask onto the focal plane of an extremely large aperture lens [14]. The sublattices host different hyperfine states of the same atomic species which are sensitive to different polarisations of the trapping laser beams. Both sublattices can be displaced one on top of another by means of an electro-optic modulator [55].

We also superimpose a superlattice potential $V = V_{OFF}\sin^2(\pi x/\sqrt{2}d)$, where d is the lattice constant for each sublattice. V_{OFF} can be controlled by changing the intensity of the laser beam, which creates this potential. This superlattice structure effectively adds a tuneable energy offset V_{OFF} to every other column in the lattice. This offset serves a two-fold purpose: it allows for independent Raman tunnelling in each direction and acts as a knob for changing the value of the chemical potential difference $\mu_w - \mu_b$, as it is shown in Fig. 8.10.

Our implementation employs a Raman-assisted tunnelling scheme on an optical lattice with a pattern of phases [48, 31, 66], as shown in Fig. 8.3. In this figure we use a convention that the tunnelling direction is set to go from one species (circle) to the other (square). Reversing the direction complex conjugates the tunnelling amplitude. The tunnelling element between sites $\mathbf{j}$ and $\mathbf{j}'$ in a Raman transition assisted by two lasers of wavevectors $\mathbf{k}_1$ and $\mathbf{k}_2$ of amplitude Ω_R can be parameterised as $t = e^{i\mathbf{q}\cdot\mathbf{r}_+}t_0(d, \mathbf{q})$, where t_0 is a real number which only depends on the nearest-neighbour distance d, the Raman frequency Ω_R and the difference between the Raman beam wavevectors $\mathbf{q} = \mathbf{k}_1 - \mathbf{k}_2$. Also $\mathbf{r}_+ = (\mathbf{j} + \mathbf{j}')/2$ is the midpoint between the two neighbouring sites. The phase of the hopping parameter is thus determined by wavevector $\mathbf{q}$. We can see in Fig. 8.1 that two different phase wavelengths for the horizontal and vertical transition amplitudes are needed. So implementation of this hopping pattern requires a Raman pair for each direction. Fig. 8.10 shows the energy level structure which accomplishes this pattern.

In order to study the experimental feasibility of the proposal, we will now present a possible implementation using ^{40}K atoms in a state-dependent optical lattice. As a summary of the details given below, we expect a small heating rate [6] of about 1 Hz which is the dominant time-scale for decoherence. Using a potential depth of about 22 recoil energies, ordinary hopping can be suppressed in each sublattice, while still having a significant overlap between neighbouring wave functions —the quantity that determines the strength of both t and Δ. Typical estimates for the Raman-assisted tunnelling [31, 66] and the induced s-wave pairing [49], give us an estimate of about 1 kHz for t, and 0.5 kHz for Δ.

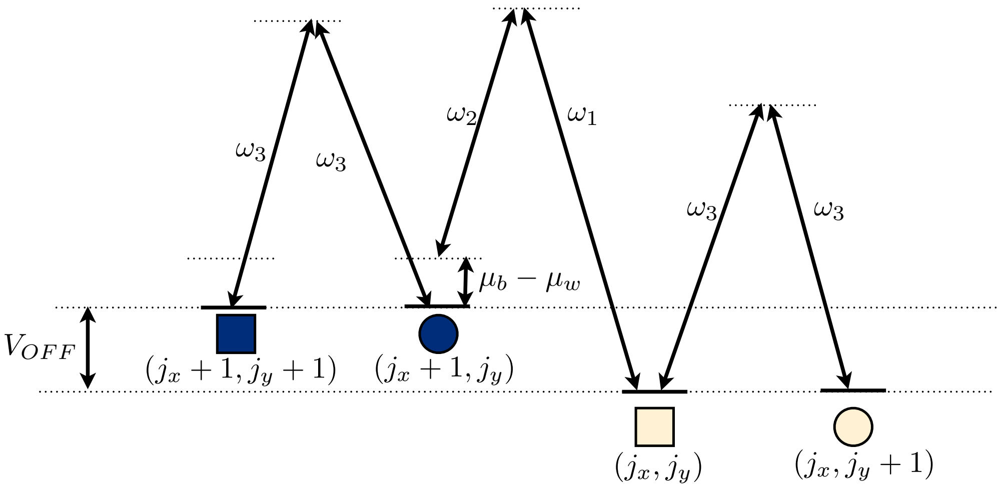

Fig. 8.10: Energy level structure, showing how two sets of Raman beams allow for independent transitions due to the presence of the offset V_{OFF}. This offset can be tuned to allow for different values of the difference in chemical potentials $\mu_w - \mu_b$. The indices (j_x, j_y) stand for horizontal and vertical position on the lattice, respectively.

These numbers could be improved through the use of alkaline-earth atoms [31].

Quantitative analysis of the optical lattice parameters

We now provide a quantitative analysis to justify the feasibility of implementing the presented model in an optical lattice. Together with our own numerical simulations, the analysis provided in Refs. [31, 49, 43] is also used. We particularise our results to two interpenetrated square lattices, each of them with lattice constant $d \simeq 400$nm and hosting a hyperfine state of ^{40}K.

The energy scale of the model parameters is constrained to an interval which depends on the lattice depth. This interval is bounded from below by the heating rates and the suppressed natural hopping within sublattices; it is bounded from above by the separation between lattice bands. We will show that all model parameters fit within this energy scale window, demonstrating the feasibility of the proposed implementation.

We first focus on the lower end of this interval. The natural hopping parameter decreases roughly exponentially with the lattice depth. Our numerical simulations (Fig. 8.11) show that the hopping reaches a value of $t_{Nat} \lesssim 10^{-3}E_R$ for a lattice with depth $V_0 \simeq 22E_R$, where V_0 is the lattice depth and E_R is the recoil energy of the lattice (around $E_R/h = 8$kHz for the choice above). Therefore, we can expect a natural hopping of the order of 5Hz. Our results are in agreement with previous analytical estimates [102].

The second constraint lower bound of our interval of acceptable parameters is provided by the photon scattering rate, which increases with the depth the lattice.

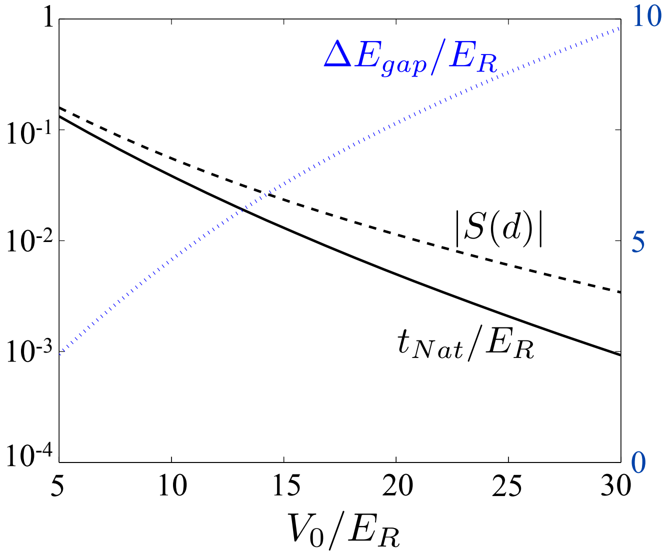

Fig. 8.11: Realistic band structure simulation of the intertwined lattice setup. *Left axis:* Dependence of the natural hopping t_{Nat} (black, solid) and the overlap between neighbouring wave functions $|S(d)|$ (black, dashed) on V_0/E_R. *Right axis:* Dependence of the bandgap ΔE_{gap} (blue, dotted) on the lattice depth, V_0/E_R.

These heating rates are a significant problem for state-dependent setups, because in these designs the maximum detuning of light is limited by the energy splitting between hyperfine states. More precisely, the heating rate can be estimated as $\gamma_h \simeq (\Gamma/\delta_{Deph})V_0$, where Γ is the spontaneous emission rate of the atom, and δ_{Deph} the detuning. The ratio Γ/δ_{Deph} critically depends on the atomic species, ranging from about $0.1/h$ for ^6Li to about $10^{-5}/h$ for ^{40}K. We focus on this last atomic element, obtaining a heating rate of about $1-2$ Hz for the above mentioned $V_0 \sim 22E_R$, but we remark the possibility of using alkaline-earth atoms to bring this value down to about 0.01 Hz [31].

Finally, all energy scales must be significantly smaller than the bandgap, ΔE_{gap}. Our simulations evaluate this bandgap to be over 60kHz for our $V_0 \simeq 22E_R$ lattice (Fig. 8.11). Again this result agrees with comparable calculations in similar setups [31]. In summary, our parameters $(\mu_b - \mu_w, t, \Delta)$ should all move in the $0.1 - 1$kHz range in order to successfully implement our proposed model.

The chemical potential difference δ can independently tuned by the auxiliary offset lattice intensity V_{OFF}. This offset can be easily set to the desired energy range, since it just requires a superlattice modulation which is much smaller than the intensity of the main lattice ($V_{OFF} < E_R$).

The Raman tunnelling t is proportional to the Raman beam intensity, $|t| = \hbar\Omega S(d)$, and the overlap between Wannier wave functions, $w(x,y)$, in neighboring wells of the superlattice, $S(d) = \iint w^\star(x,y)w(x-d/2, y-d/2)\mathrm{d}x\mathrm{d}y$. We estimate numerically this overlap to be $S \simeq 10^{-2}$ for $V_0 = 22E_R$ (Fig. 8.11). Therefore, a feasible value $\Omega \sim E_R/\hbar$ would keep $|t|$ in the desired 1 kHz order of magnitude.

Finally, the pairing Δ depends on the strength of the coupling to the molecular reservoir and the bosonic bath density [43] as $|\Delta| = g\sqrt{\rho}S(d)$. The overlap of the fermionic wave functions again plays an important role and we assume the density profile of the bosonic bath to be uniform. Estimates from previous proposals [49] based on condensed fermionic pair experiments [103] show that $|\Delta| \simeq 0.5$kHz is challenging but possible between nearest neighbours of the superlattice.

8.4.2 Experimental construction of the winding numbers from time-of-flight images

To obtain the full winding number $\tilde{\nu}$ one need to construct the independent integer-valued winding number $\tilde{\nu}_{(i)}$ for each pseudospin component. In the case of our model, the psedospin components coincide with the "black" ($i = b$) and "white" ($i = w$) sublattices that are distinguished by their different chemical potential. In an optical lattice implementation, this energy offset between the atoms can be employed to release them from one of the two sublattices at a time and thus the observables $\vec{\Sigma}_{(i),p}$ for each sublattice can be independently evaluated. We outline below a general protocol to obtain all components of the vectors $\mathbf{S}_{(i)}(p)$ from which the sublattice winding numbers $\tilde{\nu}_{(i)}$ can be constructed.

The experimental measurement of the operators 8.3 in an optical lattice setting employs the fact that time-of-flight images give direct access to the momentum space densities $\langle n_{(i),\mathbf{p}}\rangle = \langle a^\dagger_{(i),\mathbf{p}} a_{(i),\mathbf{p}}\rangle$, as outlined in chapter 7. These are sufficient to fully determine $S^z_{(i)}$, which, as discussed in Section III.B, enables to unambiguously distinguish between all the distinct types topological phases (different $|\nu|$). Thus the time-of-flight images, a standard technique in optical lattice experiments, are sufficient to identify the phases of our model.

In order to construct the full winding number one needs to obtain also the orthogonal components $S^x_{(i)}$ and $S^y_{(i)}$. They can in general be obtained by suitably switching off the pairing and tunnelling terms of 8.5 before releasing the atoms from the trap. This will rotate the observables $\Sigma^{x,y}_{(i),p}$ to $\Sigma^z_{(i),p}$, which can then be measured from time-of-flight images as above. For instance, when hopping in both directions and pairing in x-direction is suppressed, e.g. by raising the lattice in this direction, the Hamiltonian 8.5 acquires the form

$$H_{\text{rot}} = \Delta \sin(p_y) i \left(a^\dagger_{(i),\mathbf{p}} a^\dagger_{(i),\mathbf{p}} - \text{H.c.} \right) \propto \Sigma^y_{(i),\mathbf{p}}. \tag{8.14}$$

This operator implements a rotation around the S^y axis, mapping the value of the S^x operator onto the S^z axis, which after time t gives

$$S^z(p,t) = \cos(\theta_p) S^z(p,0) + \sin(\theta_p) S^x(p,0), \tag{8.15}$$

with $\theta = \Delta \sin(p_y)t/\hbar$. Time of flight image can again be used to measure this quantity from which the value of S^x can be extracted once the unrotated component $S^z(p,0)$ has been determined. Finally, the value of S^y can be obtained experimentally using a similar two-step process as above. Evolving the system with only hopping along the y direction maps S^y to S^x, which when followed by a pairing evolution can again be mapped to the directly observable S^z.

The dependence of the evolution 8.15 on the momentum p_y implies that the Hamiltonian rotations around $p_y = 0, pm\pi/2, pm\pi$ will be infinitely slow. This experimental challenge can be overcome in two ways. One way is to numerically post-process the measurements by extrapolating smoothly the values of $\mathbf{S}$ from the measurements of S^z, S^x and S^y. We have numerically verified that given $|\mathbf{S}|$ does not become zero anywhere, and that the angles in the xy plane behave smoothly across the Brillouin zone, this can be efficiently performed. An alternative is to use additional complementary noise correlation measurements $\langle n_{(i),\mathbf{p}} n_{(i),-\mathbf{p}} \rangle$. Using Wick's theorem such an observable can be written in the form

$$\begin{aligned} \langle n_{(i),\mathbf{p}} n_{(i),-\mathbf{p}} \rangle = {} & \langle n_{(i),\mathbf{p}} \rangle \langle n_{(i),-\mathbf{p}} \rangle + |\langle a^\dagger_{(i),\mathbf{p}} a^\dagger_{(i),-\mathbf{p}} \rangle|^2 \\ & + \langle a^\dagger_{(i),\mathbf{p}} a_{(i),-\mathbf{p}} \rangle \langle a_{(i),\mathbf{p}} a^\dagger_{(i),-\mathbf{p}} \rangle . \end{aligned} \tag{8.16}$$

As $\langle n_{(i),\mathbf{p}} \rangle$ follows from the usual time of flight images and $\langle a_{(i),\mathbf{p}} a^\dagger_{(i),-\mathbf{p}} \rangle$ can be obtained from them after Bragg scattering with momentum $2\mathbf{p}$ (for our model they always vanish), in essence noise correlations give us access to the orthogonal projection of the pseudo-spin components, $(S^\perp)^2 = (S^x)^2 + (S^y)^2$. Thus once S^x has been obtained, the noise correlations can be employed as an alternative way to obtain S^y.

8.5 Conclusions

This chapter has presented a general method to detect the Chern number of superconducting models from time-of-flight images. This method is readily applicable to any topological superconducting state regardless of the microscopic realization [81, 100, 49]. The only requirement is the ability to measure independently the relevant operators for each pseudospin component, such as spin orientation, internal atomic states or sublattices due to staggering. While not restricted only to, the proposed method is particularly suited for optical lattice experiments where time-of-flight images, a standard technique, readily give access to the relevant operators. We also showed that time-of-flight images of the cloud, even in the absence of a manipulation protocol, can give sufficient information (the absolute value of the Chern number) to distinguish between the different types of topological order. With the preparation of topologically ordered states with cold atoms in optical lattices as the ultimate goal, this provides a simple and reliable diagnostic tool to probe the nature of the prepared states.

To demonstrate our detection scheme, it has been applied to a model of staggered spinless fermions with s-wave pairing, a new route to topological phases with cold atoms. Topological phases with Chern numbers $\nu = 0$, $\nu = \pm 1$ and $\nu = \pm 2$ can be robustly identified. The few disagreeing parameter regimes were found to correlate with high sublattice entanglement, which is a physical observable in itself; this is a perfect illustration of the results presented in chapter 5. Furthermore, we showed that the detection scheme remains robust under two omnipresent perturbations in cold atom experiments: translational invariance breaking trapping potential and finite temperature. The latter could be compensated for by increasing detection precision, which contrasts with the behaviour of topological entanglement entropy, an alternative probe for topological order in cold atom systems [1]: in the thermodynamic limit it vanishes at any finite temperature rendering its applicability challenging [23, 45]. In addition, and unlike our method, topological entropy can not distinguish topological phases with same total quantum dimensions.

Finally, it is explicitly demonstrated that the proposed model of staggered spinless fermions with s-wave pairing is adiabatically connected to Kitaev's honeycomb model [53]. The proposed optical lattice implementation would thus offer an alternative route for realizing this celebrated model. In this realization we could relate the staggering in the chemical potential, an experimentally accessible parameter, to the presence or absence of a background vortex lattice. We showed that the presence of such a lattice underlies the Chern number $\nu = \pm 2$ phases. As this phase can only arise as the collective state of Majorana modes, detecting the change in the Chern number when the vortex lattice is switched on provides the desired global probe for the existence of Majorana modes.

9. DETECTION OF NON-ABELIAN PHASE TRANSITIONS THROUGH WINDING NUMBERS

9.1 Summary

This chapter is the last stepping stone in the path we have been following: the detection of the topological bulk properties of non-trivial insulators (or superconductors). While there is no well-understood, safe shore in sight, the contents of this chapter provide the most the most suggestive results yet as to the connection between topology, winding numbers and entanglement in an atomic cloud.

The main result of this chapter is that the pseudospin winding number is a topological invariant which can be used to predict phase transitions, even though the system as a whole may not be characterizable. Moreover, the information (predictive power) of this quantity is related to the entanglement between the pseudospin degree of freedom and the rest of the system. There is a crucial difference between the results shown here and those in chapter 8: in the latter, we could make use of the analytical results of chapter 5 to fully understand the role of each pseudospin winding number; the winding numbers were there parts of a jigsaw whose full image we know. Here, by contrast, the winding number is a lone piece of information without any support, it is only (a bit) puzzling that it can be numerically shown to give out information about the topological phase transitions. If anything, this chapter is a motivation to further research the role of partial invariants in complicated systems - possibly interacting, non-tractable setups.

As always along this thesis, we present a model which is used to show the power of our proposed method. In this case, it is a model of non-interacting, spinful fermions in a square lattice. The fermions are subjected to a magnetic field and a spin-orbit coupling term, which add up to form a non-abelian potential. Two special cases of the model are carefully analyzed, corresponding to magnetic fields which break or break not time-reversal symmetry. Our analysis of the role the winding number plays in this characterization is provided in the latter case, which is richer. In particular, there are topological semimetal-to-insulator transitions which can be diagnosed through the winding number; this $\mathcal{T}$-broken regime presents Chern number $\nu = 2$ phases.

As a small bonus, and as promised in chapter 7, this chapter also presents a better approximation to the winding number integral in terms of the discretized vector field observables (see Eq.9.24). This approximation is shown to converge very rapidly to the integer winding number with even a small number of observables.

This chapter is organized as follows: we first present and motivate the model, together with a clear analytical description of its symmetries and its relation with previous topological models. There is also a discussion of what optical lattice setups might be best at implementing the model. We then go on to illustrate the topological characteristics of the model under magnetic fields which either conserve or break time-reversal symmetry. It is shown that only the latter can support topological insulator phases. Finally, we quickly review the winding number detection method and provide full details about the differences which appear when we apply it in this model (which cannot be cast in a pseudospin form). The aforementioned integral approximation is mentioned, and a numerical analysis for this model is provided.

9.2 Description of the model

We consider a tight-binding model of two-component fermionic atoms loaded in a square lattice. We assume that the atoms are subjected to both a synthetic magnetic field, with a flux Φ per plaquette, and a translationally invariant non-Abelian SU(2) gauge field, which plays the role of spin-orbit coupling. These two elements influence the nearest neighbor tunneling amplitudes in different ways along the x and y directions, with their effect being described through the following U(2) gauge potential [35, 71]:

$$\vec{A} = \frac{2\pi\,\Phi}{a^2\,\Phi_0}\,(0,x)\,\sigma_0 + \frac{q}{a}\,(\sigma_x,\sigma_y)\ , \tag{9.1}$$

where Φ_0 is the elementary flux of the synthetic magnetic field, corresponding to an Abelian phase 2π acquired by an atom surrounding a plaquette, a is the lattice constant, $q \in [0,\pi]$ characterizes the intensity of the non-Abelian component, σ_x, σ_y are the usual Pauli matrices and σ_0 is the 2×2 identity matrix. We consider only positive values of q, since the case with $q < 0$ is equivalent up to a basis transformation, $\vec{A}(-q) = \sigma_z\,\vec{A}(q)\,\sigma_z$. The first term in Eq. (9.1) defines the Abelian contribution of the gauge potential in the Landau gauge, where only the tunnelings along y assume a position-dependent phase, not depending on the spin degree of freedom. The second term describes instead the spin-dependent non-Abelian term, which is translationally invariant and it is gauge equivalent to both a Rashba and a Dresselhaus spin-orbit term.

The tight-binding Hamiltonian of the system reads:

$$H = t\sum_{\vec{r},s,s'}\left[U_{x,ss'}\,c^{\dagger}_{\vec{r}+\hat{x},s'}\,c_{\vec{r},s} + U_{y,ss'}(x)\,c^{\dagger}_{\vec{r}+\hat{y},s'}c_{\vec{r},s}\right] + \text{h.c.}\,, \tag{9.2}$$

where $\vec{r} = (x,y)$ denote the lattice sites, s labels the two components and the tunneling matrices U_x and U_y are defined as:

$$U_x = \exp\left(i\int_{x,y}^{x+a,y} A_x\,\mathrm{d}x\right) = \exp\left(iq\,\sigma_x\right)\ , \tag{9.3}$$

$$U_y = \exp\left(i\int_{x,y}^{x,y+a} A_y\,\mathrm{d}y\right) = \exp\left(i2\pi\frac{x}{a}\frac{\Phi}{\Phi_0} + iq\,\sigma_y\right)\ . \tag{9.4}$$

Following our gauge choice (9.1), only U_y depends on position through the Abelian phase $2\pi\frac{x}{a}\frac{\Phi}{\Phi_0}$ (see Fig. 9.1).

We observe that the Hamiltonian (9.2) is invariant under the exchanges $t \to -t$, $q \to \pi - q$ through the basis transformation σ_z. This implies that the sign of t can

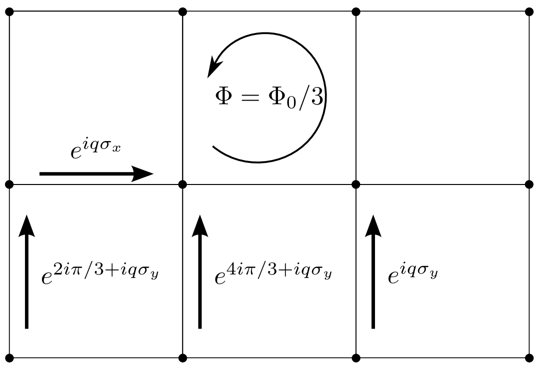

Fig. 9.1: Square lattice model with non-Abelian gauge potential. The tunneling operators U_x and U_y, defined in Eqs. (9.3,9.4), are represented for $\Phi = \Phi_0/3$. $U_x = e^{iq\sigma_x}$ is independent on the position, whereas U_y is characterized by a phase dependent on x which determines the Abelian flux Φ per plaquette.

be chosen without loss of generality (of course, if $t \to -t$, then the following results are valid provided that $\nu \to 2 - \nu$, where ν is the number of fermions per site). The validity of the Peierls substitution leading to the tight-binding Hamiltonian (9.2) has been discussed for spin-orbit coupled atoms in optical lattices [77], where it was shown that for large enough values of the strength of the periodic potentials it agrees with results obtained from numerically computed Wannier functions.

To understand the nature of the gauge potential (9.1) it is useful to calculate the Wilson loop around a plaquette [35]: the Abelian part of the potential gives rise to the phase $2\pi\,\Phi/\Phi_0$, whereas the non-Abelian term, due to the commutation relation between U_x and U_y, generates a non-trivial unitary operator for each $q \neq 0, \pi$. However, such a plaquette operator does not depend on its position, emphasizing the translational symmetry of the system along $\hat{y}$. In particular, if the magnetic flux is commensurate with the elementary flux, $\Phi/\Phi_0 = m/n$, then the wave function can be written as

$$\psi(x, y) = e^{ik_x x}\, e^{ik_y y}\, u(x)\,, \tag{9.5}$$

where $u(x)$ is periodic with period n (hereafter we set $a = 1$). The resulting first Brillouin zone is given by $k_x \in [0, 2\pi/n)$ and $k_y \in [0, 2\pi)$, as in the case when only the magnetic field is present. The parameter q does not influence the definition of the Brillouin zone and of the allowed quasi-momenta since the non-Abelian part of the gauge potential is translationally invariant.

We conclude this Section with a brief analysis of possible implementations of the potential (9.1). There are two different ingredients to be combined: an Abelian net flux per plaquette (parametrized by Φ) and a spin-dependent hopping element (parametrized by $q\vec{\sigma}$). A detailed discussion of the simulation of non-Abelian SU(2) potentials with alkaline atoms can be found in Ref. [66]. There, the spin degree of freedom is coded in two hyperfine levels of ^{40}K. Zeeman splitting allows for independent addressing of the transitions between different spin states, thus creating the desired spin-dependent hopping amplitude. An additional superlattice could then be used to engineer a rectified magnetic flux, independent of the spin state of the system [31].

A comprehensive implementation proposal for both the Abelian and non-Abelian potential can be found in [32]. This setup features a state-dependent lattice loaded with the ground state and a metastable excited state of ^{171}Yb. The narrow transition between the two trapped states guarantees a negligible heating rate, and naturally paves the way for implementing a rectified flux scheme. Polarization of the Raman lasers is used to engineer tunneling elements between different spin states, whereas a superlattice is again imposed to distinguish resonances in the two spatial directions.

As a final note, we would like to mention that the measurement protocol outlined in Section 9.4 suits the presented implementation proposals; in particular, the time of-flight measurement of the pseudospin degree of freedom is simplified by the presence of the magnetic field, which discriminates between different spin states.

9.3 Topological phases and topological phase transitions

9.3.1 Conserving time-reversal symmetry: magnetic flux $\Phi_0/2$

The first case we analyze is the one with $n = 2$, where an atom acquires an Abelian phase π encircling a plaquette. This value of the flux is the only one maintaining time-reversal symmetry. The potential (9.1) reads:

$$\vec{A} = \pi(0, x)\,\sigma_0 + q\,(\sigma_x, \sigma_y)\ . \tag{9.6}$$

In this case the unit cell of the system is composed of two subsets of sites corresponding to even and odd x coordinates. Therefore we can define an effective pseudospin 1/2 degree of freedom and a new set of Pauli matrices τ_i referring to it, with $\tau_z = \pm 1$ indicating even and odd x-coordinates respectively. The Hamiltonian (9.2) with potential (9.6) reads in quasi-momentum space:

$$\begin{aligned}\frac{H(\vec{k})}{2t} = \cos q \cos k_y\,\tau_z\sigma_0 - \sin q \sin k_y\,\tau_z\sigma_y + \\ + \cos q \cos k_x\,\tau_x\sigma_0 - \sin q \sin k_x\,\tau_x\sigma_x\,.\end{aligned} \tag{9.7}$$

It is a 4×4 matrix involving direct products of Pauli matrices (i.e., $\tau_z\sigma_y$ stands for $\tau_z \otimes \sigma_y$ and so on). The Hamiltonian (9.2) is expressed in terms of (9.7) as

$$H = \sum_{\vec{k}, s, s', \tau, \tau'} c^{\dagger}_{s',\tau'}(\vec{k})\, H_{s'\tau', s\tau}(\vec{k})\, c_{s,\tau}(\vec{k})\,, \tag{9.8}$$

where the sum is on the first Brillouin zone, $c_{s\tau}(\vec{k})$ is the Fourier transform of $c_{s\tau}(\vec{r})$ and $\tau = \pm 1$ is the pseudospin index.

In order to understand the topological characteristics of the model, it is useful to examine the topological symmetry class in the Altland and Zirnbauer classification [8, 80]. We consider the set of discrete anti-unitary symmetries and we identify at half-filling ($\mu = 0$) the following time-reversal symmetry T and particle/hole-like symmetry C [82]:

$$\sigma_y \, H^T(\vec{k}) \, \sigma_y \quad = H(-\vec{k}) \quad \mathrm{T-symmetry} \tag{9.9}$$

$$\tau_y \sigma_y \, H^T(\vec{k}) \, \tau_y \sigma_y \quad = -H(-\vec{k}) \quad \mathrm{C-symmetry}; \tag{9.10}$$

the corresponding chiral unitary symmetry is generated by generated by τ_y. Given these discrete symmetries, the topological symmetry class in the Altland and Zirnbauer classification [8] is DIII for generic values of $q \neq p\,\pi/2$, with integer p. DIII is a topologically non-trivial class in two dimensions which can support helical Majorana edge modes [76]. For the particular values $q = 0, \pi$ the gauge potential corresponds to the presence of the magnetic field only and the Hamiltonian acquires the additional SU(2) spin symmetry; for $q = \pi/2, 3\pi/2$, instead, the two non-zero terms of the Hamiltonian, proportional to $\tau_z \sigma_y$ and $\tau_x \sigma_x$, commute and generate a U(1)×U(1) symmetry, while σ_z anti-commutes with the Hamiltonian. Finally, when the chemical potential $\mu \neq 0$ the T-symmetry (9.9) is conserved, but the C-symmetry (9.10) is broken, leading to a class AII system.

The effective realization of the topological insulating phase with Majorana edge modes depends critically on the band structure and on the appearance of energy gaps, as a function of the Hamiltonian parameter q. For generic values of q the system has four energy eigenstates: we label them in increasing order ($\{1, 2, 3, 4\}$). The corresponding bands in the Brillouin zone intersect for some particular quasi-momenta. Bands 1 and 2 coincide for every q at $(k_x, k_y) = (0, 0)$, with energy $E_-(0, 0) = -2\sqrt{2}\, t \cos q$. The same happens for bands 3 and 4, with energy $E_+(0, 0) = 2\sqrt{2}\, t \cos q$. Bands 2 and 3 instead have a common point, still for every q, at $(k_x, k_y) = (\pi/2, \pi/2)$, with vanishing energy (see Fig. 9.2). We conclude that the Hamiltonian does not have an energy gap for any value of q, and the system is always in a metallic or semimetallic phase, depending on whether the chemical potential falls in a bulk band or is set exactly at the intersections between them.

The same result is obtained by introducing an anisotropy in the non-Abelian potential by considering

$$\vec{A} = \pi(0, x)\, \sigma_0 + (q_x \sigma_x, q_y \sigma_y) \ . \tag{9.11}$$

This generalization does not affect the symmetry class; the system remains in class DIII (or AII). Again the bands always touch at some points of the Brillouin zone; therefore the system is always in a metal or semimetal phase and there is no phase transition driven by the variation of the non-Abelian gauge parameters q_x and q_y.

In order to obtain nontrivial topological phases, characterized by symmetry-protected edge modes, and topological phase transitions between them, it is necessary to open a gap between some bands. One possibility is to break time-reversal

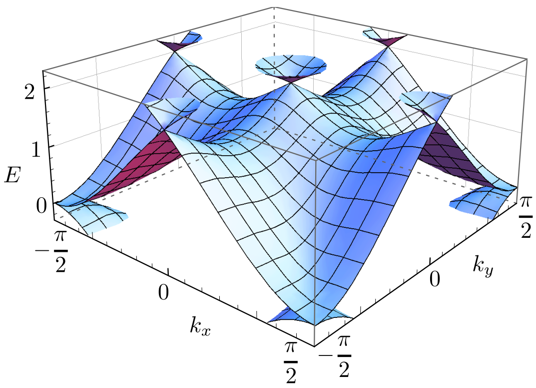

Fig. 9.2: The spectrum of the Hamiltonian (9.7) is shown for $q = \pi/4$. The Dirac cones connecting the energy bands 3 and 4 are clearly visible in the upper part of the plot at $E = 2$, whereas the gap between the bands 2 and 3 closes at $(k_x, k_y) = (\pm\pi/2, \pm\pi/2)$ and $E = 0$. The spectrum is symmetric about $E = 0$ and no energy gap appears for any value of q. The energy is expressed in units of t.

symmetry. In the following we will achieve this by considering a system with magnetic flux $\Phi_0/3$ per plaquette.

9.3.2 Breaking of time-reversal symmetry: magnetic flux $\Phi_0/3$

By introducing in the system a fractional magnetic flux per plaquette $\Phi = m\,\Phi_0/n$ with $n \neq 2$, one obtains a series of bands which are separated by energy gaps, corresponding to the deformation of the Hofstadter butterfly spectrum due to the presence of the non-Abelian potential. Such deformations have already been analyzed for several potential configurations [70, 34, 35]. We exploit the presence of these gaps to generate and identify the different topological phases that appear with the potential (9.1), whose transitions can be driven by the non-Abelian parameter q.

We focus in particular on the case with Abelian flux $\Phi_0/3$ ($n = 3$), which is the simplest one breaking time-reversal symmetry and presenting topological phase transitions. The corresponding gauge potential reads:

$$\vec{A} = \frac{2\pi}{3}(0, x)\,\sigma_0 + q\,(\sigma_x, \sigma_y)\ . \tag{9.12}$$

The unit cell is composed of three sites and it is useful to introduce a new pseudospin-1 degree of freedom, the related operator being labeled by T_z, to identify the x coordinate modulo 3. The hopping operator in the $\hat{y}$ direction is diagonal in T_z, whereas the hopping along $\hat{x}$ is not. By introducing the two hopping matrices

$$T_x = \begin{pmatrix} 0 & 0 & 1 \\ 1 & 0 & 0 \\ 0 & 1 & 0 \end{pmatrix}\ , \quad T_z = \begin{pmatrix} e^{i\frac{2\pi}{3}} & 0 & 0 \\ 0 & e^{i\frac{4\pi}{3}} & 0 \\ 0 & 0 & 1 \end{pmatrix}\ , \tag{9.13}$$

the tunneling operators in (9.3) and (9.4) read:

$$U_x = T_x \, e^{iq\sigma_x} \,, \qquad U_y = T_z \, e^{iq\sigma_y} \tag{9.14}$$

(direct product of matrices is always intended). U_x and U_y are 6×6 matrices acting on the space defined by the tensor product of the lattice pseudospin-1 and the inner spin-1/2 degrees of freedom.

Since $n = 3$, the first Brillouin zone is defined by the quasi-momenta $k_x \in [0, 2\pi/3)$ and $k_y \in [0, 2\pi)$. In the quasi-momentum space the Hamiltonian reads:

$$\begin{aligned} H = -\mu \, \mathbb{I}_6 + T_x \, e^{iq\sigma_x} e^{ik_x} + T_x^\dagger \, e^{-iq\sigma_x} e^{-ik_x} + \\ + T_z \, e^{iq\sigma_y} e^{ik_y} + T_z^\dagger \, e^{-iq\sigma_y} e^{-ik_y} \,, \end{aligned} \tag{9.15}$$

where t is set to 1, μ denotes the chemical potential which changes the filling, and $\mathbb{I}_6$ is a 6×6 unit matrix. The Hamiltonian can be easily rewritten as:

$$\begin{aligned} H = -\mu \, \mathbb{I}_6 + \big[\cos q \left(T_x \, e^{ik_x} + T_z \, e^{ik_y}\right) + \\ + i \sin q \left(T_x \, \sigma_x e^{ik_x} + T_z \, \sigma_y e^{ik_y}\right)\big] + \text{h.c.} \,. \end{aligned} \tag{9.16}$$

For generic values of q the six eigenstates of the Hamiltonian (9.16), with energies $E_\lambda(\vec{k})$, describe five different spectral bands separated by energy gaps. There are five because the two central ones are always connected through Dirac cones.

Even though the bands are separated by gaps for every value of the quasi-momenta, due to their strongly bent shapes, indirect overlaps (the minimum of the higher band is lower than the maximum of the lower band) appear between the two lowest-energy bands and between the two highest-energy bands for q in a neighborhood of 0 or π. In these cases the non-Abelian potential is not strong enough to open an insulating phase separating these pairs of bands and when the chemical potential is such that two different bands are partially filled, the system is in a semimetal phase [32], despite the absence of Dirac cones.

For q far enough from 0 and π instead, the semimetal phases disappear and are substituted by insulating phases. Therefore the chemical potential μ determines the usual alternation of metallic and insulating phases appearing in correspondence to all the gaps of the system.

Other phase transitions, of a topological nature, appear for $q = \pi/3$ and $2\pi/3$ where the gaps between the two top bands and the two bottom bands directly close in Dirac cones. To understand the signature of this phase transition we analyze the topological features of the system. Since $T_x^\dagger \neq T_x^*$, one cannot find anti-unitary operators corresponding to discrete T- and C- symmetries. The Hamiltonian (9.16) is then in the same topological class of the quantum Hall effect, class A, in the Altland and Zirnbauer classification.

The Hamiltonian H describes a system which is topologically non-trivial and characterized by the presence of edge modes. They are localized on the boundary of the two-dimensional system and therefore can be observed only in bounded geometries, like the cylinder. Their energies interpolate between subsequent bands and their number is related to the topological invariants of the spectral bands. Moreover, due to the non-Abelian term, they do not present a fixed spin orientation; the non-Abelian potential in (9.1) is indeed equivalent to a Rashba spin-orbit coupling, which yields to a dependence of the spin polarization on the quasi-momentum.

Let us consider now values for q and the chemical potential such that the system is in a bulk insulating phase with an integer number of atoms per unit cell. Then the number of observed edge states per boundary is given by the sum of the Chern numbers of the bands with an energy smaller than the Fermi energy. Given the 6-component eigenfunctions $\psi_\lambda(\vec{k})$ of H (with λ labeling the bands), their Chern number C_λ is defined by [41, 91]:

$$\mathcal{C}_\lambda = \frac{i}{2\pi}\int_{\mathrm{BZ}} d^2k\left(\langle\partial_{k_x}\psi_\lambda|\partial_{k_y}\psi_\lambda\rangle - \langle\partial_{k_y}\psi_\lambda|\partial_{k_x}\psi_\lambda\rangle\right). \tag{9.17}$$

The sign of $\mathcal{C}_\lambda$ refers to the direction of the propagation of the edge modes associated with $\psi_\lambda(\vec{k})$.

In order to examine how the numbers and the features of the edge modes change by varying q (which is supposed to be in a range out of the semimetallic phase), let us label the Hamiltonian eigenfunctions from the lowest to the highest energy by an index $\lambda = -2, -1, 0^+, 0^-, 1, 2$. For generic values of q only bands 0^+ and 0^- are directly connected through Dirac cones whereas the other bands are separated by energy gaps, although often with the indirect energy overlaps discussed above that determine the presence of topological semimetal phases [32].

The energy gap between the bands -2 and -1 closes at $q = \pi/3$ for $k_x = \pi/3$ and $k_y = \pi/3 + 2\pi p/3$, with integer p (see Fig. 9.3). Analogously the gap between the two highest bands closes at the same value of q for $k_x = 0$ and $k_y = 2\pi p/3$. The same gaps close also at $q = 2\pi/3$, at interchanged quasi-momenta $\vec{k}$.

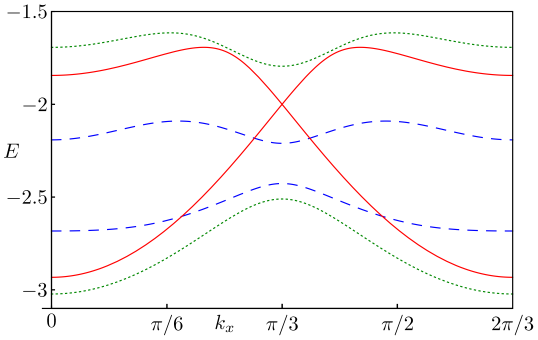

Fig. 9.3: The energies of the two lowest states of the Hamiltonian (9.16) are plotted for $q = \pi/5$ (blue dashed line), $q = \pi/3$ (red line) and $q = 2\pi/5$ (green dotted line), for $k_y = \pi/3$ and as a function of k_x. For $q = \pi/5$ and $q = 2\pi/5$ the lowest bands are separeted by a gap and, for filling $\nu = 1/3$, the system is in two different topological insulating phases. At $q = \pi/3$ the gap closes causing a topological phase transition. The energy is in units of the tunneling amplitude t and the chemical potential is fixed at $\mu = 0$.

From the analysis of the spectrum it is clear that this closing of the gap corresponds to a further Dirac cone appearing in the bulk of the system. However this does not correspond simply to a crossing of Landau levels, as we would expect in a similar system in the continuous limit [20, 21]; instead, it is a topological phase transition which changes the Chern numbers of the involved bands, thus affecting the number of edge states in a geometry with boundaries. No change in the Chern number arises instead along the phase transition between a semimetal and an insulating phase.

To calculate the number of edge states, let us consider the spectrum of an infinite stripe with two edges. We discuss first the case in which only the lowest energy band is fully occupied, whereas all the others are empty (filling 1/3, corresponding to one atom per unit cell). The number of propagating modes at each edge of the system coincides with the Chern number $\mathcal{C}_{-2}$, which is $+1$ for $0 < q < \pi/3$ (or $2\pi/3 < q < \pi$) and -2 for $\pi/3 < q < 2\pi/3$. Increasing the chemical potential and considering also the contribution of the second band $\mathcal{C}_{-1}$, we see from numerical calculations that the number of edge modes interpolating between the second and the lowest central band is 2 for $0 < q < \pi/3$ (or $2\pi/3 < q < \pi$) and -4 for $\pi/3 < q < 2\pi/3$; this implies that $\mathcal{C}_{-1}$ also changes from 1 to -2 and vice versa across the two phase transitions. Thus, going from $q < \pi/3$ to $q > \pi/3$, the edge states double and change their direction, as an effect of the non-Abelian potential. At $q = 2\pi/3$ the transition has the opposite effect and brings the system back into the first insulating phase. An analogous behavior appears in the edge modes interpolating between the two highest energy bands, in the case of filling 5/3.

These features have been numerically studied for the tight-binding Hamiltonian of the model using the Kwant software package to evaluate the number of edge modes for an infinite stripe geometry of width 40 whose spectrum has been calculated as a function of k_x. The Chern numbers were instead independently calculated using a discretized version of Eq. (9.17) and dividing the Brillouin zone into 120×120 plaquettes.

The variation of the Chern numbers at the topological phase transition is similar to the one driven by the spin-orbit coupling generated by σ_z in the honeycomb lattice model, as described in [33]. However, in the case analyzed here spin is not a conserved quantity, meaning that different spin species do not have separate Chern numbers. The phase transitions are driven instead by an off-diagonal Rashba coupling.

Finally, the potential (9.12) can be generalized to the anisotropic case:

$$\vec{A} = \frac{2\pi}{3}(0, x)\,\sigma_0 + (q_x\sigma_x, q_y\sigma_y) \ . \tag{9.18}$$

The phase diagram of the anisotropic model at filling 1/3 is shown in Fig. 9.4. The $q_x = q_y$ pattern described before is shown by a gray dotted line, and the corresponding transition points between the two topological insulating phases are shown by two red dots.

For $q_x \neq q_y$ we still observe the presence of three different phases: a topological semimetal phase, characterized by a partial filling of the two lowest bands, and two distinct topological insulating phases, where the first band is completely filled and the second is empty. The insulating phases are characterized by a nonzero Chern number $\mathcal{C}_{-2} = 1, -2$ respectively. Again the topological semimetal phase is distinguished by the topological insulating phases due to the presence of an indirect overlap of the bands; once this overlap disappears, we have a transition between these two regimes and the bulk conductance vanishes. The topological phase transition between the two insulating phases is instead related to a change in the Chern numbers, with parameters q_x and q_y determining the position of Dirac cones appearing in the spectrum at the transition.

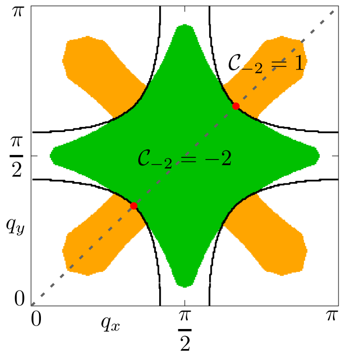

Fig. 9.4: Phase diagram at filling $1/3$ as a function of q_x and q_y for the gauge potential (9.18). The insulating regions characterized by Chern numbers $\mathcal{C}_{-2} = -2, 1$ are shown in green and orange respectively. Uncolored regions correspond to indirect overlap between bands (topological semimetal phase), whereas the black lines show the position of the Dirac cones corresponding to a discontinuity in the Chern number $\mathcal{C}_{-2}$. The red dots represent topological phase transitions at $q = \pi/3, 2\pi/3$ along the diagonal $q_x = q_y = q$.

9.4 Detection of the topological phase transition

Topological phase transitions in complicated systems, such as the one presented in the previous subsection, are hard to detect unambiguously. Several techniques have been proposed to experimentally characterize the topological invariants. Some of them are based on the observation of the edge modes [95], which in our model change both in number and in direction of propagation at the transition points, providing direct evidence for the topological transition. Other viable techniques rely on the possibility of detecting the dynamic response of the bulk under an external force or on other bulk properties [60, 75, 26].

Our approach again consists on taking time-of flight-images which discriminate the inner spin-degree of freedom of the atoms; and which allow a direct measurement of the Chern number of the lowest energy band, once the Fermi level is placed in the first energy gap [6, 32].

In the models analyzed in previous chapters (see Cha. 7 and, for a more complicated but similar rationale, Cha. 8), the Hamiltonian can be written as a 2×2 matrix where the spin and sublattice degrees of freedom completely coincide: it can be shown (see chapter 4) that in the insulating phases the spin (Pontryagin) winding number in the first Brillouin zone coincides with the Chern number of the lowest band and thus with the number of edge states.

In the model considered here instead, $\Phi = \Phi_0/3$ and the Hamiltonian (9.16) is a 6×6 matrix with eigenfunctions that can be generically expressed as:

$$\left|\psi_\lambda(\vec{k})\right\rangle = \sum_{\substack{s=\uparrow,\downarrow \\ x=0,1,2}} c_{\lambda,sx}(\vec{k})\ |s\rangle_{\text{spin}}\ |x\rangle_{\text{lat}}\ , \tag{9.19}$$

where the spin and lattice pseudospin (labeled above as lat) degrees of freedom do not coincide. The wave function ψ_λ is described in the basis obtained by the tensor product of the spin and lattice pseudospin spaces and, due to the effect of the non-Abelian potential, ψ_λ is not simply a direct product state of the form $\left|\varphi_\lambda(\vec{k})\right\rangle_{\text{spin}} \otimes \left|\chi_\lambda(\vec{k})\right\rangle_{\text{lat}}$, but it encodes some entanglement between the two degrees of freedom.

Despite the fact that the Hamiltonian does not define in a direct way a mapping from the Brillouin zone to the Bloch sphere, it is still possible to follow an approach similar to the one in chapter 5 and define a spin winding number over the first Brillouin zone. This is because the spin is a periodic observable in the first Brillouin zone, and therefore a spin winding number can be properly defined and experimentally measured through time of flight imaging [6]. This spin winding number does not coincide with the Chern number defined in (9.17), because the latter requires in its definition a knowledge of the full wave function, not only of the spin part. Nevertheless we will show that the spin pattern of the wavefunctions in the different bands provides, in our model, enough information to detect the topological phase transition.

Focusing on the lowest energy band, we define the spin polarization $\vec{S}(\vec{k})$ in the Brillouin zone in terms of a reduced density matrix by tracing out the lattice orbital degree of freedom:

$$\rho(\vec{k}) = \sum_{x=0,1,2} {}_{\text{lat}}\langle x|\psi_\lambda(\vec{k})\rangle\langle\psi_\lambda(\vec{k})|x\rangle_{\text{lat}}, \tag{9.20}$$

where ρ is the 2×2 matrix representing a mixed state for the spin degree of freedom and depending on the quasi-momentum in the Brillouin zone. If only this lowest energy band is filled and the system is not in a semimetal (gapless) phase, the time of flight images, distinguished by their inner spin state and eventually combined with a rotation of the atomic states, allow for the measurement of the observables given by

$$S_i(\vec{k}) = \mathrm{Tr}_{\text{spin}}\left[\rho(\vec{k})\,\sigma_i\right]\ . \tag{9.21}$$

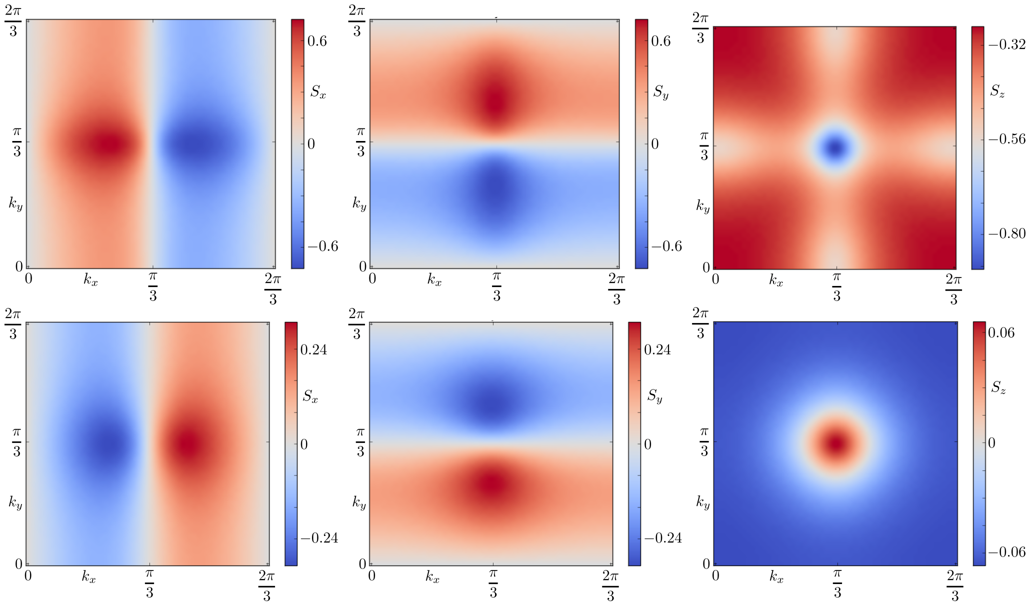

Fig. 9.5: Comparison between the spin polarization at $q = \pi/5$ (top row), which represents the topological insulating phase with $\mathcal{W} = 0$, and $q = 2\pi/5$ (bottom row), which describes the second insulating phase with $\mathcal{W} = -1$. The component S_z of the polarization (third column) behaves very differently in the two cases. For $q = \pi/5$ (as generally for $q < \pi/3$), S_z is negative in the whole Brillouin zone (top right panel), whereas for $q = 2\pi/5$ (as in general for $\pi/3 < q < \pi/2$) the polarization exhibits a skyrmion structure. When $q = 2\pi/5$, the skyrmion interpolates from $S_z \simeq 0.067$ at $\vec{k} = (0, 0)$ to $S_z \simeq -0.067$ at $\vec{k} = (\pi/3, \pi/3)$ (bottom right panel). The S_x and S_y components display opposite signs in the two cases.

The vector $\vec{S}$ is not normalized due to the fact that ρ describes a mixed state. The behavior of the polarization $\vec{S}$ provides a clear indication of the topological phase transition: for $0 < q < \pi/3$ or $2\pi/3 < q < \pi$ the component S_z is negative in the whole Brillouin zone, whereas in the intermediate phase at $\pi/3 < q < 2\pi/3$ (for $q \neq \pi/2$) S_z assumes both negative and positive values (see Fig. 9.5). At $q = \pi/2$, the polarization always lies in the $\hat{x} - \hat{y}$ plane due to the additional symmetry generated by σ_z.

The polarization $\vec{S}$ is independent of the gauge choice for the Abelian potential and is periodic with period $\Delta k = 2\pi/3$ in both the $\hat{x}$ and $\hat{y}$ directions; thus one has to consider a reduced magnetic Brillouin zone with $\vec{k} \in [0, 2\pi/3) \times [0, 2\pi/3)$.

Excluding the point at $q = \pi/2$ (where $S_z = 0$ and our argument fails), the spin polarization along $\hat{z}$ in the phase at $\pi/3 < q < 2\pi/3$ has a single skyrmion in the reduced Brillouin zone (a configuration in which the spin polarization entirely covers the Bloch sphere once moving in the reduced Brillouin zone). For $\pi/3 < q < \pi/2$ this skyrmion is centered at $\vec{k} = \{\pi/3, \pi/3\}$, whereas for $\pi/2 < q < 2\pi/3$ it is centered at $\vec{k} = \{0, 0\}$, meaning that the skyrmions appear at the position of the Dirac points at $q = \pi/3$ and $q = 2\pi/3$, respectively.

The winding number of the spin polarization in the reduced Brillouin zone (rBZ) provides a good topological invariant that plays the role of an order parameter for these transitions and reflects the presence of a skyrmion in momentum space. In particular this winding number $\mathcal{W}$ is defined as the integral of the spin curvature

$$c(\vec{k}) = \frac{1}{4\pi}\frac{\vec{S}}{|\vec{S}|^3}\cdot\left(\partial_{k_x}\vec{S}\times\partial_{k_y}\vec{S}\right) \tag{9.22}$$

and it reads:

$$\mathcal{W} = \frac{1}{4\pi}\int_{\text{rBZ}} d^2k\,\frac{\vec{S}}{|\vec{S}|^3}\cdot\left(\partial_{k_x}\vec{S}\times\partial_{k_y}\vec{S}\right)\,, \tag{9.23}$$

where $|\vec{S}|$ normalizes the polarization.

The winding number $\mathcal{W}$ is 0 for $0 < q < \pi/3$ and for $2\pi/3 < q < \pi$, whereas $\mathcal{W} = -1$ in the other phase (with the exception of the point at $q = \pi/2$). If we want to consider the full Brillouin zone we must multiply this winding number by 3, and, at the phase transitions, we recover the same discontinuity observed for the Chern number $\mathcal{C}_{-2}$. We find that $\mathcal{C}_{-2} = 3\mathcal{W} + 1$.

The discrepancy between the two indices cannot be directly related to a contribution to the winding number from the lattice degree of freedom: if we trace out the spin degree of freedom instead of the lattice one and try to calculate, with an analogous procedure, the polarization obtained by the new 3×3 reduced density matrix, its winding number is constantly zero and does not affect the difference $\mathcal{C}_{-2} - 3\mathcal{W}$. This unequivalence can be understood even in the absence of non-Abelian flux: a net magnetic field implies that the relevant correlators are non-local in momentum space [98].

At the experimental level one may be able to estimate $\mathcal{W}$ through a discretization of formula (9.23), based on the division of the time of flight images in small domains, corresponding to a discretization of the Brillouin zone [6, 32]. It is important to realize that, while experimental time of flight imaging can be well approximated by a continuous set of data, a discretized approach is relevant for analyzing the signal which can be obtained from finite size lattices. The following discussion can therefore be understood as modeling either limitations of the measurement procedure or finite size effects in realistic setups.

In order to illustrate the protocol to compute $\mathcal{W}$, let us divide the reduced Brillouin zone into $L \times L$ plaquettes that we label by discrete quasimomenta (p_x, p_y), in units of $\delta = \frac{2\pi}{3L}$. For each plaquette it is possible to estimate the vector $\vec{S}(p_x, p_y)$ from the experimental data (eventually repeating the experiments many times to acquire a sufficient statistics). The spin curvature $c(\vec{k})$ in (9.22) can be approximated by:

$$\begin{aligned} 2\pi\, c(p_x, p_y) = {} & \arctan\left[\frac{\vec{N}(p_x,p_y)\cdot\left(\vec{N}(p_x+\delta,p_y)\times\vec{N}(p_x,p_y+\delta)\right)}{1+\vec{N}(p_x,p_y)\cdot\vec{N}(p_x+\delta,p_y)+\vec{N}(p_x,p_y+\delta)\cdot\vec{N}(p_x+\delta,p_y)+\vec{N}(p_x,p_y)\cdot\vec{N}(p_x,p_y+\delta)}\right]+ \\ & +\arctan\left[\frac{\vec{N}(p_x+\delta,p_y+\delta)\cdot\left(\vec{N}(p_x,p_y+\delta)\times\vec{N}(p_x+\delta,p_y)\right)}{1+\vec{N}(p_x+\delta,p_y+\delta)\cdot\vec{N}(p_x+\delta,p_y)+\vec{N}(p_x,p_y+\delta)\cdot\vec{N}(p_x+\delta,p_y)+\vec{N}(p_x+\delta,p_y+\delta)\cdot\vec{N}(p_x,p_y+\delta)}\right], \end{aligned} \tag{9.24}$$

where $\vec{N}$ is the normalized polarization vector $\vec{N} = \frac{\vec{S}}{|\vec{S}|}$.

The two terms in (9.24) correspond to (half) the solid angles defined respectively by the (ordered) triplets of vectors

$$\left\{\vec{N}(p_x, p_y), \vec{N}(p_x + \delta, p_y), \vec{N}(p_x, p_y + \delta)\right\}$$

and

$$\left\{\vec{N}(p_x + \delta, p_y + \delta), \vec{N}(p_x, p_y + \delta), \vec{N}(p_x + \delta, p_y)\right\}.$$

By adopting this approximation, $\mathcal{W}$ results from the sum of all the $c(p_x, p_y)$'s in the rBZ:

$$\mathcal{W} \sim \sum_{(p_x,p_y)\in \mathrm{rBZ}} c(p_x, p_y)\,. \tag{9.25}$$

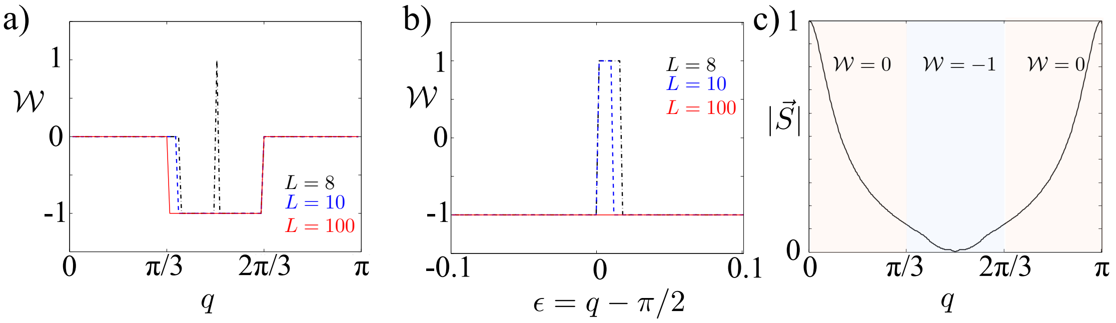

Fig. 9.6: Effects of discretization on the relative error in the computation of the winding number. *a):* Estimated spin winding number $\mathcal{W}$ for various values of the discretization L: $L = 100$ (solid red line), $L = 10$ (dashed blue line) and $L = 8$ (dashed-dotted black line). The finer grid ($L = 100$) reproduces almost exactly the theoretical value, whereas coarser grids feature deviations at the transition points (mainly at $q = \pi/3$ because of the relative positions of the grid and the skyrmion) plus a significative error at the maximally entangled $q = \pi/2$ point. *b):* Winding number computed at $q = \pi/2 + \epsilon$ for different discretizations. *c):* The minimum of the norm of the polarization vector $|\vec{S}|$ as a function of q. This minimum is reached in the skyrmionic region, showing that the detection of the non-trivial winding number requires more statistical power. In particular, at $q = \pi/2$ the norm vanishes at the skyrmion core, rendering the measurement protocol useless at that particular point.

Since the obtained value for $\mathcal{W}$ is generally not an integer, as it must be, the relative error is easily deducible and it is smaller than $1 \cdot 10^{-3}$ for a 5×5 discretization at $q = \pi/5$ and $q = \pi/4$, corresponding to the trivial phase where $\mathcal{W} = 0$; the error is also small ($< 1 \cdot 10^{-3}$) at points in the non-trivial phase away from the transition, such as $q = 2\pi/5$. However, there are a couple of error-prone regions where a finer discretization of the reduced Brillouin zone helps to correctly determine the topological nature of the state. In particular the accuracy decreases both around the phase transitions, where the skyrmion might be overlooked by a coarse discretization (see Fig. 9.6a), and close to $q = \pi/2$ (see Fig. 9.6b), where the partial density matrix approach fails because the orbital and pseudospin degrees of freedom become maximally entangled and the S_z component of the spin vanishes. The main contribution to the total winding number is indeed obtained from the central region of each skyrmion, where the gradient of $\vec{N}$ is larger. Therefore one has to ensure sufficient sampling close to the skyrmion core, in order to avoid unwanted large discretization errors.

We also note that, in the presence of a skyrmion, the norm of the polarization is much smaller than unity (see Fig. 9.6c) due to a strong mixing with the lattice degree of freedom: for example at $q = 2\pi/5$ the component S_z in the north and south poles appearing at $\vec{k} = (0, 0)$ and $\vec{k} = (\pi/3, \pi/3)$ is approximately ± 0.067 (see Fig. 9.5). Thus the difference in the number of atoms between the two species at the center of the skyrmion is of the order of 10%. This example is relevant since $q = 2\pi/5$ is close to the optimal point in which S_z is maximized in the center and there we find the maximal extension of the core of the skyrmion (defined as the neighborhood of the north pole where $S_z > 0$). In general the dimension of the core is quite reduced and, in order to avoid excessive discretization errors, we adopted the approximation in Eq. (9.24), which is finer than the one used in chapter 7 and better fulfills the accuracy requirements of our model.

As a final remark we point out that the detection of the phase transition by the spin winding number works if only the lowest band is occupied. In the semimetal phase also the second band contributes to the measured spin winding number, thus spoiling the final result (in [32] the behavior of the spin winding number is investigated also in the semimetal regime where two different bands are involved).

9.5 Conclusions

We analyzed a model of two-component fermions on a square optical lattice with tunneling amplitudes determined by a non-Abelian gauge potential with both a magnetic field and a translationally invariant SU(2) non-Abelian term. By choosing a magnetic flux different from $\Phi_0/2$ we considered a setup with broken time-reversal symmetry and showed that the non-Abelian term drives the system across topological phase transitions. In particular we investigated the case of $\Phi = \Phi_0/3$, where the system presents six energy bands, and discussed its phase diagram at filling 1/3, which is characterized by a topological semimetal and by two different topological insulating phases, with edge states differing in number and in propagation direction across the topological phase transition.

The topological insulating phases can be distinguished by looking at the spin polarization in momentum space, estimating the spin winding number from time of flight absorption images. The winding number method provides a clear diagnostics for the characterization of the topological phase transition even though the spin is not a conserved quantity of the system.

The single-particle properties of this system may constitute the basis for the study of topological phase transitions also in the presence of interactions. In particular, in the limit $q \to \pi/2$ the lowest band in this model has an extremely flat profile which constitutes a fundamental requirement to engineer Chern insulators, able to mimic fractional quantum Hall physics [72]. Even though in this limit measuring the spin winding number might become more difficult, the fact that it remains a topological invariant would be extremely useful in characterizing the system. Furthermore, introducing a repulsive interaction may lead to the regime of topological Mott insulators [25] where the presence of the spin degree of freedom may enrich the phase diagram of such interacting models, also due to the possibility of introducing spin-dependent interactions.

10. MEASUREMENT OF SPATIAL DISTRIBUTIONS OF ENTANGLEMENT IN OPTICAL LATTICES

10.1 Summary

This chapter is a change in the melody, if not the theme, of the rest of the thesis. The main goal is common: to construct a robust measurement protocol in order to measure an elusive non-local property of our state. Here, too, we are interested in the practical details of an optical lattice implementation, and perform theoretical and numerical studies to estimate the effect of typical noise sources on the application of our measurement scheme.

This chapter deals with how to detect genuine multipartite entanglement in a cloud of atoms. The entanglement class which can be thus detected is very particular: we are interested in creating and characterizing graph states, which are the essential resource for measurement-based quantum computation (MBQC - see Ref. [42]). We also propose to measure this entanglement class in an unusual manner: most entanglement measurement experiments try either to start from the control of individual quantum systems (photons, ions, atoms,...) and scaling the system up, or studying collective degrees of freedom of a large number of atoms. Here, however, we follow an intermediate approach, by which it is possible to gain local information about a very large entangled state.

In particular, we study the entangled states that can be created in bipartite two-dimensional optical lattices loaded with ultracold atoms. Most importantly for practical purposes, it is shown that by using only two sets of measurements it is possible to compute a set of entanglement witness operators distributed over arbitrarily large regions of the lattice; and then these witnesses can be used to produce two-dimensional plots of the entanglement content of these states. We also discuss the influence of noise on the states, and characterize these effects by performing numerical simulations in our particular choice of geometry.

This chapter is structured as follows: first, we give a brief introduction to the class of states we want to build and measure, after which we particularize the setup by choosing a particular geometry. We present observables that characterize the state and act as entanglement witnesses in section 10.3, in which we also face the main difficulties associated to this method. We find that even under decoherence states useful for quantum computation can be found, and analyse simple observables that bound the fidelity of the state. Then, Sec. 10.4 reviews the experimental techniques available to create graph states in optical lattices. The additional difficulties which the measurement protocol faces in an optical lattice setup are analyzed theoretically in section 10.5. Finally, in Sec. 10.6, we perform numerical simulations of a cluster state subject to different noise sources, demonstrating that the entanglement witness is capable of detecting those errors.

10.2 Graph states

Graph states are a particular kind of genuine multipartite entangled state ([17]) which can be most intuitively understood by its construction: we assume that we start with completely unentangled qubits and then choose some 2-qubit maximally entangling gate which we apply to pairs of qubits. The qubits can be considered "vertices" of a graph where the "links" are given by the application of the entagling gate. Graph states have been proposed to perform universal quantum computation just based on measurements (MBQC) and have intriguing properties. While some of the most useful characteristic of graph states will be outlined in section 10.3, a recommended complete review on this topic can be found in Ref.[42]). Along this chapter, we will use the terms qubit, vertices and atoms rather interchangeably.

An important peculiarity of the graph states we will deal with in this chapter is that they are bipartite, i.e. one can choose two sets of atoms A and B which cover all vertices but do not have any links within them. This fact will be of key importance in applying the results of section 10.3.3. In particular, we will perform numerical simulations to illustrate the protocol in a honeycomb lattice of atoms, as shown in Fig. 10.1.

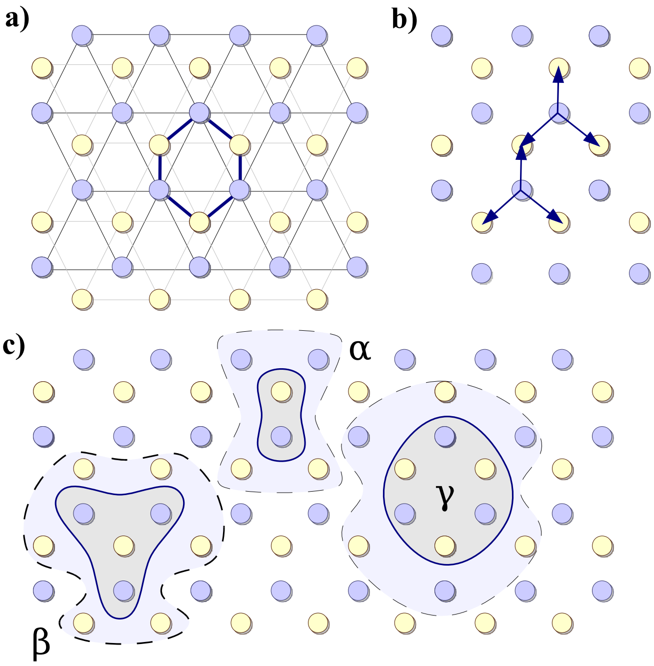

Fig. 10.1: (a) We work with two subsets of qubits (here coloured in yellow and blue) trapped in two independent triangular sublattices, which together form a honeycomb lattice. (b) A graph state can be generated moving one of the sublattices along three different directions. (c) In this work we analyze the properties of localizable multipartite entanglement in small sets of 2 (α), 4 (β), 6 (γ), or more spins. Each of these regions, Ω, is connected with its boundary, $\partial\Omega$, by two-qubit unitaries.

To fix ideas we will assume that the entangling operation between atoms in different sublattices is a CZ gate, $U_{CZ} = \exp\left(-i\frac{\pi}{4}\sigma^z_{\mathrm{A}}\sigma^z_{\mathrm{B}}\right)$. After three parallel sets of operations, beginning with a product state, $(|0\rangle + |1\rangle)^{\otimes N}$, we will arrive at a graph state

$$|G_{\hexagon}\rangle \sim \prod_{i\in A}\prod_{j\in\mathcal{N}(i)} U_{CZ}^{(i,j)}\,(|0\rangle+|1\rangle)^{\otimes N_A+N_B}\,, \tag{10.1}$$

where A and B denote the sublattices and $\mathcal{N}(i)\subset B$ is the set of nearest neighbors to the potential well $i\in A$ Note that if instead of using the control-phase one implements a control-NOT, $U_{\mathrm{CNOT}} = (1+\sigma^z_{\mathrm{A}})\,\mathbb{1}_B - (1-\sigma^z_{\mathrm{A}})\,\sigma^x_{\mathrm{B}}$, where the B-type atoms absorbs the parity of its neighbors, we obtain what we call a "parity" multipartite entangled state

$$|P_{\hexagon}\rangle \sim \prod_{i\in A}\prod_{j\in\mathcal{N}(i)} U_{\mathrm{CNOT}}^{(i,j)}\,(|0\rangle+|1\rangle)^{\otimes N_A+N_B}\,. \tag{10.2}$$

10.3 Entanglement witnesses

10.3.1 Global fidelity of graph states

All the states that we can create using the previous operations belong to the family of stabilizer states. In both cases we have a complete set of N_A+N_B local observables, the stabilizing operators, g_i, that may take values $\{-1,+1\}$, and for which the states $G_{\hexagon}$ and $P_{\hexagon}$ are eigenstates with eigenvalue $+1$ on all sites [1]. For instance, in the case of the graph state we have

$$g_i\,|G_{\hexagon}\rangle = +1\,|G_{\hexagon}\rangle\,, \quad \forall i\in A\cup B. \tag{10.3}$$

with the stabilizing operators $g_i = \sigma^x_i \prod_{j\in\mathcal{N}(i)}\sigma^z_j$. In general, given a set of lattice sites, Ω, we can construct a projector onto a stabilizer state containing those sites

$$P_\Omega = \prod_{i\in\Omega}\frac{1}{2}(1+g_i). \tag{10.4}$$

In theory we can use this projector to compute the fidelity of our experimentally realized state, ρ, which is probably mixed, with respect to the objective $G_{\hexagon}$ or $P_{\hexagon}$,

$$F_{A\cup B} = \mathrm{tr}(P_{A\cup B}\,\rho), \tag{10.5}$$

where the region under study now encloses the A and B sublattices. However in practice this is already impossible for a few qubits, since the evaluation of F_Ω requires us to measure $2^{N_A+N_B}$ different observables coming from all possible products of the g_i operators. The difficulty of this task seems to be tantamount to performing a full tomography of the mixed state ρ.

---

[1] The g_i operators are the generators of the so-called stabilizer group [37].

10.3.2 Localizable fidelity

Instead of following this very complicated route, we will focus on two simpler questions, which are intimately related: (i) a notion of local fidelity to the stabilizer state and (ii) the existence and detection of genuine multipartite entanglement [3] in the lattice. In both cases we can extract a number, let it be a fidelity or the expectation value of an entanglement witness, $F(i)$ or $W(i)$, which is distributed over the 2D lattice of sites. With those numbers we can study the distribution of entanglement and how much our state has been affected by noise or decoherence.

Our notion of "localizable fidelity" builds on the fact that given a simply connected set of sites, Ω, and a perfect graph state, $|G_{\bigcirc}\rangle$, we can extract another perfect graph state in that region. One way to achieve this is measuring the boundary qubits, $\partial\Omega$, [See Fig. 10.1c] and, depending on the outcome of those measurements, performing phase gates on the qubits that were immediately connected to them. An alternative but completely equivalent way is to disentangle the boundary with the same two-qubit unitaries we used to build the state

$$\rho_\Omega = \mathrm{tr}\left(\prod_{i\in\partial\Omega}\prod_{j\in\mathcal{N}(i)} U_{CZ}^{(i,j)}\rho_{A\cup B}\right). \tag{10.6}$$

The most important idea is that this procedure still can be applied if the initial state of the atomic ensemble is mixed, $\rho_{A\cup B}$, due to decoherence. In this case the fidelity of the final state is related to the same observable that we found before, that is

$$F_\Omega = \langle G_\Omega|\,\rho_\Omega\,|G_\Omega\rangle = \mathrm{tr}\left(P_\Omega\rho_{A\cup B}\right), \tag{10.7}$$

the fidelity of the final state only depends on how close $\rho_{A\cup B}$ is to the eigenstates of the stabilizing operators that cover the region **and** the boundary, $\Omega\cup\partial\Omega$. The final observation is that the fidelity F_Ω gives us not only local information about how close our state is to the graph state, but it is also a witness for genuine multipartite entanglement in that region, $W_\Omega = \frac{1}{2}\mathbb{1} - P_\Omega$ [93].

10.3.3 Optimized witnesses

However, even if $\langle W\rangle < 0$ detects entanglement, the evaluation of this quantity seems to require a number of measurements that increases exponentially with the number of qubits. We thus need another ingredient, which is obtained by writing the fidelity as a product of two operators constructed from stabilizing operators corresponding to different sublattices, $P_\Omega = P_{\Omega\cap A}P_{\Omega\cap B}$, and introducing a new operator [92]

$$\tilde{P}_\Omega = P_{\Omega\cap A} + P_{\Omega\cap B} - \mathbb{1} \leq P_\Omega, \tag{10.8}$$

This equation can be readily verified in the basis that diagonalizes both $P_{\Omega\cap A}$ and $P_{\Omega\cap B}$, where the eigenvalues of the projectors can only be 0 or +1.

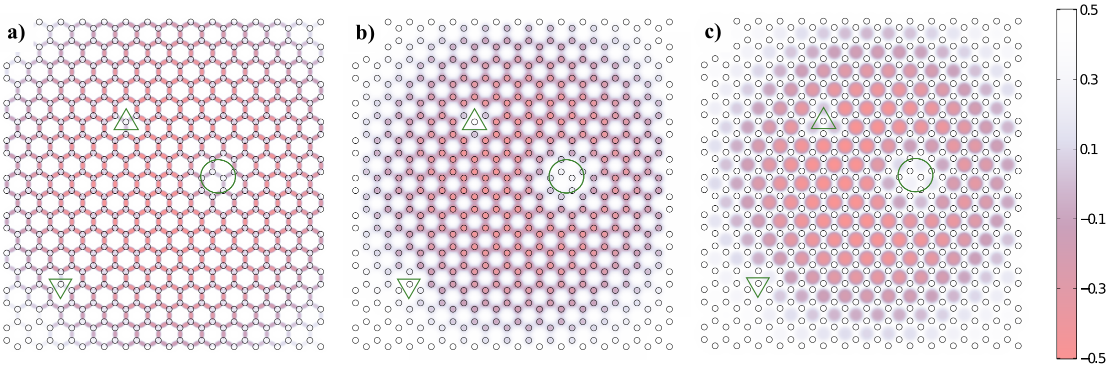

Fig. 10.2: Two-dimensional distribution of the entanglement witnesses for (a) two, (b) four and (c) six particle arrangements, α, β and γ from Fig. 10.1c, respectively. The value of the witness is color coded on the (a) links, (b) atoms or (c) center of the plaquette. A a negative value of the witness (red) denotes existence of bi- or multi-partite entanglement. All pictures present the same defects, consisting on two empty sites (triangles), atoms subject to strong dephasing (circle), and an increase of phase gate errors towards the edges of the trap.

This observable provides a lower bound for the fidelity

$$F_\Omega \geq \langle \tilde{P}_\Omega \rangle, \tag{10.9}$$

and can be used to construct an entanglement witness

$$\tilde{W}_\Omega = \frac{1}{2}\mathbb{1} - \tilde{P}_\Omega. \tag{10.10}$$

The advantage is that now the quantities $\langle P_{\Omega\cap A}\rangle$ and $\langle P_{\Omega\cap B}\rangle$ can be extracted from just two settings of measurements. In particular, for the graph state one such expectation values

$$\langle P_{\Omega\cap A}\rangle = \left\langle \prod_{i\in\Omega\cap A} \frac{1}{2}\left(1 + \sigma_i^x \prod_{j\in N(i)} \sigma_j^z\right)\right\rangle, \tag{10.11}$$

is obtained measuring σ^x in all A atoms ($i \in \Omega \cap A$) and σ^z in the B ($j \in N(i)$), while the other expectation value is obtained with the opposite measurement basis. Note also that postprocessing the **same** set of measurement results we can compute the values $\langle \tilde{P}_\Omega \rangle$ for any region Ω, which allows us to produce two-dimensional displays of the distribution of localizable fidelity or the multipartite entanglement witness.

10.4 Experimental generation of stabilizer states

The original method for creating graph states with neutral atoms was based on filling state-dependent lattices with one atomic species and using controlled collisions [64, 47]. In contrast, we propose to develop our ideas building on the experimental setup from Ref. [16, 55], which traps two different species of atoms in two coexisting optical lattices, one of which can be moved. This setup combines a diffraction mask with a powerful microscope objective, which projects two similar triangular lattice patterns on its focal plane. Using two light beams with different frequencies, the experiment may trap lithum and cesium atoms in two independent lattices that can be moved at will along the plane that confines the atoms. As shown in Fig. 10.1a, we can contemplate the Cs and Li arrangements as the triangular sublattices of a larger honeycomb lattice where each Cs atom is surrounded by three Li atoms, and vice versa; and each atom acts as one qubit. Since our lattice is bipartite by construction entanglement can be created using a small number of steps, equal to the coordination number of the full lattice. Continuing with this example, one has to move one sublattice three times so that each Cs atom approaches each of its neighboring Lithium atoms [Fig. 10.1b], suffering a controlled collision [64] or an engineered interaction [16]. A fundamental difference with the previous setups is that the sublattice now moves as a whole, regardless of the internal states of the atoms. If the lattices are very deep and the atom-atom interaction is strong enough, this can be done with great precision.

Naturally, using a particular experimental setup adds characteristic forms of noise to the measurement of the stabilizer operators, which may result in failure to pass the witness test. In order to quantify how typical noise sources in optical lattice setups affect the theoretical results, we will perform a theoretical study of the effect of the noise and numerical simulations based on our chosen lattice geometry in the following sections.

10.5 Positive maps and Noise sources

Any physical operation on a quantum state must be a trace preserving positive map, which maps density matrices into density matrices. Furthermore, such operators admit a unique decomposition using a set of operators

$$\varepsilon(\rho) = \sum_k A_k \rho A_k^\dagger,$$

with the property $\varepsilon(\mathbb{1}) = \mathbb{1}$.

This description admits a generalization to expectation values. In other words, we also have a positive map description in the Heisenberg picture, where operators/observables and not states are changed. Using the definition $\langle \Theta \rangle = \mathrm{tr}\{\Theta\rho\}$, the change in the expectation value can be expressed as

$$\langle \Theta \rangle_{\varepsilon(\rho)} = \mathrm{tr}\{\Theta \sum_k A_k \rho A_k^\dagger\} = \langle \tilde{\varepsilon}(\Theta) \rangle$$

where $\tilde{\varepsilon}(\Theta) = \sum_k A_k^\dagger \Theta A_k$.

We now want to estimate the effect of different positive maps on our entanglement witnesses. We will first focus on local error sources. It is important to observe that the expected values we want to calculate are of the general form

$$P = f(\sigma^{\alpha}_{i\in A}, \sigma^{\beta}_{i\in B}), \quad \alpha, \beta \in \{x, z\},$$

that is, they are functions of the same observables on each sublattice. This means that under local error sources the following relation applies:

$$P' = f\left(\tilde{\varepsilon}(\sigma^{\alpha}_{i\in A}), \tilde{\varepsilon}(\sigma^{\beta}_{i\in B})\right).$$

Therefore it suffices to compute how the operators change under the different local error sources. In each case, the decoherence channel will change the effective value of the stabilizer expectation value.

10.5.1 Dephasing

In this noise source we have an average over random phases

$$\tilde{\varepsilon}(\sigma^x) = \int e^{-i\phi\sigma^z} \sigma^x e^{i\phi\sigma^z} p(\phi) d\phi.$$

If the distribution $p(\phi)$ is symmetric, then

$$\tilde{\varepsilon}(\sigma^x) = \int \left[\cos(2\phi) + i\sin(2\phi)\sigma^z\right] \sigma^x p(\phi) d\phi = (1-\epsilon_i)\sigma^x,$$

with some error factor ϵ_i. Since the σ^z operators are not affected, it is legitimate to say that the map induces a global change in the expected value $g_i \to (1-\epsilon_i) g_i$.

10.5.2 Particle loss

This positive map has the form

$$\epsilon(\rho) = (1-p)\rho + p|0\rangle\langle 0|,$$

which we can also write in Kraus form using the operators

$$A_0 = (1-p)\mathbb{1}, A_1 = p|0\rangle\langle 0|, A_2 = p|0\rangle\langle 1|.$$

This means that the operators transform as

$$\tilde{\varepsilon}(\Theta) = (1-p)\Theta + p\langle 0|\Theta|0\rangle\mathbb{1}.$$

Thus the stabilizer operators are modified

$$g_i \to (1-p)^N \sigma^x_i \prod_{j\in N(i)} \sigma^z_j + g_i^{\perp},$$

where N is the number of qubits in the stabilizer operator (4 in our case for the honeycomb lattice) and the $g_i^{\perp}$ contain terms that are going to vanish because they can be written in the form $g_i \sigma^x_i \prod_{j\in N'(i)} \sigma^z_j$ or $g_i \prod_{j\in N'(i)} \sigma^z_j$ with $N'(i) \subseteq N(i)$, so that their expectation values are zero.

10.5.3 Errors in the gates

We can proceed similarly though some subtleties are to be taken into account. First of all we realize that instead of transforming the state we can transform the stabilizer operators which appear in the expectation value

$$g_j \to e^{-i\sum_{k\in N(j)}\epsilon_{jk}\sigma_j^z\sigma_k^z} g_j e^{+i\sum_{k\in N(j)}\epsilon_{jk}\sigma_j^z\sigma_k^z}.$$

It can be seen that this is equivalent to performing the same transformation only on the σ_j^x operator

$$\sigma_j^x \to \prod_k \left[\cos(2\epsilon_{jk}) + i\sin(2\epsilon_{jk})\sigma_j^z\sigma_k^z\right]\sigma_j^x,$$

Note that since we only have σ^x operators in one sublattice and σ^z on the other, the phases that we have here are uncorrelated among different σ^x operators. Furthermore, any term that contains a σ^z operator vanishes once we take expectation values, which means that we can replace $\sigma_j^x \to (1-\epsilon_j)\sigma_j^x$, where $\epsilon_j = \prod_k \int \epsilon_{jk} p_{jk}(\epsilon_{jk}) d\epsilon_{jk}$. This shows that the outcome is a global reduction of the stabilizer expectation value.

10.6 Simulations

This section features a numerical simulation of a realisation of our method in an experiment taking possible practical sources of error into account. We have studied the degradation of the expectation value of the witness $\tilde{W}_\Omega$ given in Eq. (10.10). In general it is not possible to compute easily the change of $\langle P_\Omega\rangle$, but we will take advantage of the facts that the witness is the sum of two functions of stabilizing operators corresponding to *different* sublattices and that for our sources of noise these expectation values have simple expressions, such as $\langle P_{\Omega\cap A,B}\rangle = \prod_{i\in\Omega\cap A,B}(1+\langle g_i\rangle)/2$, in which only the expectation values of isolated stabilizers appear, $\langle g_i\rangle$. We have considered various types of noise, as detailed in the previous section, and use the quantum channel formalism to compute the changes in $\langle g_i\rangle$.

(i) Dephasing, which is due to fluctuations in the energy levels of the atoms due to external fields, $\epsilon_j(\rho) = \int d\theta_j \exp(-i\sigma^z\theta_j)\rho\exp(i\sigma^z\theta_j)p(\theta_j)$. This map is repeated on all sites, with site dependent uniformly distributed random phases in $[-\epsilon_j, \epsilon_j]$, degrading the stabilizing operator $\langle g_i\rangle \to \langle g_i\rangle \prod_{i\in\Omega}\sin(2\epsilon_i)/2\epsilon_i$.

(ii) Imperfections in the gates that entangle pairs of sites, $U_{CZ}^{(j,k)} \to U_{CZ}^{(j,k)}\exp(i\theta_{jk}\sigma_j^z\sigma_k^z)$, where θ_{jk} are again random variables, uniformly distributed in $[-\epsilon_{jk}, \epsilon_{jk}]$. This error introduces a factor in the expectation value of the stabilizing operators, $\langle g_i\rangle \to \langle g_i\rangle \prod_{j\in N(i)}\frac{1}{2}(1+\sin(2\epsilon_{ij})/2\epsilon_{ij})$, plus other terms that do not contribute to the witness (10.10).

(iii) Atom loss, which introduces a new state in the lattice, the hole $|h\rangle$. In practice, it can be described by $\epsilon_{\mathrm{AL}}(\rho) = (1-p)\rho + p\,|0\rangle\langle 0|$.

(iv) Spontaneous emission $\epsilon_{\mathrm{SE}}(\rho) = (1-p)\rho + p\,|0\rangle\,\langle 0|\,.$

(v) The completely depolarizing channel $\epsilon_{\mathrm{DP}}(\rho) = (1-p)\rho + \frac{p}{2}\mathbb{1}$.

The last three sources of error have the same effect, $\langle g_i\rangle \to (1-p)\langle g_i\rangle$.

With these types of noise and decoherence we studied the evolution of our witness operators and the overall description of a potential experiment using them. The results are shown in Figs. 10.2a-c, where we plot the values of $\tilde{W}_\alpha, \tilde{W}_\beta$ and $\tilde{W}_\gamma$, interpolated using smooth functions that are centered and cover the affected regions, α, β and γ, of two, four and six qubits. The result is a two-dimensional map of the entanglement content, where the value of the witness is color-coded either (a) on the link between two atoms, α, (b) on the central atom and the star surrounding it, β, or (c) on the center of the six-atom plaquette, γ. In these particular plots we have combined all sources of decoherence, making some of them more relevant in different regions of the lattice. We have introduced a region of atoms subject to strong dephasing induced by a focused laser, covering the area marked by a circle. We have also emptied two sites, surrounded by a triangle. These empty holes are numerically equivalent to having spontaneous emission with 100% probability. Finally, we have assumed that the phase gate is 100% accurate in the center of the lattice and acquires a 10% error at the boundary of the lattice.

We already appreciate interesting features in these simple simulations. The first one is that bipartite entanglement is less affected by noise than multiqubit arrangements. While we can reconstruct a Bell state close to the boundary with an 80% error, the four- and six-qubit states only have an appreciable value of the witness when the CZ gate is above 90% fidelity. The second feature is that the effect of local errors remains local. The sites, bonds and plaquettes that share one or more qubits with the regions affected by atom loss or strong decoherence (circle and triangle in the plot) have positive values of the witness and do not have significant entanglement. However, one site or plaquette away from the region of influence of those defects, the witnesses recover their large negative value.

10.7 Conclusions

This chapter has presented a simple scheme for detecting bipartite and multipartite entanglement in two-dimensional lattices with ultracold atoms. The present study admits a straightforward generalization not only to other bipartite lattice setups, such as square lattices, but also to other interaction schemes (U_{CNOT}), or to displacing each Cs atom not three, but one or two times. Further work on how this protocol might be useful in characterizing states for fault-tolerant QC and simple surface codes can be found in Ref.[50].

We must remark that our scheme only uses the fact that the lattice is bipartite and that it is possible to simultaneously measure the state of all lattice sites in each sublattice independently. In particular, while we have focused on a two-species setup [16, 55], exactly the same protocols and measurement schemes can be used using the state-dependent optical lattices in previous experiments [64], combined with the new optics that allows imaging individual lattice sites [14]. The only difference is that since we do not have different atoms on different sublattices, the measurement protocol has to be preceded by a global and local rotation of one sublattice to change its measurement basis. This is not too complicated and can be done using two counterpropagating laser beams in an optical lattice configuration, such that their maxima of intensity concide with just one sublattice.

This proposal represents the first experimentally realizable scheme for mapping out the entanglement distribution and fidelity of a very large many-body correlated state. It also opens the path for the experimental detection of very large cluster states, a task which so far was not achievable using ultracold atoms in optical lattices, but which becomes possible for ongoing experiments using two species of atoms and holographically generated trapping potentials [16]. In particular, it is important to remark that the family of graph states in honeycomb lattices is a universal resource for measurement-based quantum computation and that this scheme can be used to isolate regions of high fidelity in such resources.

11. SUMMARY AND OUTLOOK

11.1 Summary of results

This thesis has addressed the possibility of characterizing and detecting directly non-local properties of bidimensional atomic clouds. As already mentioned, the main motivations for this proposals arise from the field of quantum information and quantum simulations. The main results of this thesis are listed below, in an order and structure that closely, but not exactly, resembles the order of chapters in this thesis:

- **A complete tunable Dirac Hamiltonian can be feasibly engineered in a 2D optical lattice.**

  We have reviewed the way a family of tight-binding models with massive particles can give rise to low-energy theories of Dirac masless fermions. The relationship between all possible (non-interacting) terms and the tunable microscopic parameters is explained. The specific characteristics of the setup are detailed and quantified, in order to make a full simulation proposal. Finally, a few methods of measurement are put forward, which depend on the characteristics of the particular experiment, and which pave the ground for more complicated simulations in similar setups.

- **The topological order of a Chern insulator can be measured by a time-of-flight experiment**

  We have shown that a two-band Chern insulator can be implemented and detected in an optical lattice experiment. A winding number can be computed from time-of-flight images of the cloud, which is equivalent to the Chern number. We have checked numerically that the detection procedure is completely robust under the inhomogeneities and temperatures typical of optical lattice experiments, as it might be expected from an integer-valued topological invariant.

- **The Chern number of a composite system of pseudospins can be exactly measured from partial winding numbers.**

  We have proved the Chern number of a 4x4 translationally invariant Hamiltonian can be decomposed as the sum of the Berry phases -winding numbers- of two pseudospin partitions. For the proof to hold, it is required that these partitions are nowhere maximally entangled - which sets a strong restriction of the choice of bipartitions. In general, this restriction will imply that the bipartition is motivated by some symmetry of the problem. Moreover, and building on the previous result, this means that the Chern number of such a composite system can also be measured in a time-of-flight experiment: we show that a remarkable example of the power of this method can be found in a proposal to measure Majorana zero modes in a fully described optical lattice experiment.

- **The winding number can be measured to detect phase transitions in systems with more degrees of freedom.**

  We have built a tight-binding model which features Abelian and non-Abelian potentials on massive fermions. Measurements on the spin degree of freedom alone are sufficient to construct a winding number which changes along a non-Abelian phase transition, as it is shown numerically. In line with the intuition provided by the last chapter, the information that can be extracted from this partial measurements critically depends on the breaking of relevant symmetries of the problem.

- **Genuine multipartite entanglement can be locally measured in graph states.**

  We have shown that the local fidelity of a graph state can be measured in a simple model of qubits in a bipartite lattice. More importantly, this fidelity is a genuine multipartite entanglement witness that can be computed for arbitrary regions, with just two sets of measurements. We have provided numerical evidence that the protocol works for various typical sources of noise in optical lattice experiments. Although the measurements are in themselves destructive, the method is useful both as a means to certify the presence of entanglement and as a calibration tool for any setup which aims at building large graph states.

11.2 Outlook

This section will put together all the possible research directions that have been suggested in the body of the thesis, plus comment on some more speculative ideas that might become relevant research directions in the field, or else be totally useless.

One of the main questions that this thesis puts forward, and which is also at the core of the field of quantum simulations, is how to compute and characterize the effect of interactions between particles. For most kind of problems, and particularly problems of fermions in a two-or-higher dimensional lattice, classical numerical methods are too costly or directly fail. However, characterization of such problems may be of great value: exotic phases of matter with anyonic excitations, topologically-protected Majorana zero modes or even the secrets of high-Tc superconductivity might be found in that complicated realm.

This thesis has presented a new tool for this challenge: an observable winding number that can be computed through routine time-of-flight imaging in optical lattice experiments. This topological invariant is not only equivalent to the Chern number in its simplest case, but chapters 5 and 8 have shown that it can also be equivalent to the Chern number in composite cases, with the free bonus of providing information about the entanglement content between bipartitions. If any experiment is able to change the choice of bipartitions with freedom, this provides direct access to the scaling properties of the non-interacting entanglement spectrum.

Moreover, the winding number can also be used as an independent, meaningful invariant when we have no access to the complete set of degrees of freedom of the state. This has been shown in chapter 9 for a simple case, but its full power shall be developed when such a measurement method is applied to a many body state.

Another natural question is whether there is some set of natural observables that capture the Chern number for systems bigger than pseudospins - some sort of winding number for higher dimensions. In a sense, the spin case is simple because three expectation values are equivalent to doing full tomography of the state, but the experience with the composite 4x4 case renders hope that more complicated systems do not need some tomography-equivalent set of observables for extracting topological invariants; one can only expect that new (and interesting!) restrictions may apply to this case, as the role of entanglement in this decomposition suggests.

Finally, there are some general directions that this thesis is ponting towards, and which may be interesting to mention. To name but a few, is there any measurement protocol for a many-body entanglement spectrum? Are partial invariants relevant to characterize a state, and if so, is there a meaning having all the necessary topological information in expendable degrees of freedom? Since it is possible to model topological insulators and superconductors as bidimensional spin systems, what is the many-body sense of this spin lattice having entanglement, or - inspired by the results of chapter 10 - localizable entanglement? These and other similar questions can be combined into the main objective of the thesis, as outlined in the introduction: could we extract more sense of the characterization artifacts that we use, only if we had a clear sense of how they are to be measured? We strongly believe the answer to that question is positive, and justifies the work of the present thesis.

BIBLIOGRAPHY

[1] Dmitry A. Abanin and Eugene Demler. Measuring Entanglement Entropy of a Generic Many-Body System with a Quantum Switch. *Phys. Rev. Lett.*, 109(2):020504, July 2012.

[2] A. Acín, A. Andrianov, L. Costa, E. Jané, J. Latorre, and R. Tarrach. Generalized Schmidt Decomposition and Classification of Three-Quantum-Bit States. *Phys. Rev. Lett.*, 85(7):1560–1563, August 2000.

[3] A. Acín, D. Bruß, M. Lewenstein, and A. Sanpera. Classification of Mixed Three-Qubit States. *Phys. Rev. Lett.*, 87(4):040401, July 2001.

[4] M. Aidelsburger, M. Atala, S. Nascimbène, S. Trotzky, Y.-A. Chen, and I. Bloch. Experimental Realization of Strong Effective Magnetic Fields in an Optical Lattice. *Phys. Rev. Lett.*, 107(25):255301, December 2011.

[5] E. Alba, X. Fernandez-Gonzalvo, J. Mur-Petit, J.J. Garcia-Ripoll, and J.K. Pachos. Simulating Dirac fermions with Abelian and non-Abelian gauge fields in optical lattices. *Ann. Phys. (N. Y).*, 328:64–82, January 2013.

[6] E. Alba, X. Fernandez-Gonzalvo, J. Mur-Petit, J. K. Pachos, and J. J. Garcia-Ripoll. Seeing Topological Order in Time-of-Flight Measurements. *Phys. Rev. Lett.*, 107(23):235301, November 2011.

[7] Jason Alicea. Majorana fermions in a tunable semiconductor device. *Phys. Rev. B*, 81(12):125318, March 2010.

[8] Alexander Altland and Martin R. Zirnbauer. Nonstandard symmetry classes in mesoscopic normal-superconducting hybrid structures. *Phys. Rev. B*, 55(2):1142–1161, January 1997.

[9] E. Anisimovas, F. Gerbier, T. Andrijauskas, and N. Goldman. Design of laser-coupled honeycomb optical lattices supporting Chern insulators. *Phys. Rev. A*, 89(1):013632, January 2014.

[10] M.A. Armstrong. Basic Topology.

[11] Neil W. Ashcroft and N. David Mermin. *Solid state physics.* 1976.

[12] J. Avron, R. Seiler, and B. Simon. Homotopy and Quantization in Condensed Matter Physics. *Phys. Rev. Lett.*, 51(1):51–53, July 1983.

[13] W S Bakr, A Peng, M E Tai, R Ma, J Simon, J I Gillen, S Fölling, L Pollet, and M Greiner. Probing the superfluid-to-Mott insulator transition at the single-atom level. *Science*, 329(5991):547–50, July 2010.

[14] Waseem S Bakr, Jonathon I Gillen, Amy Peng, Simon Fölling, and Markus Greiner. A quantum gas microscope for detecting single atoms in a Hubbard-regime optical lattice. *Nature*, 462(7269):74–7, November 2009.

[15] Immanuel Bloch, Jean Dalibard, and Wilhelm Zwerger. Many-body physics with ultracold gases. *Rev. Mod. Phys.*, 80(3):885–964, 2008.

[16] Kathy-Anne Brickman Soderberg, Nathan Gemelke, and Cheng Chin. Ultracold molecules: vehicles to scalable quantum information processing. *New J. Phys.*, 11(5):055022, May 2009.

[17] Hans J. Briegel and Robert Raussendorf. Persistent Entanglement in Arrays of Interacting Particles. *Phys. Rev. Lett.*, 86(5):910–913, January 2001.

[18] E. Brion, L. H. Pedersen, and K. Molmer. Adiabatic Elimination in a Lambda System. page 14, October 2006.

[19] G. Bruun and C. Pethick. Effective Theory of Feshbach Resonances and Many-Body Properties of Fermi Gases. *Phys. Rev. Lett.*, 92(14):140404, April 2004.

[20] Michele Burrello and Andrea Trombettoni. Non-Abelian Anyons from Degenerate Landau Levels of Ultracold Atoms in Artificial Gauge Potentials. *Phys. Rev. Lett.*, 105(12):125304, September 2010.

[21] Michele Burrello and Andrea Trombettoni. Ultracold atoms in U(2) non-Abelian gauge potentials preserving the Landau levels. *Phys. Rev. A*, 84(4):043625, October 2011.

[22] J. Casanova, J. J. García-Ripoll, R. Gerritsma, C. F. Roos, and E. Solano. Klein tunneling and Dirac potentials in trapped ions. *Phys. Rev. A*, 82(2):020101, August 2010.

[23] Claudio Castelnovo and Claudio Chamon. Entanglement and topological entropy of the toric code at finite temperature. *Phys. Rev. B*, 76(18):184442, November 2007.

[24] C. Chamon, R. Jackiw, Y. Nishida, S.-Y. Pi, and L. Santos. Quantizing Majorana fermions in a superconductor. *Phys. Rev. B*, 81(22):224515, June 2010.

[25] A. Dauphin, M. Müller, and M. A. Martin-Delgado. Rydberg-atom quantum simulation and Chern-number characterization of a topological Mott insulator. *Phys. Rev. A*, 86(5):053618, November 2012.

[26] Alexandre Dauphin and Nathan Goldman. Extracting the Chern Number from the Dynamics of a Fermi Gas: Implementing a Quantum Hall Bar for Cold Atoms. *Phys. Rev. Lett.*, 111(13):135302, September 2013.

[27] María Eckholt and Juan José García-Ripoll. Correlated hopping of bosonic atoms induced by optical lattices. *New J. Phys.*, 11(9):093028, September 2009.

[28] A. Einstein, B. Podolsky, and N. Rosen. Can Quantum-Mechanical Description of Physical Reality Be Considered Complete? *Phys. Rev.*, 47(10):777–780, May 1935.

[29] Simon Fölling, Artur Widera, Torben Müller, Fabrice Gerbier, and Immanuel Bloch. Formation of Spatial Shell Structure in the Superfluid to Mott Insulator Transition. *Phys. Rev. Lett.*, 97(6):060403, August 2006.

[30] FukuiTakahiro, HatsugaiYasuhiro, and SuzukiHiroshi. Chern Numbers in Discretized Brillouin Zone: Efficient Method of Computing (Spin) Hall Conductances. November 2013.

[31] Fabrice Gerbier and Jean Dalibard. Gauge fields for ultracold atoms in optical superlattices. *New J. Phys.*, 12(3):033007, March 2010.

[32] N Goldman, E Anisimovas, F Gerbier, P Öhberg, I B Spielman, and G Juzeliūnas. Measuring topology in a laser-coupled honeycomb lattice: from Chern insulators to topological semi-metals. *New J. Phys.*, 15(1):013025, January 2013.

[33] N. Goldman, W. Beugeling, and C. Morais Smith. Topological phase transitions between chiral and helical spin textures in a lattice with spin-orbit coupling and a magnetic field. *EPL (Europhysics Lett.*, 97(2):23003, January 2012.

[34] N Goldman and P Gaspard. Quantum Hall-like effect for cold atoms in non-Abelian gauge potentials. *Europhys. Lett.*, 78(6):60001, June 2007.

[35] N. Goldman, A. Kubasiak, P. Gaspard, and M. Lewenstein. Ultracold atomic gases in non-Abelian gauge potentials: The case of constant Wilson loop. *Phys. Rev. A*, 79(2):023624, February 2009.

[36] N. Goldman, I. Satija, P. Nikolic, A. Bermudez, M. A. Martin-Delgado, M. Lewenstein, and I. B. Spielman. Realistic Time-Reversal Invariant Topological Insulators with Neutral Atoms. *Phys. Rev. Lett.*, 105(25):255302, December 2010.

[37] Daniel Gottesman. Theory of fault-tolerant quantum computation. *Phys. Rev. A*, 57(1):127–137, January 1998.

[38] Markus Greiner, Olaf Mandel, Tilman Esslinger, Theodor W Hänsch, and Immanuel Bloch. Quantum phase transition from a superfluid to a Mott insulator in a gas of ultracold atoms. *Nature*, 415(6867):39–44, January 2002.

[39] Kenneth Günter, Thilo Stöferle, Henning Moritz, Michael Köhl, and Tilman Esslinger. p-Wave Interactions in Low-Dimensional Fermionic Gases. *Phys. Rev. Lett.*, 95(23):230401, November 2005.

[40] F. D. M. Haldane. Model for a Quantum Hall Effect without Landau Levels: Condensed-Matter Realization of the "Parity Anomaly". *Phys. Rev. Lett.*, 61(18):2015–2018, October 1988.

[41] M. Z. Hasan and C L Kane. Topological Insulators. *Physics (College. Park. Md).*, 82(4):23, 2010.

[42] M. Hein, W. Dür, J. Eisert, R. Raussendorf, M. Van den Nest, and H. J. Briegel. Entanglement in Graph States and its Applications. page 99, February 2006.

[43] M. Holland, S. Kokkelmans, M. Chiofalo, and R. Walser. Resonance Superfluidity in a Quantum Degenerate Fermi Gas. *Phys. Rev. Lett.*, 87(12):120406, August 2001.

[44] Timothy H. Hsieh and Liang Fu. Bulk Entanglement Spectrum Reveals Quantum Criticality within a Topological State. *Phys. Rev. Lett.*, 113(10):106801, September 2014.

[45] S. Iblisdir, D. Pérez-García, M. Aguado, and J. Pachos. Scaling law for topologically ordered systems at finite temperature. *Phys. Rev. B*, 79(13):134303, April 2009.

[46] R. Jackiw and S.-Y. Pi. Chiral Gauge Theory for Graphene. *Phys. Rev. Lett.*, 98(26):266402, June 2007.

[47] D. Jaksch, C. Bruder, J. Cirac, C. Gardiner, and P. Zoller. Cold Bosonic Atoms in Optical Lattices. *Phys. Rev. Lett.*, 81(15):3108–3111, October 1998.

[48] D Jaksch and P Zoller. Creation of effective magnetic fields in optical lattices: the Hofstadter butterfly for cold neutral atoms. *New J. Phys.*, 5(1):56–56, May 2003.

[49] Liang Jiang, Takuya Kitagawa, Jason Alicea, A. R. Akhmerov, David Pekker, Gil Refael, J. Ignacio Cirac, Eugene Demler, Mikhail D. Lukin, and Peter Zoller. Majorana Fermions in Equilibrium and in Driven Cold-Atom Quantum Wires. *Phys. Rev. Lett.*, 106(22):220402, June 2011.

[50] Jaewoo Joo, Emilio Alba, Juan José García-Ripoll, and Timothy P. Spiller. Generating and verifying graph states for fault-tolerant topological measurement-based quantum computing in two-dimensional optical lattices. *Phys. Rev. A*, 88(1):012328, July 2013.

[51] Gregor Jotzu, Michael Messer, Rémi Desbuquois, Martin Lebrat, Thomas Uehlinger, Daniel Greif, and Tilman Esslinger. Experimental realisation of the topological Haldane model. page 14, June 2014.

[52] C. L. Kane and E. J. Mele. Quantum Spin hall effect in graphene. *Phys. Rev. Lett.*, 95(22), 2005.

[53] Alexei Kitaev. Anyons in an exactly solved model and beyond. *Ann. Phys. (N. Y).*, 321(1):2–111, January 2006.

[54] O. Klein. Die Reflexion von Elektronen an einem Potentialsprung nach der relativistischen Dynamik von Dirac. *Zeitschrift für Phys.*, 53(3-4):157–165, March 1929.

[55] Andreas Klinger, Skyler Degenkolb, Nathan Gemelke, Kathy-Anne Brickman Soderberg, and Cheng Chin. Optical lattices for atom-based quantum microscopy. *Rev. Sci. Instrum.*, 81(1):013109, January 2010.

[56] Michael Köhl, Henning Moritz, Thilo Stöferle, Kenneth Günter, and Tilman Esslinger. Fermionic Atoms in a Three Dimensional Optical Lattice: Observing Fermi Surfaces, Dynamics, and Interactions. *Phys. Rev. Lett.*, 94(8):080403, March 2005.

[57] Ville Lahtinen. Interacting non-Abelian anyons as Majorana fermions in the honeycomb lattice model. *New J. Phys.*, 13(7):075009, July 2011.

[58] Ville Lahtinen, Andreas W. W. Ludwig, Jiannis K. Pachos, and Simon Trebst. Topological liquid nucleation induced by vortex-vortex interactions in Kitaev's honeycomb model. *Phys. Rev. B*, 86(7):075115, August 2012.

[59] Ville Lahtinen and Jiannis K. Pachos. Topological phase transitions driven by gauge fields in an exactly solvable model. *Phys. Rev. B*, 81(24):245132, June 2010.

[60] Lindsay J LeBlanc, Karina Jiménez-García, Ross A Williams, Matthew C Beeler, Abigail R Perry, William D Phillips, and Ian B Spielman. Observation of a superfluid Hall effect. *Proc. Natl. Acad. Sci. U. S. A.*, 109(27):10811–4, July 2012.

[61] Markus Legner and Titus Neupert. Relating the entanglement spectrum of noninteracting band insulators to their quantum geometry and topology. *Phys. Rev. B*, 88(11):115114, September 2013.

[62] Maciej Lewenstein, Anna Sanpera, and Verònica Ahufinger. *Ultracold Atoms in Optical Lattices: Simulating quantum many-body systems.* 2012.

[63] Hui Li and F. Haldane. Entanglement Spectrum as a Generalization of Entanglement Entropy: Identification of Topological Order in Non-Abelian Fractional Quantum Hall Effect States. *Phys. Rev. Lett.*, 101(1):010504, July 2008.

[64] Olaf Mandel, Markus Greiner, Artur Widera, Tim Rom, Theodor W. Hänsch, and Immanuel Bloch. Coherent Transport of Neutral Atoms in Spin-Dependent Optical Lattice Potentials. *Phys. Rev. Lett.*, 91(1):010407, July 2003.

[65] Paolo Maraner and Jiannis K. Pachos. Yang–Mills gauge theories from simple fermionic lattice models. *Phys. Lett. A*, 373(30):2542–2545, July 2009.

[66] Leonardo Mazza, Alejandro Bermudez, Nathan Goldman, Matteo Rizzi, Miguel Angel Martin-Delgado, and Maciej Lewenstein. An optical-lattice-based quantum simulator for relativistic field theories and topological insulators. *New J. Phys.*, 14(1):015007, January 2012.

[67] Harold J. Metcalf and Peter van der Straten. *Laser Cooling and Trapping.* Graduate Texts in Contemporary Physics. Springer New York, New York, NY, 1999.

[68] V Mourik, K Zuo, S M Frolov, S R Plissard, E P A M Bakkers, and L P Kouwenhoven. Signatures of Majorana fermions in hybrid superconductor-semiconductor nanowire devices. *Science*, 336(6084):1003–7, May 2012.

[69] Chetan Nayak, Ady Stern, Michael Freedman, and Sankar Das Sarma. Non-Abelian anyons and topological quantum computation. *Rev. Mod. Phys.*, 80(3):1083–1159, September 2008.

[70] K. Osterloh, M. Baig, L. Santos, P. Zoller, and M. Lewenstein. Cold Atoms in Non-Abelian Gauge Potentials: From the Hofstadter "Moth" to Lattice Gauge Theory. *Phys. Rev. Lett.*, 95(1):010403, June 2005.

[71] Rebecca N Palmer and Jiannis K Pachos. Fractional quantum Hall effect in a U(1)×SU(2) gauge field. *New J. Phys.*, 13(6):065002, June 2011.

[72] Siddharth A. Parameswaran, Rahul Roy, and Shivaji L. Sondhi. Fractional quantum Hall physics in topological flat bands. *Comptes Rendus Phys.*, 14(9-10):816–839, November 2013.

[73] Vitor Pereira, A. Castro Neto, and N. Peres. Tight-binding approach to uniaxial strain in graphene. *Phys. Rev. B*, 80(4):045401, July 2009.

[74] Ingo Peschel. Calculation of reduced density matrices from correlation functions. *J. Phys. A. Math. Gen.*, 36(14):L205–L208, April 2003.

[75] H. Pino, E. Alba, J. Taron, J. J. Garcia-Ripoll, and N. Barberán. Hall response of interacting bosonic atoms in strong gauge fields: From condensed to fractional-quantum-Hall states. *Phys. Rev. A*, 87(5):053611, May 2013.

[76] Xiao-Liang Qi, Taylor Hughes, S. Raghu, and Shou-Cheng Zhang. Time-Reversal-Invariant Topological Superconductors and Superfluids in Two and Three Dimensions. *Phys. Rev. Lett.*, 102(18):187001, May 2009.

[77] J. Radić, A. Di Ciolo, K. Sun, and V. Galitski. Exotic Quantum Spin Models in Spin-Orbit-Coupled Mott Insulators. *Phys. Rev. Lett.*, 109(8):085303, August 2012.

[78] C. A. Regal, C. Ticknor, J. L. Bohn, and D. S. Jin. Tuning p-Wave Interactions in an Ultracold Fermi Gas of Atoms. *Phys. Rev. Lett.*, 90(5):053201, February 2003.

[79] Zohar Ringel and Yaacov E. Kraus. Determining topological order from a local ground-state correlation function. *Phys. Rev. B*, 83(24):245115, June 2011.

[80] Shinsei Ryu, Andreas P Schnyder, Akira Furusaki, and Andreas W W Ludwig. Topological insulators and superconductors: tenfold way and dimensional hierarchy. *New J. Phys.*, 12(6):065010, June 2010.

[81] Masatoshi Sato, Yoshiro Takahashi, and Satoshi Fujimoto. Non-Abelian Topological Order in s-Wave Superfluids of Ultracold Fermionic Atoms. *Phys. Rev. Lett.*, 103(2):020401, July 2009.

[82] Andreas Schnyder, Shinsei Ryu, Akira Furusaki, and Andreas Ludwig. Classification of topological insulators and superconductors in three spatial dimensions. *Phys. Rev. B*, 78(19):195125, November 2008.

[83] E. Schrödinger and M. Born. Discussion of Probability Relations between Separated Systems. *Math. Proc. Cambridge Philos. Soc.*, 31(04):555, October 2008.

[84] Gordon Semenoff. Condensed-Matter Simulation of a Three-Dimensional Anomaly. *Phys. Rev. Lett.*, 53(26):2449–2452, December 1984.

[85] D. Sheng, Z. Weng, L. Sheng, and F. Haldane. Quantum Spin-Hall Effect and Topologically Invariant Chern Numbers. *Phys. Rev. Lett.*, 97(3):036808, July 2006.

[86] I. Spielman. Raman processes and effective gauge potentials. *Phys. Rev. A*, 79(6):063613, June 2009.

[87] A. Sterdyniak, N. Regnault, and B. A. Bernevig. Extracting Excitations from Model State Entanglement. *Phys. Rev. Lett.*, 106(10):100405, March 2011.

[88] J. Struck, C. Ölschläger, M. Weinberg, P. Hauke, J. Simonet, A. Eckardt, M. Lewenstein, K. Sengstock, and P. Windpassinger. Tunable Gauge Potential for Neutral and Spinless Particles in Driven Optical Lattices. *Phys. Rev. Lett.*, 108(22):225304, May 2012.

[89] Leonard Susskind. Lattice fermions. *Phys. Rev. D*, 16(10):3031–3039, November 1977.

[90] Leticia Tarruell, Daniel Greif, Thomas Uehlinger, Gregor Jotzu, and Tilman Esslinger. Creating, moving and merging Dirac points with a Fermi gas in a tunable honeycomb lattice. *Nature*, 483(7389):302–5, March 2012.

[91] D. Thouless, M. Kohmoto, M. Nightingale, and M. den Nijs. Quantized Hall Conductance in a Two-Dimensional Periodic Potential. *Phys. Rev. Lett.*, 49(6):405–408, August 1982.

[92] Géza Tóth and Otfried Gühne. Detecting Genuine Multipartite Entanglement with Two Local Measurements. *Phys. Rev. Lett.*, 94(6):060501, February 2005.

[93] Géza Tóth and Otfried Gühne. Entanglement detection in the stabilizer formalism. *Phys. Rev. A*, 72(2):022340, August 2005.

[94] M.A.H. Vozmediano, M.I. Katsnelson, and F. Guinea. Gauge fields in graphene. *Phys. Rep.*, 496(4-5):109–148, November 2010.

[95] Lei Wang, Alexey Soluyanov, and Matthias Troyer. Proposal for Direct Measurement of Topological Invariants in Optical Lattices. *Phys. Rev. Lett.*, 110(16):166802, April 2013.

[96] Gregory Wannier. The Structure of Electronic Excitation Levels in Insulating Crystals. *Phys. Rev.*, 52(3):191–197, August 1937.

[97] Christof Weitenberg, Manuel Endres, Jacob F Sherson, Marc Cheneau, Peter Schauss, Takeshi Fukuhara, Immanuel Bloch, and Stefan Kuhr. Single-spin addressing in an atomic Mott insulator. *Nature*, 471(7338):319–24, March 2011.

[98] Daijiro Yoshioka. *The Quantum Hall Effect*, volume 133 of *Springer Series in Solid-State Sciences*. Springer Berlin Heidelberg, Berlin, Heidelberg, 2002.

[99] Yue Yu and Ziqiang Wang. An exactly soluble model with tunable p - wave paired fermion ground states. *EPL (Europhysics Lett.*, 84(5):57002, December 2008.

[100] Chuanwei Zhang, Sumanta Tewari, Roman M. Lutchyn, and S. Das Sarma. p_{x}+ip_{y} Superfluid from s-Wave Interactions of Fermionic Cold Atoms. *Phys. Rev. Lett.*, 101(16):160401, October 2008.

[101] Shi-Liang Zhu, Baigeng Wang, and L.-M. Duan. Simulation and Detection of Dirac Fermions with Cold Atoms in an Optical Lattice. *Phys. Rev. Lett.*, 98(26):260402, June 2007.

[102] W. Zwerger. Mott-Hubbard transition of cold atoms in optical lattices. page 17, November 2002.

[103] M. Zwierlein, C. Stan, C. Schunck, S. Raupach, A. Kerman, and W. Ketterle. Condensation of Pairs of Fermionic Atoms near a Feshbach Resonance. *Phys. Rev. Lett.*, 92(12):120403, March 2004.